AUTOMATIC SEGMENTATION OF MITOCHONDRIA IN SCANNING
ELECTRON MICROSCOPY IMAGES

A THESIS SUBMITTED TO
THE GRADUATE SCHOOL OF INFORMATICS OF
THE MIDDLE EAST TECHNICAL UNIVERSITY
BY

MEHMET ÇAĞRI GÜVEN

IN PARTIAL FULFILLMENT OF THE REQUIREMENTS FOR THE DEGREE
OF
MASTER OF SCIENCE
IN
THE DEPARTMENT OF INFORMATION SYSTEMS

SEPTEMBER 2021

**AUTOMATIC SEGMENTATION OF MITOCHONDRIA IN SCANNING
ELECTRON MICROSCOPY IMAGES**

submitted by **MEHMET ÇAĞRI GÜVEN** in partial fulfillment of the requirements
for the degree of **Master of Science in Information Systems Department, Middle
East Technical University** by,

Prof. Dr. Deniz Zeyrek Bozşahin
Dean, **Graduate School of Informatics** ⎯⎯⎯⎯⎯⎯⎯

Prof. Dr. Sevgi Özkan Yıldırım
Head of Department, **Information Systems** ⎯⎯⎯⎯⎯⎯⎯

Prof. Dr. Ünal Erkan Mumcuoğlu
Supervisor, **Health Informatics, METU** ⎯⎯⎯⎯⎯⎯⎯

Examining Committee Members:

Assoc. Prof. Dr. Aysu Betin Can
Information Systems , METU ⎯⎯⎯⎯⎯⎯⎯

Prof. Dr. Ünal Erkan Mumcuoğlu
Health Informatics , METU ⎯⎯⎯⎯⎯⎯⎯

Assist. Prof. Dr. Burçak Otlu
Health Informatics, METU ⎯⎯⎯⎯⎯⎯⎯

Assoc. Prof. Dr. Ahmet Murat Özbayoğlu
Computer Engineering, TOBB ETÜ ⎯⎯⎯⎯⎯⎯⎯

Prof. Dr. Sevgi Özkan Yıldırım
Information Systems, METU ⎯⎯⎯⎯⎯⎯⎯

Date: 07.09.2021

I hereby declare that all information in this document has been obtained and presented in accordance with academic rules and ethical conduct. I also declare that, as required by these rules and conduct, I have fully cited and referenced all material and results that are not original to this work.

Name, Surname: Mehmet Çağrı Güven

Signature   :

ABSTRACT

**AUTOMATIC SEGMENTATION OF MITOCHONDRIA IN SCANNING
ELECTRON MICROSCOPY IMAGES**

Güven, Mehmet Çağrı

M.S., Department of Information Systems

Supervisor: Prof. Dr. Ünal Erkan Mumcuoğlu

September 2021, 78 pages

Many studies have shown that shape of mitochondria indicates the occurrence of diseases. Scanning Electron Microscopy (SEM) enables to obtain image of internal structures of the cell and mitochondria. Automatic segmentation of mitochondria contributes to the decision of diseases by specialists. There is limited study about automatic segmentation of mitochondria in Serial Block-Face Scanning Electron Microscopy (SFBSEM) images. SBFSEM imaging technique provides full automation, well registered images, less time and less effort for data acquisition. Therefore, SBF-SEM imaging technique is selected for this study. Recently, deep learning methods have been implemented for image processing of SEM datasets. However, due to requirement of huge datasets, much effort and powerful computers for preparing testing and training data, energy based model is implemented for this study. The algorithms used in this thesis are primarily the algorithms developed by Tasel et al for mitochondria segmentation in TEM images. The method includes preprocessing, ridge detection, energy mapping, curve fitting, snake-based shape extraction, validation and post-processing steps. In this thesis, these algorithms are adapted and refined for SBFSEM images to obtain optimum performance. Evaluations are made by using Dice Similarity Coefficient (DSC), precision, recall and F-Score metrics.

ÖZ

TARAMALI ELEKTRON MİKROSKOBU GÖRÜNTÜLERİNDE MİTOKONDRİLERİN OTOMATİK OLARAK BÖLÜTLENMESİ

Güven, Mehmet Çağrı

Yüksek Lisans, Bilişim Sistemleri Bölümü

Tez Yöneticisi: Prof. Dr. Ünal Erkan Mumcuoğlu

Eylül 2021, 78 sayfa

Birçok çalışma mitokondri ve kristaların şeklinin hastalıkların oluşumunu belirttiğini göstermektedir. Taramalı Elektron Mikroskobu (SEM), hücrenin iç yapılarının ve mitokondrilerin görüntülerinin elde edilmesini sağlar. Mitokondrilerin otomatik bölütlenmesi uzmanlar tarafından hastalıkların karar verilmesine katkı sağlar. Seri Blok-Yüz Taramalı Elektron Mikroskobu (SFBSEM) görüntülerinde mitokondrinin otomatik segmentasyonu hakkında sınırlı çalışma vardır. SBFSEM görüntüleme tekniği, tam otomasyon, iyi kaydedilmiş görüntüler, veri elde etmek için daha az zaman ve daha az çaba sağlar. Bu nedenle, bu çalışma için SBFSEM görüntüleme tekniği seçilmiştir. Son zamanlarda, derin öğrenme yöntemleri SEM veri setlerinin görüntü işlemesi için uygulanmaktadır. Ancak, büyük veri setlerinin, fazla çabanın ve test ve eğitim verilerinin hazırlanması için güçlü bilgisayarların gerekliliğinden bu çalışma için enerji tabanlı model uygulanmaktadır. Bu tezde kullanılan algoritmalar öncelikle TEM görüntülerinde mitokondri bölütlenmesi için Tasel ve arkadaşları tarafından geliştirilen algoritmalardır. Yöntem, ön işleme, sırt algılama, enerji haritalama, eğri uyumlandırma, yılan temelli şekil çıkarma, doğrulama ve son işlem adımlarını içerir. Bu tezde, bu algoritmalar optimum performans elde etmek için SBFSEM görüntüleri için uyarlanmış ve yeniden düzenlenmiştir. Değerlendirmeler Dice Benzerlik Katsayısı(DSC), kesinlik, hatırlama ve F-Skoru metrikleri kullanılarak yapılır.

Anahtar Kelimeler: Mitokondri Bölütlenmesi, Taramalı Elektron Mikroskobu, Sırt Algılama, Eğri Uyumlandırma, Yılan Temelli Şekil Çıkarma

To the my beauty, Hatice Kaya Güven, who is the meaning of my life

ACKNOWLEDGMENTS

TABLE OF CONTENTS

LIST OF TABLES

LIST OF FIGURES

LIST OF ABBREVIATIONS

2D	2 Dimensions
2.5D	Two-and-half Dimensions
3D	3 Dimensions
AdaBoost	Adaptive Boosting
ANN	Artificial Neural Network
ATP	Adenosine Triphosphate
ATUM	Automatic Tape-collecting UltraMicrotome
ATUM-SEM	Automatic Tape-collecting UltraMicrotome Scanning Electron Microscopy
BD	Bipolar Disorder
CCDB	Cell Centered Database
CNN	Convolutional Neural Network
Cyro-ET	Cryo-electron tomography
CDF	Cumulative Distribution Function
DBSCAN	Density-Based Spatial Clustering of Applications with Noise
DNA	Deoxyribonucleic Acid
DSC	Dice Similarity Coefficient
EMT	Electron Microscope Tomography
ER	Endoplasmic Reticulum
E-T	Everhart-Thornley
FPN	Feature Pyramid Network
FIB-SEM	Focused Ion Beam Scanning Electron Microscopy
MUC-4	Fourth Message Understanding Conference

GPU	Graphics Processing Units
IA-SEM	Ion-Abrasion Scanning Electron Microscopy
k-NN	k-Nearest Neighbor
MSBE	Median Symmetric Boundary Error
mm	milimeter
nm	nanometer
NCMIR	National Center for Microscopy and Imaging Research
NN	Neural Network
R-CNN	Region Based Convolutional Neural Networks
RNA	Ribonucleic Acid
RPN	Region Proposal Network
ROI	Region Of Interest
SBEM	Serial Block Face Scanning Electron Microscopy
SBFSEM	Serial Block Face Scanning Electron Microscopy
SEM	Scanning Electron Microscopy
SNR	Signal-to-Noise Ratios
SVM	Support Vector Machine
MUC-3	Third Message Understanding Conference
TEM	Transmission Electron Microscopy
U-Net	Universal Network
VGG	Visual Geometry Group

CHAPTER 1

INTRODUCTION

1.1 Problem Definition

Living beings consist of simple structural molecules or many functional systems which include organs. Organs are made up of tissues that have similar functions. Tissues are likewise made up of cells that have similar tasks. A cell has many organelles which fulfill different tasks. A mitochondrion is one of these organelles. It meets the energy requirement of the cell. It is necessary to obtain high-resolution images for detecting and segmenting mitochondria inside the cell. Electron Microscopy Tomography(EMT) imaging technique provides high-resolution images by visualizing the inner structure of the cell and mitochondrion. Scanning Electron Microscopy(SEM) imaging technique is a type of EMT imaging technique. In this study, automatic segmentation of mitochondria is carried out by using images of the cell that are obtained by the SEM.

1.2 Biological Information About Mitochondria

1.2.1 Cell Structures and Organelles

A cell consists of many organelles. Some of these organelles are ribosomes, endoplasmic reticulum (ER), golgi body, centrosome, mitochondrion, and nucleus as can be seen in Figure 1. All of them have important functions for the cell. Cell organelles have these functions to enable the cell to survive and to be reproduced. They are all specialized in fulfilling specific tasks. The task of the ER is to synthesize proteins and lipids for other organelles and membranes. Membrane of ER has a size more than half of the size of cell membrane. Moreover, the total area including internal space can cover 10 percent or more than the area of the cell. The golgi body works as a carrier inside the cell. Its task is to package and carry proteins, lipids, and some other particles from ER to other organelles and cell membranes. It modifies lipids and proteins while doing this task. It also makes biosynthesis of lipids. The task of lysosomes is to digest substances produced by a cell or taken from the outside. Centrosomes consist of centrioles which help chromosomes to separate from each other during the cell division. Centrosomes and lysosomes exist only in animal cells. The
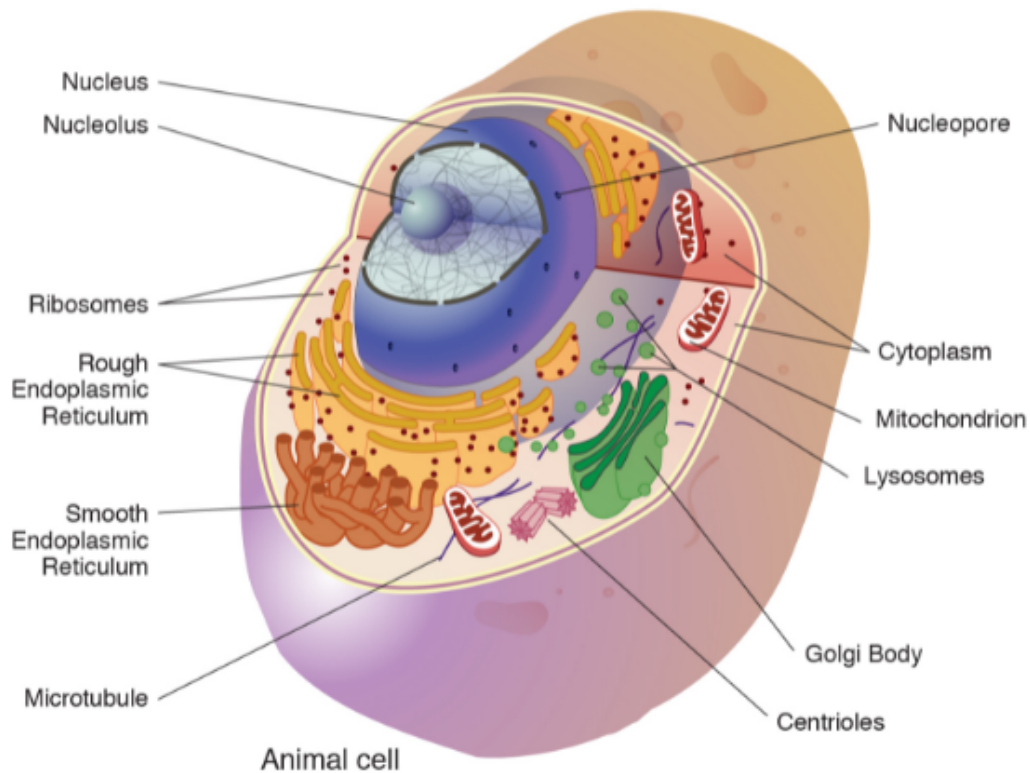
Figure 1: Internal Structure of An Animal Cell and Organelles[5]

biggest structure of the cell is the nucleus. It consists of RNA and DNA, which are the inheritance genetic material of the cell. The task of mitochondria is to produce energy for the cell and convert energy to substances that the cell is able to use [16].

1.2.2 Mitochondrion Structure and Mitochondrion Association with Diseases

Mitochondria are defined as power plant of the cell. It supplies 90% of the cell's ATP requirement. Moreover, they are responsible for other functions of cell metabolism. They regulate ion balance, cell growth, redox status, cell signaling. As a result, they have important function for the cell to survive [17].

Mitochondria have the double membrane structure which consists of inner and outer membranes. The outer membrane forms the external shape of mitochondria. The inner membrane forms the structure of cristae. The inner membrane has indented structure, and it forms cristae by making indentations throughout the matrix inside mitochondria. In recent studies, membranes and morphology of cristae have been examined in detail to show relationship between the function of mitochondria and the physical structure of mitochondria [35].
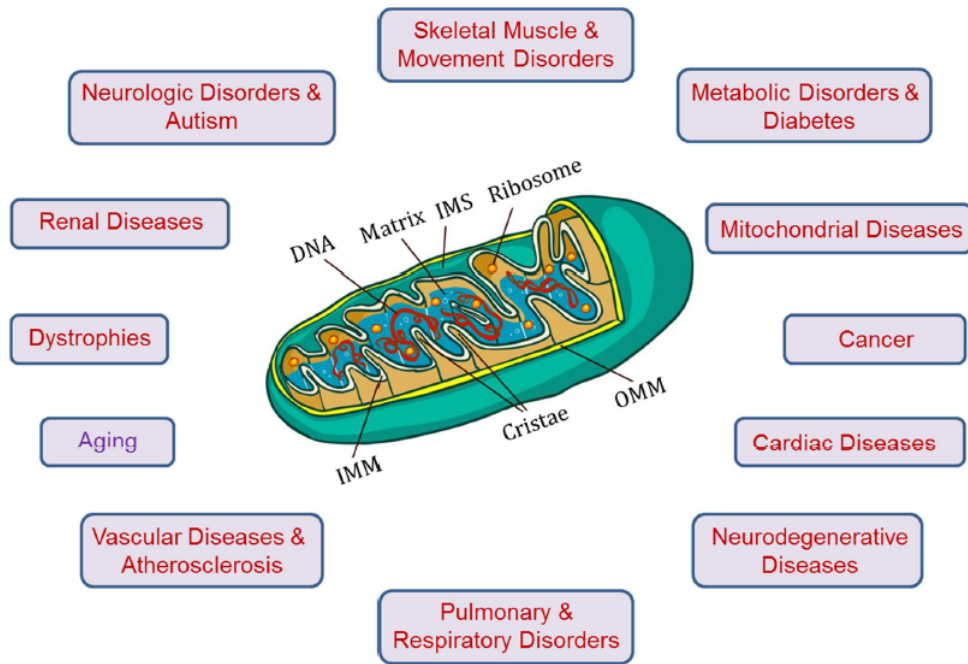
Figure 2: Mitochondria are indicators of many diseases [17]

.

Several kinds of research have shown that mitochondria and cristae are very important signs of many diseases. Dysfunctions of mitochondria cause various diseases specified in Figure 2. Functions and structures of mitochondria and cristae are important for diseases such as pathogenesis and progression of numerous human diseases, cancer, neurodegenerative and cardiovascular disorders, diabetes, traumatic brain injury, and inflammation [17]. Furthermore, in the study of [17], it is stated that 11 articles have worked on the effect of mitochondrial dysfunction in several pathological conditions based on four main titles which are neurological disorders, liver diseases, diseases associated with oxygen deficiency, and inborn, metabolic diseases.

1.3 Motivation

1.3.1 Significance of Automatic Mitochondria Segmentation

Segmentation of mitochondria is important for deciding the relationship between cells and their behavior since mitochondria are indicators for some diseases as stated in subsection 1.2.2. The external structure, shape, size, and cellular location of mitochondria give information about the disease and its function. There is a correlation between the size of the mitochondrion and glucose disposal rate as well as insulin sensitivity. The size of mitochondrion is an indicator of diabetes [20]. The sizes of mitochondria and cristae are reduced in Alzheimer's disease [3]. In the study of

[4], the size, shape, and intracellular distribution of mitochondria change in patients that have Bipolar Disorder(BD) as compared to healthy people. Cellular location and external structure have critical importance for functions of mitochondria [33]. Therefore, automatic segmentation of mitochondria and cristae membranes contribute to the decision of illnesses.

Doctors and scientists spend a lot of time and make huge effort to determine diseases mentioned above and detect mitochondria with a software tool. IMOD computer tool is used for the segmentation of mitochondria manually. IMOD is the tool which is used for image processing, modeling and monitoring of the tomographic reconstructed images. Moreover, it provides 3D reconstruction of EM serial sections and optical sections. The tool provides alignment and combination of 2D image stacks. Moreover, it enables to show 3D image from views of different angles [36]. The shape and structure of mitochondria differ in each dataset. Therefore, if automatic segmentation is not conducted, specialists need to carry out segmentation by hand. Nevertheless, this process is time-consuming and exhausting.

Recently, deep learning methods have been applied for the automatic segmentation of mitochondria in SEM images. Deep learning methods need huge memory, huge data, Graphics Processing Units(GPU) power and time effort. Data must be prepared to give as input to deep learning method. Data preparation process takes a long time, and huge effort is necessary since a large amount of data should be trained to become successful. These large amount of data must be marked for testing. Labor force is necessary for marking. Moreover, marking of mitochondria requires technical knowledge about mitochondria and structure of the cell. There is not enough time for experts to mark mitochondria for this study. Furthermore, GPU power and high performance computers are important to achieve successful results. There is not enough data and powerful computers for training and testing to use deep learning methods. In addition, deep learning methods use huge data without considering the relationship between successive slices. In SEM images, successive slices are important to decide mitochondria. Even experts use successive slices by making decision about one shape as mitochondria or not. Deep learning methods do not use this information. Deep learning methods are not preferred for automatic segmentation of mitochondria because of the reasons stated above. Energy based method which uses information in successive slices proposed by [35] is preferred. By adding elimination algorithms for false initial points of snake method and false detected snake contours, study of [35] is made robust, and acceptable results are obtained.

As a result, automatic segmentation of mitochondria in this study contributes to saving time, getting correct results and spending less effort. In this study, powerful computers which use GPU for high computation power are not required. Moreover, the method in this study uses little data instead of huge data as compared to deep learning methods. Data preparation process is not needed. Only ground truths are marked to obtain evaluation metrics. This is less time consuming process in terms of labor force as compared to other studies. Energy based method is implemented because of the reasons stated above.

4

1.4   Imaging Techniques

There are many types of microscopes. Some of these are optical microscope which uses light passed throughout the object, electron microscope which uses a beam of accelerated electrons passed throughout the object, scanning probe microscope which uses a physical probe to scan the object, X-ray microscope which uses electromagnetic radiation throughout the object.

The resolution power of human eyes is around 0.2 mm. This means that human eyes have a limited distance to distinguish two point from each other. A light microscope has resolution about 1000 times the resolution of the human eye. Therefore, it provides the human eye with distinguishing objects in 200 nm resolution. EMT has a higher resolution than light microscope due to limitations of physics of the light[18].

In many studies, images are obtained by two types of electron microscopy tomography methods for the automatic segmentation of membrane in medical imaging. These types of EMT are Transmission Electron Microscopy(TEM) and SEM imaging techniques.

1.4.1   Transmission Electron Microscopy

TEM consists of physical elements demonstrated in Figure 3. These elements are an electron gun, condenser lens, objective aperture, objective lens, projector lenses, and a fluorescent screen. Firstly, an electron gun forms a beam of electrons with high kinetic energy enough to direct on a thin road through the sample. The electron gun consists of two parts which are electron source and electron accelerating chamber. The name of the electron source is cathode which has negative voltage relative to the anode. Electrons are accelerated through the anode that has positive voltage relative to the cathode. An electric field is generated between the anode, and the cathode enable electrons to have kinetic energy. Most of the accelerated electrons are eliminated by an anode plate. The condenser lens makes the electron beam parallel and focuses it through the sample by setting the area of the beam as close as possible to the area of the sample. After the electron beam hits the specimen, initially objective lenses are used to focus the distracted beam and increase the illumination of the image. The objective lens aperture takes place below the objective lens and produces a contrast. Moreover, it prevents too much blurring on the image. An intermediate lens is also used to magnify images coming from the objective lens. Furthermore, it creates an electron diffraction pattern on the screen. Finally, projector lens forms image and diffraction pattern on the whole fluorescent screen [9]. The scanning of sample process is conducted for different angles between electron beams and specimen as seen in Figure 4. This process is conducted for different tilt angles between ± 70. The angle between each successive scan is around 1-2 °. Projection data on the specimen for different angles are acquired. Then, these projection data are used to obtain 3D reconstructed image by applying back-projection techniques in spatial or Fourier domain [35].
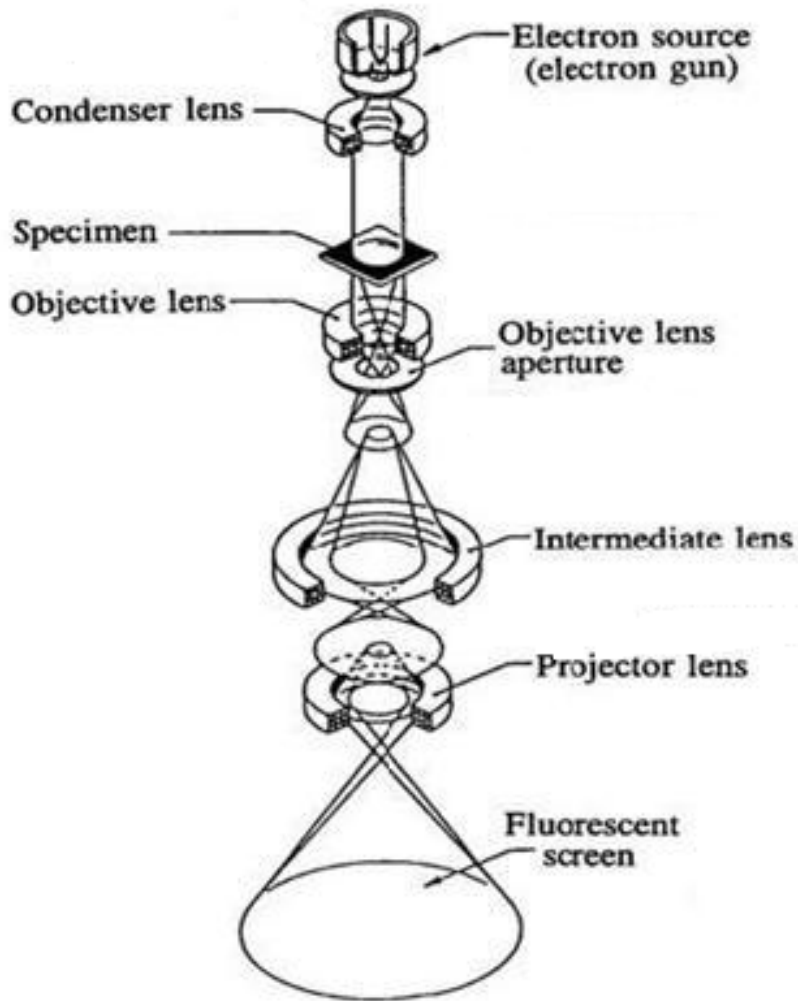
Figure 3: Schematics of the physical structure of the Transmission Electron Microscope[22]
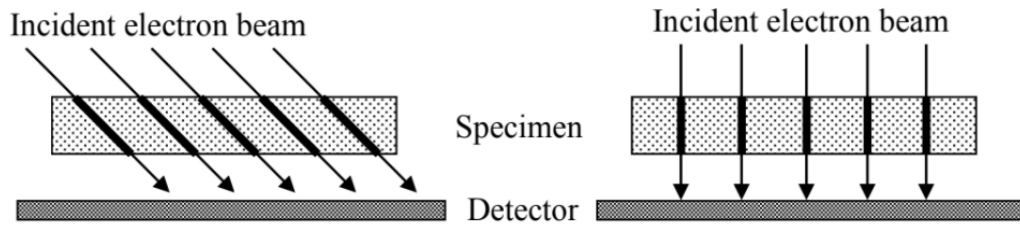
Figure 4: Projection of Electron Beams on the Specimen For Different Tilt Beam Angles in TEM[35]

1.4.2 Scanning Electron Microscopy

For this study, the SEM imaging technique is used to obtain samples. The SEM is based on scattered electrons emitted from the surface of the sample. Figure 5 shows the schematic of the physical structure of the SEM. As can be seen in Figure 5, there is an electron gun which creates a beam of electrons with a tungsten filament cathode throughout an accelerating anode. The tungsten filament cathode is used for electron guns because tungsten's vapor pressure is lower than all other metals. Moreover, melting point is higher than all other metals, and it has a low cost. Therefore, it is suitable to use the tungsten inside of the electron gun because of the feature about heating and cost. As the name of the accelerating anode implies, anode accelerates electrons and converts the spot beam of the electrons into a linear shape. The electron beam is focused on the limited path by the focusing magnet. After the focusing magnet, the electron beam is directed to the scanning magnet which changes the direction of the beam in the x and y axes to scan in raster format over a rectangular area of the surface of the sample [18].

When the electron beam hits the sample, Auger Effect occurs. Figure 6 shows the Auger Effect. After a hit occurs, an electron from one higher energy level settles down to the energy level which the secondary electron previously was in. Electrons in the incident electron beam become scattered electrons. After this incident, because of the displacement of the electron from one higher energy level to a low energy level, released energy is shared between the characteristic X-Ray and the Auger electron. The Auger electron is an electron in the outermost energy level which has ejected from the sample. This incident causes the sample to ionize because of the Auger electron[29].

When the focused beam touches the sample, it produces secondary electrons, auger electrons, back-scattered electrons, characteristic X-Rays, and Cathodoluminescence as demonstrated in Figure 7. Back-scattered electrons and secondary electrons are collected by the Everhart-Thornley (E-T) detector. This detector converts the signals into images in digital form by applying intensity changes in point-by-point on the screen [11].
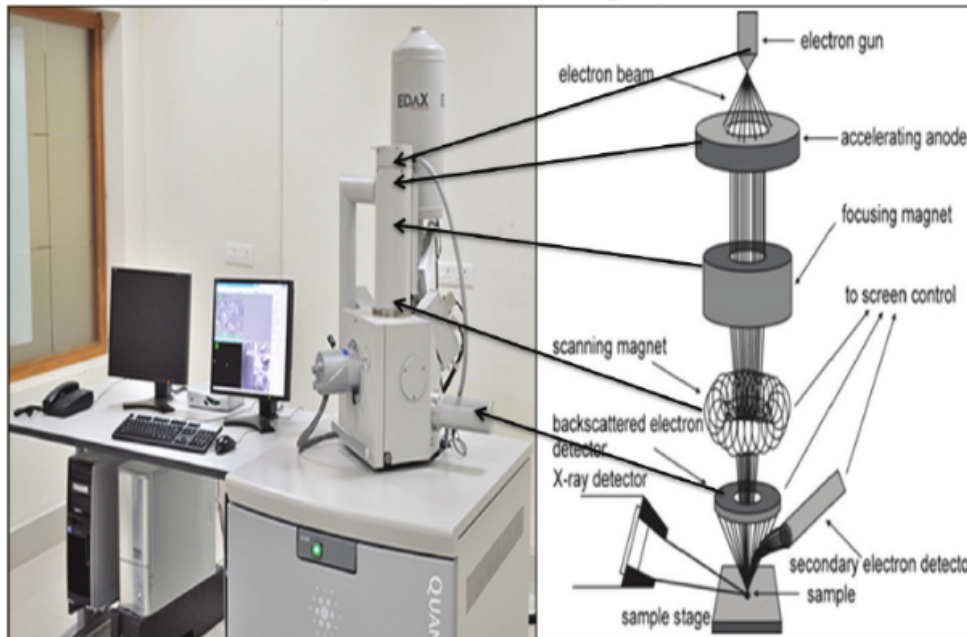
Figure 5: Schematics of the physical structure of the Scanning Electron Microscope[18]

SBEM in Figure 8 refers to serial block-face scanning electron microscopy(SBFSEM). Explanations in Figure 8 referenced from [14] explain phases of the sub-slice imaging in the SBFSEM. Moreover, this procedure is explained in [30] as "Imaging a 3D volume can be achieved by utilizing a special type of SEM technique which is SBFSEM. In the SBFSEM technique, a stack of 2D images is obtained by cutting ultra-thin sections from the surface using a diamond knife and then imaging by SEM. This technique supplies 3D volumetric data formed by a series of 2D images each associated to a single slice."

While TEM images are used to get information about inner structure of the cell, SEM images are used to get information about surface and its composition. In this study, automatic segmentation of mitochondria is conducted to help specialists to determine diseases. Information about surface and composition of sample is necessary for this decision. SEM images provide information about membranes of mitochondria [38]. Furthermore, sample preparation of the SEM is conducted by using little effort as compared to TEM. On the other hand, sample preparation task takes a long time and labor- intensive [21]. However, imaging of the SEM samples can be directly made by putting them into an aluminum stub. This means that SEM imaging is performed to acquire and interpret results easily without much effort. Moreover, root cause of the decision is related to big price differences between two imaging techniques and ease of use. Although TEM provides much more resolving power and easy segmentation of mitochondria, it is much more expensive and more complex than SEM. It is necessary intensive training of TEM before operating them. Special procedures

8
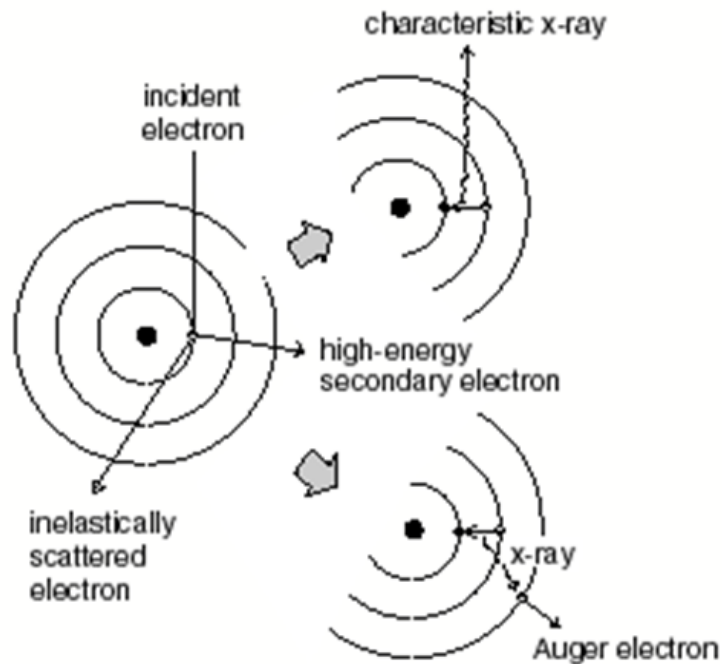
Figure 6: Auger Effect

with several steps are used for TEM such as the alignment of the electron beam. Two imaging techniques differ from each other on how they are operated. SEM needs much less acceleration voltage as compared to TEM. SEM also has advantage concerning maximum field of view (FOV) which SEM can have. Larger FOV is obtained in SEM. This means that while SEM shows large part of the sample, TEM shows very small part of the sample. Similarly, the depth of field of TEM is lower than the SEM [38]. These are the advantages of SEM as compared to TEM. This is why we prefer SEM imaging technique in this study.

1.5 Aim and Scope

The morphology of mitochondria gives an idea about the cell and organism. In this work, automatic segmentation of mitochondria in SBFSEM images is aimed. The main aim is to gain time and to obtain robust, and correct results during the segmentation process since manual segmentation of mitochondria by hand is a very time-consuming and exhausting process. Moreover, there are a few studies which make automatic segmentation in SEM Images such as [25], [23], [31], [12], [41], [32]. Most of studies mentioned above are implemented by using focused ion beam-scanning electron microscopy (FIB-SEM) and automatic tape-collecting ultra micro-tome scanning electron microscopy (ATUM-SEM). Only study which uses SBFSEM
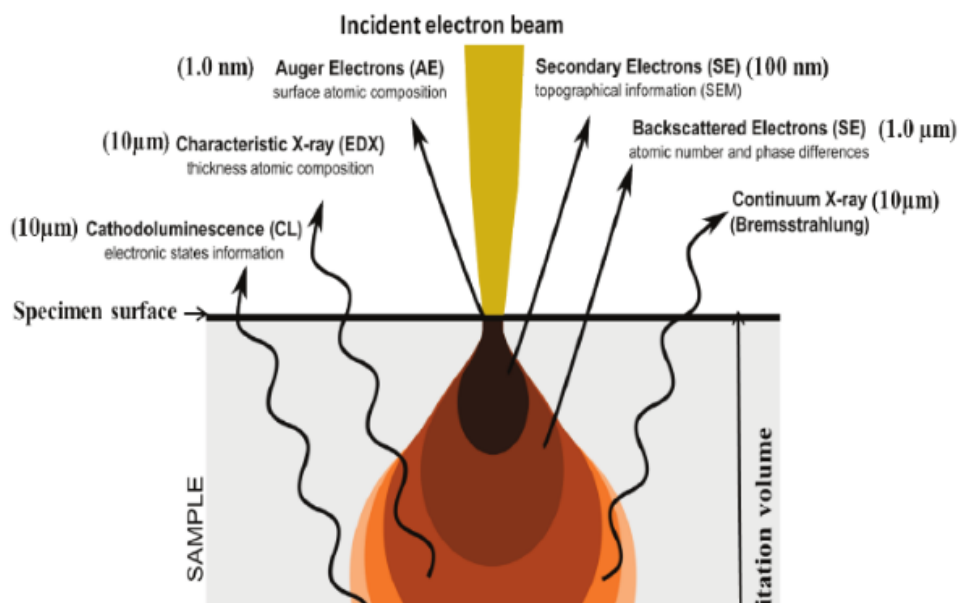
Figure 7: The moment that the incident electron beam touches the surface of the sample[18]

is the study of Giuly et al. [12]. Moreover, study of Narasimha uses ion-abrasion scanning electron microscopy images (IA-SEM).

In study of [12], importance of SBFSEM emphasised by stating that reasons for choosing SBFSEM. These reasons are achievement of full automation, rapid obtainment, getting well registered images and commercial availability of SBFSEM images. Recently, usage of SBFSEM has been increased exponential in recent years because the technical properties like convenient preparation of the tissue preparation and parameters of imaging provide remarkable success for this imaging technique [15]. Moreover, images obtained by using SBFSEM have more acquisition area, more pixels and wider FOV as compared to other imaging techniques. Acquisition time, effort for acquisition and voltage needed for acceleration are lower than other imaging techniques.

Properties of ATUM-SEM, FIB-SEM and SBFSEM are given in Figure 9 which is taken from [34]. Moreover, properties of FIB-SEM, SBFSEM, Array Tomography and TEM are given in Figure 10 which is taken from [13]. Although SBFSEM has lower resolution than TEM, FIB-SEM, ATUM SEM imaging techniques, automatic segmentation in SBFSEM dataset is aimed commercially because of reasons stated above, Figure 9 and Figure 10.

Method of Giuly et al. [12] is worked on the SBFSEM image. We aimed to compare our results with the results of [12]. However, the study of [12] uses training and testing data for segmentation. Preparation of the huge data which is used in the study of [12] is required. Moreover, computational time is necessary to train and test data. For the study of [12], the proposed method needs to process very huge data. Usage of

10
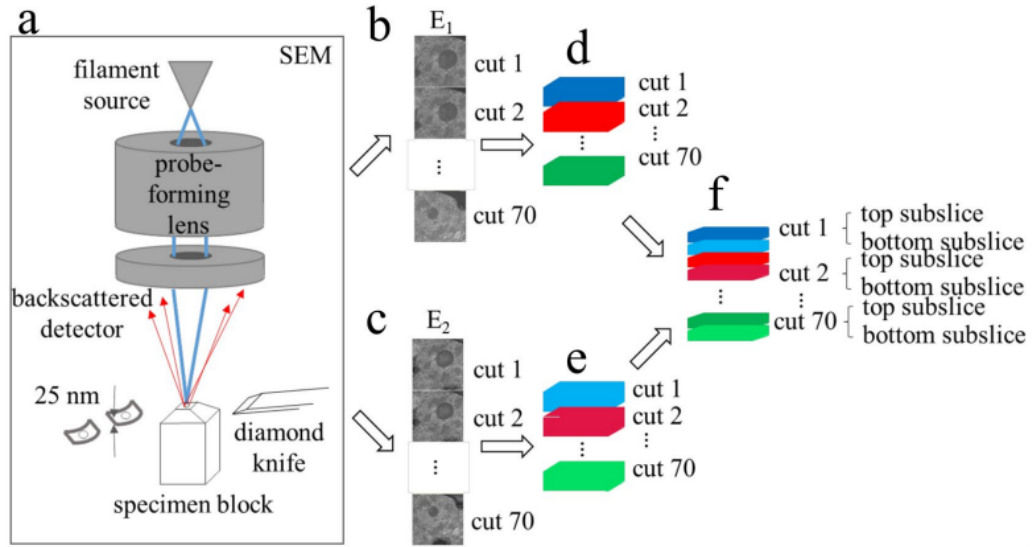
Figure 8: "Diagram of sub-slice imaging in the SBEM. (a) Surface of the sample block is imaged by scanning a focused electron probe from a field emission source across a region of interest and collecting back-scattered electrons (BSEs) with an annular detector. Sample block is raised by height ≥ 25 nm, and a section of that thickness is shaved off using a diamond knife mounted in the SBEM's in situ microtome. The newly exposed surface is then re-imaged. This process is repeated until an image stack is collected from the desired sample volume, 70 slices in this illustration. (b,c) Series of back-scattered electron images captured at energy E1 and E2, respectively. (d,e) 3D reconstruction of single-energy image series from (b,c), respectively. (f) Dual-energy reconstruction gives sub-slice resolution." [14]

huge data causes to exceed limits of RAM. Therefore, powerful computers are necessary to gain time. Moreover, we aimed to compare our results with results of Sanchez et al.[28]. Study of [28] uses Cryo-electron tomography(Cryo-ET) images which are the type of the TEM as dataset. This study tries to make a robust local membrane detector by using Hessian based tensor voting algorithm. We investigate source or executable codes from Internet to apply this study on SBFSEM images. Moreover, we demand them from the author of the study of [28]. However, we could not reach code. Because of the lack of time, we could not also implement algorithms in study of [28]. Furthermore, our method includes many algorithms, most of algorithms in this study are written without using functions in the existing libraries. Most of algorithms are written by using simple data structures. Main algorithms in this study are taken from the study of Tasel et al. [35]. The shortcomings of the method are strengthened and adapted for SEM images by adding algorithms to make the method robust. For better initial point determination and validation, some algorithms are added to the study of [35]. Moreover, study of [35] includes many parameters. Selection of parameters is very difficult task. Parameters in preprocessing, curve fitting and snake based shape extraction algorithms affect results extremely. Parameter selection is important task for these algorithms. Parameter selection is conducted successfully in

11

Table 1 | Comparison of volume SEM techniques

	SBEM	FIB-SEM	ATUM-SEM
Fully automated acquisition (note 1)	Yes	Yes	No
Sections preserved for post-processing and "random-access" imaging	No	No	Yes
State-of-the-art voxel size (x, y, z)	$10 \times 10 \times 25$ nm^3 (note 2)	$5 \times 5 \times 5$ nm^3	$3 \times 3 \times 30$ nm^3
Maximum slice/milling/section width	~1 mm	~20–100 μm (note 3)	~3 mm
Problems specific to each technique	Slice debris, surface charging, sensitivity to electron dose	Redeposition of vaporised material	Wrinkled sections, occasional section damage or loss
Staining	only *en bloc*	only *en bloc*	*en bloc* or section staining
Stitching and alignment	Translational shifts usually sufficient	Translational shifts usually sufficient	Demanding because of distortions and rotations
Acquisition time estimates and dataset sizes for example volumes (note 4)			
$10 \times 10 \times 10$ μm^3	2 h; 0.4 GB	39 h; 8 GB	23 h; 3.7 GB
$20 \times 20 \times 20$ μm^3	4 h; 3.2 GB	10 days; 64 GB	2 days; 30 GB
$50 \times 50 \times 50$ μm^3	22 h; 50 GB	4 months; 1 TB	6 days; 460 GB
$100 \times 100 \times 100$ μm^3	5 days; 400 GB	–	15 days; 3.7 TB
$200 \times 200 \times 200$ μm^3	5 weeks; 3.2 TB	–	8 weeks; 30 TB
$1000 \times 1000 \times 1000$ μm^3 (= 1 mm^3)	13 years; 400 TB	–	12 years; 3700 TB

Figure 9: Comparison of different types of SEM Imaging Techniques [34]

	SBF-SEM	FIB-SEM	Array tomography	TEM tomography
Instrument	JSM-7800F with Gatan 3View 2XP	JIB-4610F	JSM-7800F	JEM-1400Plus
Acquisition area (X,Y)	24×24 μm^2	18×24 μm^2	19×24 μm^2	3.5×3.5 μm^2
Acquisition depth (Z)	7.5 μm (50 nm $\times$ 150 image)	10.8 μm (20 nm $\times$ 543 image)	1.4 μm (70 nm $\times$ 20 image)	200 nm
Pixel size (X,Y)	3 nm	9.4 nm	4.7 nm	1.72 nm
Pixel size (Z)	50 nm	20 nm	70 nm	1.72 nm
Numbers of pixels	8192×8192	1920×2560	3840×5120	2048×2048
Accelerating voltage	1.0 kV	3.0 kV	7.0 kV	120 kV
Acquisition time	2.5 hour	48 hour	4 hour	1 hour

Figure 10: Comparison of Different Imaging Techniques [13]

this study. As a result, better results are obtained by using algorithms above and by making selection of parameters. Results are given as quantitatively and compared with the results obtained by the study of [35] in the results chapter. The results of the method implemented here could not compared with those of [12] and [28], since our effort to reach the authors, and obtain and run these software were not successful.

1.6   Contribution Of The Thesis

This study tries to obtain the automatic segmentation of mitochondria by using energy based algorithms. Automatic segmentation of mitochondria is important task due to contributions to the detection of diseases as mentioned in previous sections. Image characteristics changed from dataset to dataset. Therefore, every work performed in different datasets is unique and valuable. This study is one of the rare study worked on SBFSEM image as mentioned in previous section. SBFSEM is very popular imaging technique. Reasons for this popularity are stated in previous section. Therefore, this study contributes to literature by making segmentation in a more accessible dataset.

Furthermore, most of studies about automatic segmentation in SEM images use simple evaluation metrics. In some studies, segmentation of mitochondria is accepted as successful if area of mitochondria and ground truths intersects more than %70. This evaluation metric is simple and does not give the correct results. In studies of [23], [25], [41] about SEM images, metric stated above is used and their claims are based on the this metric. Therefore, their results are not reliable and do not show the success clearly. In this study, our main contributions are to use more reliable metric and to obtain acceptable results by using these metrics for SEM images.

CHAPTER 2

LITERATURE REVIEW

Although there are many studies on automatic segmentation of mitochondria by using the TEM imaging technique, there is not much research on automatic segmentation of mitochondria by using the SEM imaging technique. Working on SEM images is more difficult than working on TEM images because SEM images have in-plane lower resolution, and between slice thickness is much larger(order of magnitude) on SEM images. In this chapter, studies and their methods are expressed. Most of studies are about the automatic segmentation of mitochondria in SEM images. [30], [19], [28], [35] are studies about automatic segmentation of cristae and mitochondria using TEM images. There are limited number of studies using SEM images such as [25], [23], [31], [12], [41], [32]. Recently, some studies have been conducted on the subject of automatic segmentation of mitochondria in SEM images by using the deep neural network method such as [25], [8], [41], [19]. Moreover, most of studies mentioned below use FIB-SEM and ATUM-SEM dataset. The only work is [12] which uses SBFSEM image data as dataset as mentioned in previous chapter.

This study has advantages when compared with other studies as expressed in previous chapter. Firstly, our study is made with less effort in terms of preparation of data. Secondly, this study is performed without requiring powerful computers with high computational power. Moreover, this study uses more complex and accurate metrics as compared to other studies. Finally, this study is important because it is the one of the rare study which uses SBFSEM dataset.

A study by Jing Liu et al. [25] on segmentation consists of preprocessing, detection, segmentation of the mitochondria, and post-processing. In preprocessing step, data is augmented by flipping, rotating, and adding noise randomly to the present data. In the detection and segmentation step, improved Mask Region Based Convolutional Neural Networks(R-CNN) is implemented. This step consists of 3 main algorithms which are resnet50, Feature Pyramid Network(FPN), and Region Proposal Network(RPN). In the final step, post-processing is conducted to optimize results obtained from the R-CNN algorithm. FIB-SEM and ATUM-SEM are processed as datasets in this study. Accuracy is calculated through Jaccard Index obtained by dividing true positive results by true positive results plus false-positive results plus false-negative results. The final results are calculated as 0.849 on the FIB-SEM dataset and 0.864 on the ATUM-SEM dataset which are better than other proposed algorithms.

Another study by Weifu Li et al. [23] has 4 steps of mitochondria detection, validation for detection, segmentation, and validation for segmentation. In the detection step, the AdaBoost algorithm is trained by using ATUM-SEM stacks as training data. The ground truth data is formed by making hand segmentation with ImageJ software. In this study, if the detected area of a mitochondrion overlaps with the ground truth more than 70%, this mitochondrion is accepted as true positive. Many precision and recall results which have minimum detection times are obtained for different threshold values in AdaBoost. The recall value increases with the increasing threshold value. As a result, maximum precision is obtained if the threshold value is 2. This method is also implemented on FIB-SEM data. However, results obtained in ATUM-SEM stacks are better than results in FIB-SEM data.

Another work on segmentation of mitochondria written by Mumcuoglu et al. [30] is proposed to detect and segment mitochondria in TEM images. The algorithm consists of two main parts which are mitochondria detection and mitochondria segmentation. The detection method is based on the elliptical shape of mitochondria and their double membrane boundaries. The detection algorithm has the steps of image preprocessing, double ridge energy image computing, thresholding, selection of the largest connected component and morphological filtering, ellipse detection, and mitochondria detection. In the segmentation part, two reliable seed points are chosen, and the optimal path between these seeds is found by using the live-wire graph search algorithm. Dataset is taken from Cell Centered Database(CCDB) of the National Center for Microscopy and Imaging Research (NCMIR). Evaluations carried out on 4 Images. 52 shapes are detected as mitochondria but 10 of them are false. As a result, Dice Similarity Coefficient(DSC) is measured on average as 0.91, and Median Symmetric Boundary Error(MSBE) is measured on average as 4.9 nm.

Furthermore, in study by Sanchez et al. [28], the aim is to make a robust local membrane detector by using Hessian based tensor voting algorithm. The work is based on spreading differential information through 3D space with a tensor voting algorithm. Cryo-ET images which are the type of TEM are used in this study. The hessian tensor-based detector is used to detect ridge-like structures, and the structure tensor is used to detect edge-like structures. The proposed work consists of four steps. In first step, the input is filtered and a scale-spaced tomogram is formed. In this step, scale is set to the sigma value. Noise is eliminated by using this value, and all features smaller than sigma value is filtered. Moreover, Gaussian filter input is prepared for ridge and edge structures as well as for the third step. In the second step, the scale space of the tomogram is obtained to form hessian and structure tensors. This process is completed with the tensor voting algorithm. The third step includes local surface detection and characterization. Hessian and structure tensors are inputs for Non-Maximum Suppression Detector to detect membranes. After that gaps on the membranes are filled by the tensor voting algorithm because direct thresholding causes gaps on the membranes. In the next step, a local membrane detector is used to obtain more robust membranes. At the final step; thresholding, spreading different types of membranes, and clustering for global analysis are applied as a post-processing method. In this work, membranes of different structures are inputs. Consequently, gaps on membranes are filled by the proposed robust local membrane detector.

A method proposed by Karadeniz, M. A. and Mumcuoglu, E. U. [19] consists of 3 steps which are preprocessing, ANN(Artificial Neural Network), and directional growing algorithm. TEM images with high resolution taken from CCDB are used as dataset. As the preprocessing step, auto contrast enhancement, re-sampling, and bilateral filtering are applied to the input image. After that, ANN is applied to the preprocessed image. A feed-forward neural network with a multilayer is implemented as ANN. The backpropagation algorithm which is gradient descent based is conducted for the learning process. The directional growing algorithm which is formed with the help of the Canny Edge detection algorithm is applied to fill gaps arising from the previous step.

A method by Narasimha et al. [31] which makes the automatic texton-based joint classification and segments mitochondria in images of the melanoma cells using IA-SEM is proposed. SEM images used as dataset in this work have low contrast and low signal-to-noise ratios (SNR). Noise in the dataset is adjusted by implementing a 2D texture-preserving filter. Texton-based nearest neighbor classification, k-nearest neighbor classification(k-NN), support vector machines (SVMs) based classification, and histogram matching classification by using Neural Network(NN) are used in this article to classify images for training and testing. The accuracy test of the proposed method is conducted by comparing the results between the proposed algorithm and the manual method. As a result, results obtained in this work have a better error rate as compared to manually obtained results.

Moreover, there is another work about the segmentation of mitochondria by Giuly et al. [12]. They proposed an algorithm named as Cytoceg Process for automatic segmentation of mitochondria in 3D electron microscopic volume. SBFSEM images are used as dataset. Cytoceg process contains 3 steps for automatic segmentation. Firstly, random forest patch classification is applied to the 2D patches. 2D patches are preferred because SEM images have a gap in z-direction to obtain more accurate results. In the second step, contour-pair classification is applied to the results obtained from step 1. This classification enables to eliminate redundant parts obtained in the previous step. Finally, the level set operation is seeded with the result obtained from step 2 to obtain 3D mitochondria results. Accuracy results obtained from three different types of tissue by making 4 tests are above 90%.

A method proposed by Chi Xiao et al. [41] includes 3 steps of preprocessing, segmentation of the mitochondria by 3D Convolutional network and 3D visualization. ATUM-SEM and FIB-SEM datasets are used in this study. Image registration and histogram equalization methods are implemented for image preprocessing. In the segmentation part, residual block and 3D U-Net are combined to improve the network. Deep learning libraries from Keras and Tensorflow library are used during implementation. Data augmentation is conducted by dividing dataset into smaller sizes and flipping, rotating data to increase the size of the dataset and variation of the training data. For evaluation of the results; Jaccard Index, Dice coefficient and conformity coefficients, F1 score, precision, and recall values are calculated. When looking at results of ATUM stacks, proposed work result accuracies are more than 90% in Jaccard Index, dice coefficient, and conformity coefficient. Moreover, results have better accuracies than other proposed studies.

Another work about the segmentation of the mitochondria written by Serdar F. Tasel, Erkan U. Mumcuoglu et al. [35] consists of 8 steps. Preprocessing, ridge detection, energy mapping, curve fitting, curve filtering, snake-based shape extraction, validation, and post-processing are the steps of this study. Curve fitting and snake algorithms are energy-based methods. Curves are determined by maximizing energy on the parabola which is over curves and membranes. The snake-based shape extraction method is based on the convergence of the energy over the possible curves calculated by curve fitting methods. Moreover, the snake-based shape extraction algorithm is adapted to 3D images, and results obtained from 2D and 2.5D methods are compared to each other in this study. 2.5D results have a high precision value as compared to 2D results. The algorithms implemented in this thesis are mainly the algorithms of this study. These algorithms were adapted and optimized for SBFSEM images. The contributions of this thesis are explained explicitly in the other chapters.

The work by Julia Dietlmeier et al. [8] proposes a method which includes CNN with gradient boosting classifier. This work uses FIB-SEM data as dataset. Transfer learning is implemented to extract convolutional features. VGG which is a type of CNN is used in this study. 16 layer VGG is applied in the Keras library. The labeling of the ground truth is implemented by the Amira software tool. The quantitative results are obtained by calculating accuracy, precision, and F1 value. Training is conducted by splitting randomly training and test data. Two images are used for training, and 98 images are used for validation.These images are selected randomly. Accuracy results are calculated as 96.42% with variance 0.6% for 10 splits.

The last related study written by Nhan Nguyen-Thanh et al. [32] consists of three parts. The first part is course segmentation whose aim is to decide regions of probable mitochondria. This part is based on the features of mitochondria shape such as elliptical and circular shape. Candidate regions are used in the detection step to decide that they belong to mitochondria or not. Features such as Gabor, intensity, perimeter, and area are extracted in this part. Machine learning algorithms such as k-NN, SVM, and NN are used to combine extracted features. In the third step, whose name is fine segmentation, detected mitochondria are segmented. In this step, points not included in mitochondria are eliminated. FIB-SEM data is used as dataset. In this study, it is claimed that their proposed results have about 95% accuracy and this study is simpler than other mentioned studies such as [26] and [31].

CHAPTER 3

PROPOSED WORK

3.1 Data

In this thesis, automatic segmentation of mitochondria in SEM images is implemented as mentioned in the previous chapters. Data is collected from different types of cell images to strengthen the method. The method is applied on two different datasets with various Regions Of Interest(ROIs) to obtain and generalize the desired results.

3.1.1 Datasets

The dataset used in this thesis is taken from the CCDB. Images are gathered from SEM in this database. Many options are present in CCDB. The CCDB is an easily accessible database from the website [24]. The CCDB is supported by NCMIR, and is also a part of the Cell Image Library. This library contains images, videos, and animations of cells, capturing a wide diversity of organisms, cell types, and cellular processes. This database aims to enable advanced research on cell-related studies and contribute to the detection and treatment of diseases. Cells may be exposed to dramatic changes and modifications during their lifetime. These changes are indicators of some vital diseases. Scientists and doctors need to understand the structure and changes of cells to determine problems and to find solutions for these problems [40]. The primary objective of this database is to use cell structure for the purpose stated above.

The basename of the first dataset taken from the CCDB is 20275. It shows the hippocampus cell of a mouse. The cell body is pyramidal neuron. Two successive slices of dataset 20275 can be seen in Figure 11. Image samples of dataset 20275 have the size 3201x2021 (width × height). The number of slices and the voxel size of the dataset 20275 are 50 and 11 x 11 x 70 nm in x-y-z axis. Moreover, another dataset is used for mitochondria segmentation. The basename of second dataset taken from the CCDB is 20305. It also shows the hippocampus cell of a mouse and, the cell body is pyramidal neuron. Two successive slices of dataset 20305 can be seen in Figure 12. Image samples of dataset 20305 have the size 2271x1891 (width × height). The number of slices and the voxel size of the dataset 20305 are 24 and 2.3 x 2.3 x 70 nm in the x-y-z axis. Properties of these two datasets are given in Table 1. Datasets
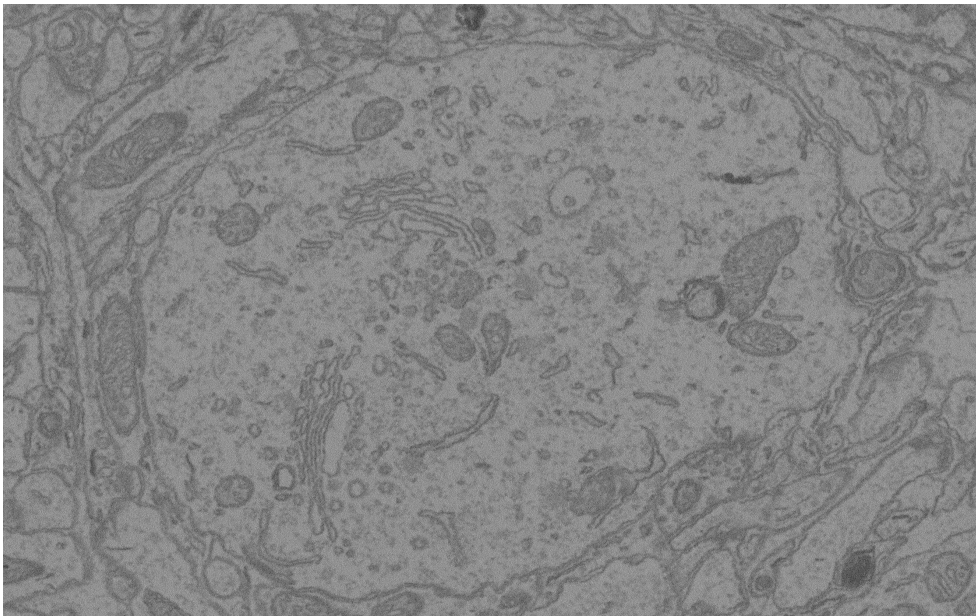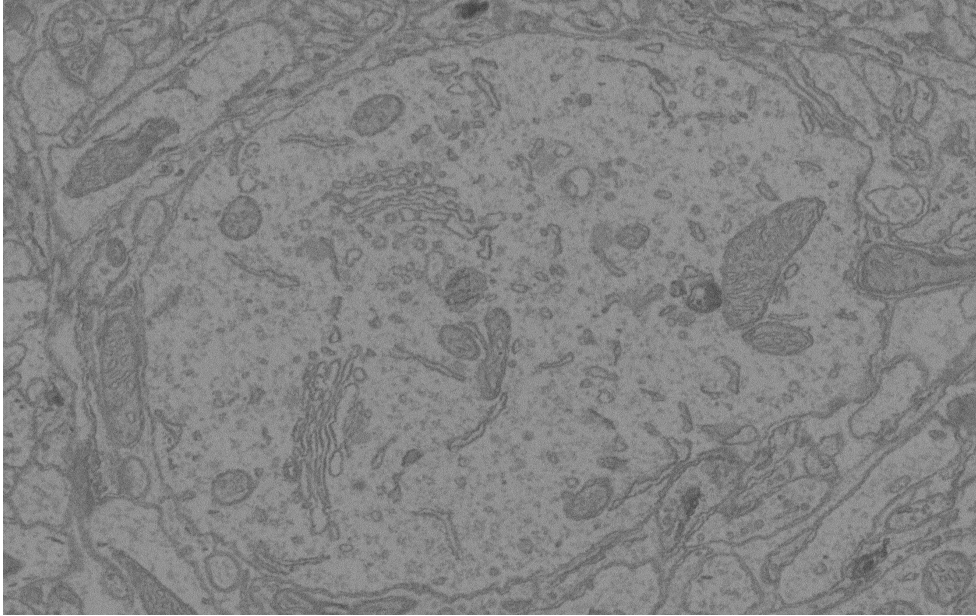
Figure 11: Succcesive Slices of SEM Image for Dataset 20275
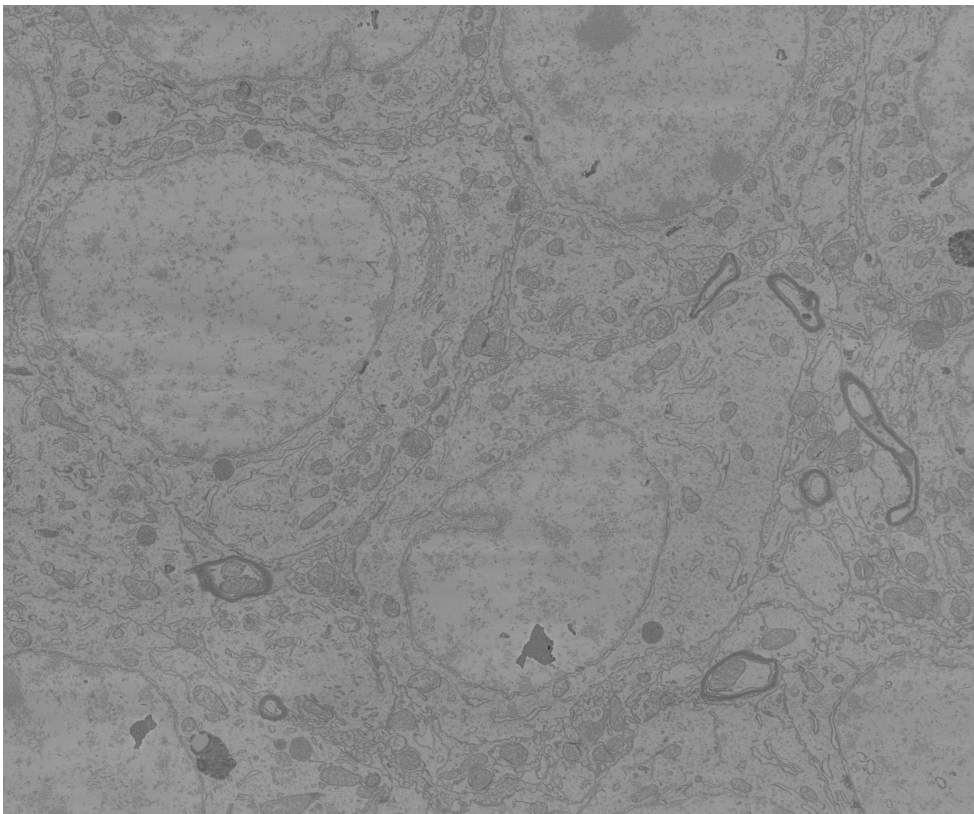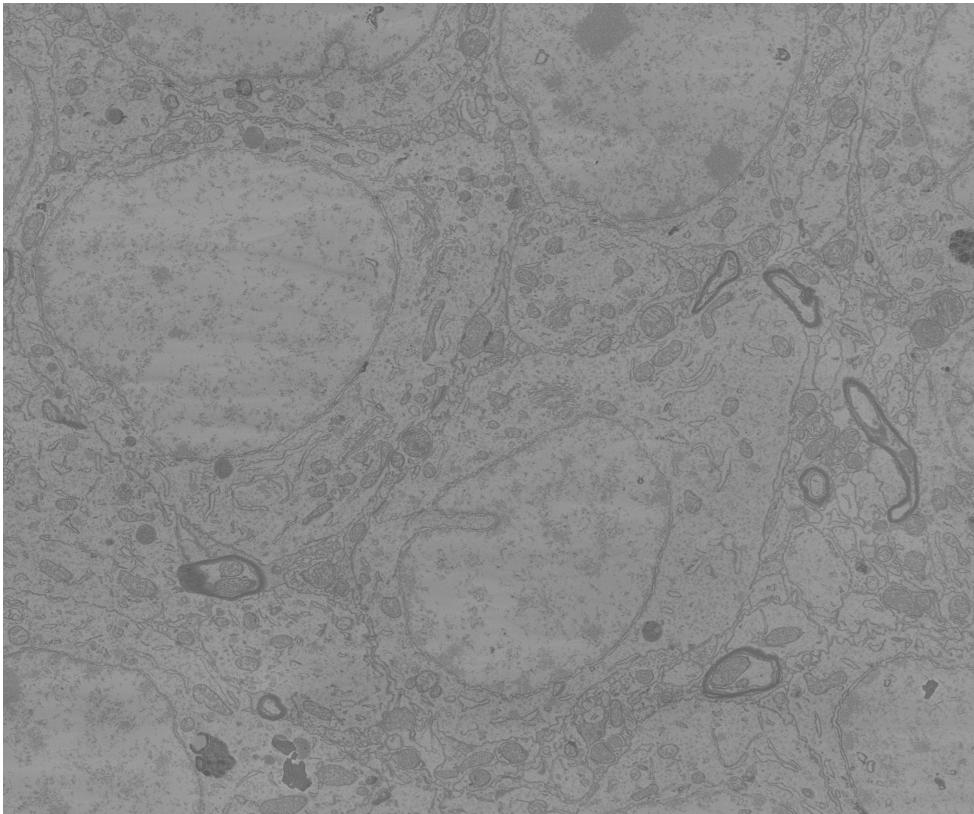
Figure 12: Succcesive Slices of SEM Image for Dataset 20305

Table 1: Properties of Datasets

Dataset Basename	Image Size (Width x Height)	Number Of Slices	Voxel Size(nm) (X x Y x Z)
20275	3201x2021	50	11 x 11 x 70
20305	2271x1891	24	2.3 x 2.3 x 70

have different resolutions, voxel sizes, and numbers of slices as seen in Table 1. Each dataset has a diversity of contrast in the image.

3.1.2 Ground Truth

The ground truth data is obtained by manually marking mitochondria membranes in datasets supplied by the NCMIR using the IMOD tool. IMOD tool facilitates image segmentation, 3D modeling and data analysis of 2D and 3D image. Moreover, IMOD tool enables user to mark and visualize mitochondria from successive slices of images in 2D and 3D format.

Ground truths for different ROIs of dataset 20275 and dataset 20305 are seen in Figure 13 and Figure 14 respectively. It is predicted that manually marking of mitochondria membranes on SEM images by using IMOD will take a lot of time because of the large number of images and pixels. Since specialists have limited time, ground truths will be marked using IMOD by the writer of this thesis. However, these ground truth markings were validated by the data provider expert in NCMIR(Guy Perkins).

3.2 Method

Many algorithms are implemented for the automatic segmentation of mitochondria in SEM images. Some of these algorithms were originally proposed and implemented in earlier study for TEM images by Tasel et al. [35]. In this thesis, some changes are made to adapt these algorithms accordingly for SEM images. The flowchart of the method can be seen in Figure 15. These steps and selection of parameters according to SEM images are very important to obtain satisfying results. Especially Histogram Equalization, Initial Point Elimination and Validation steps are very important steps for successful results. This flowchart represents the implemented algorithms. The method includes many steps. Firstly, preprocessing step is applied on the input image. Auto contrast enhancement algorithm, re-sampling, and bilateral filtering are the algorithms of the preprocessing step. After that, ridge detection and energy mapping are applied to the preprocessed image. Then, curve fitting and filtering are implemented to extract low-frequency curves. These detected low-frequency curves are used to determine initial points for snake-based shape extraction. Histogram equalized image is obtained by making histogram equalization on the bilateral image. The
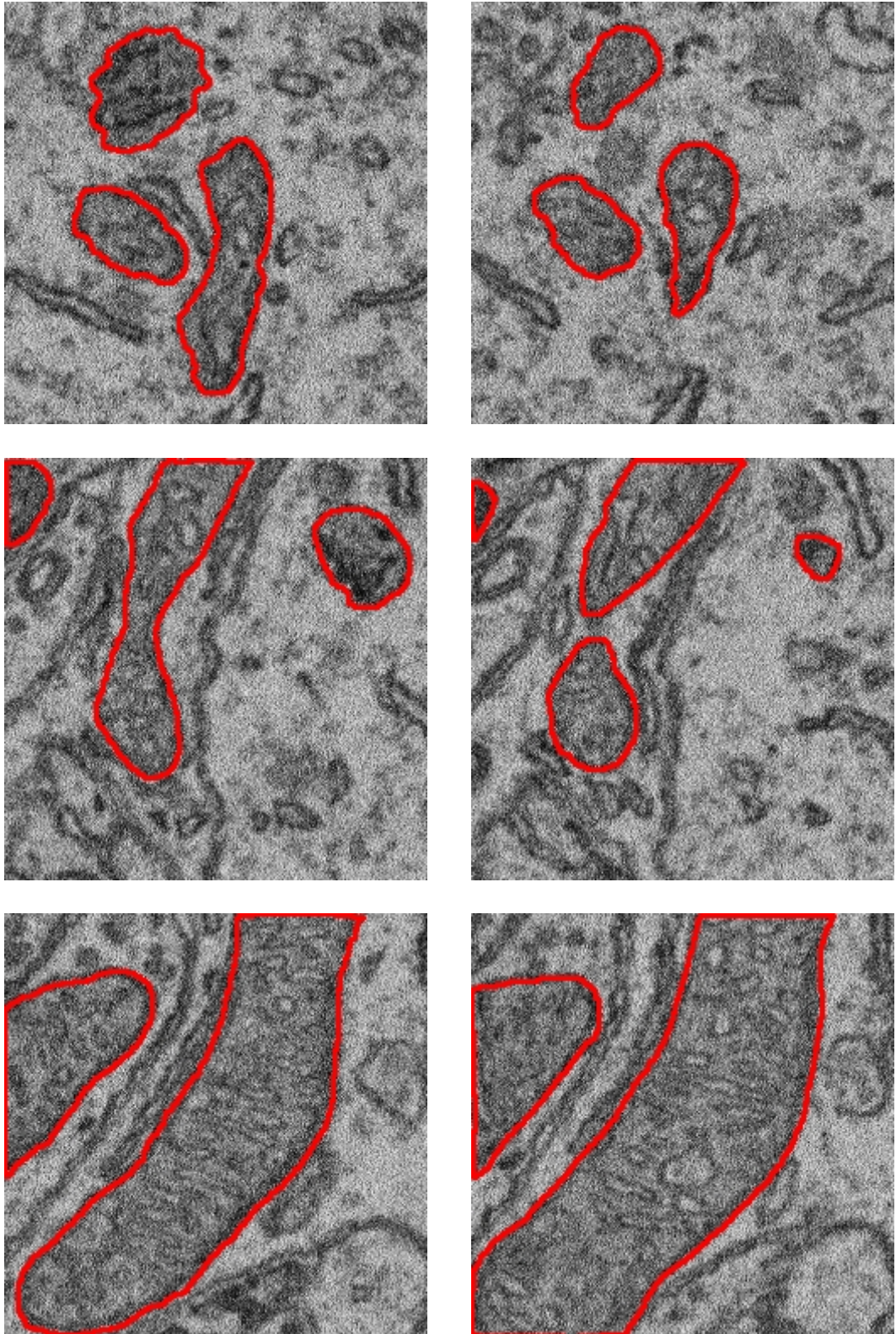
Figure 13: Ground Truths for Different ROIs of Dataset 20275
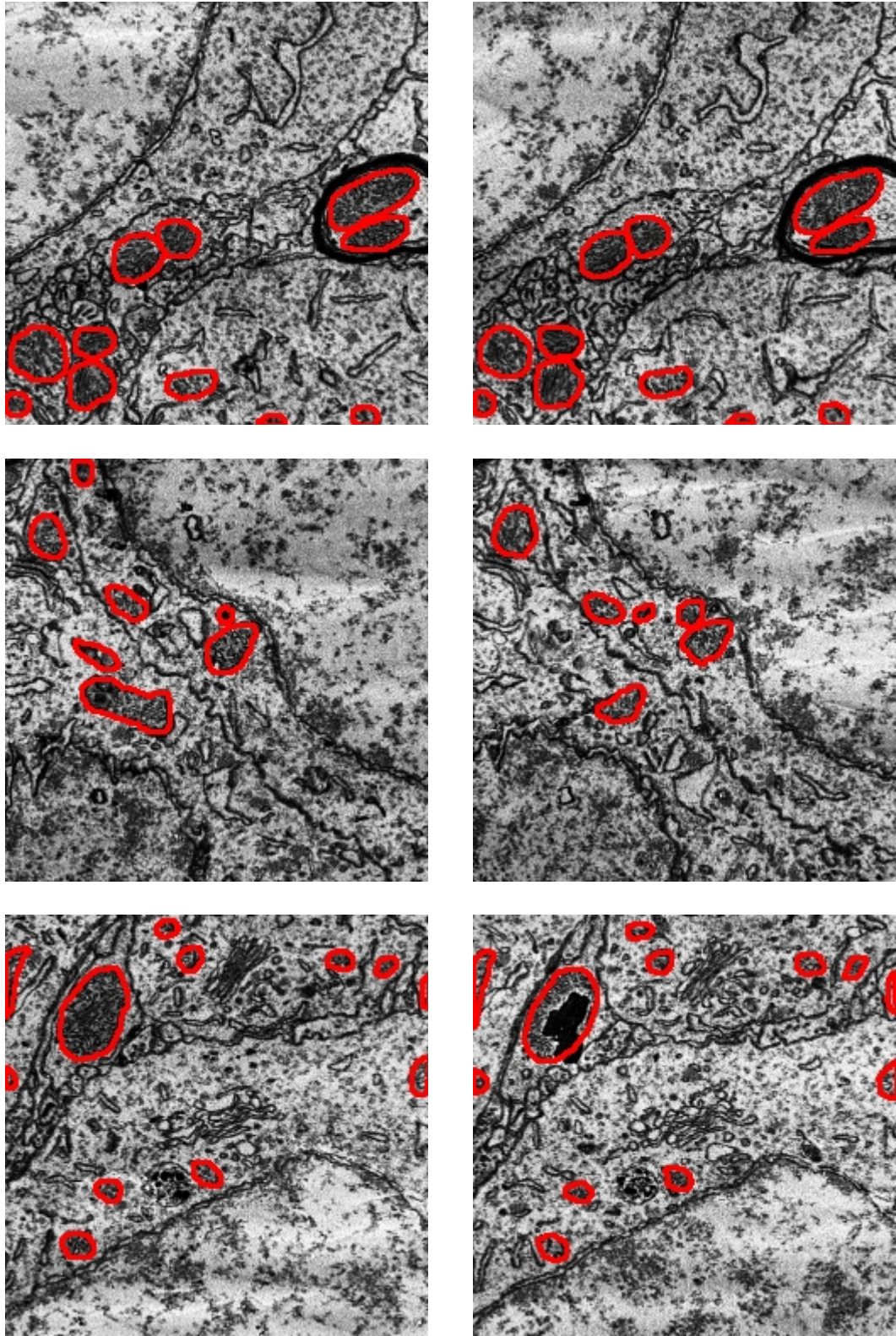
Figure 14: Ground Truths for Different ROIs of Dataset 20305
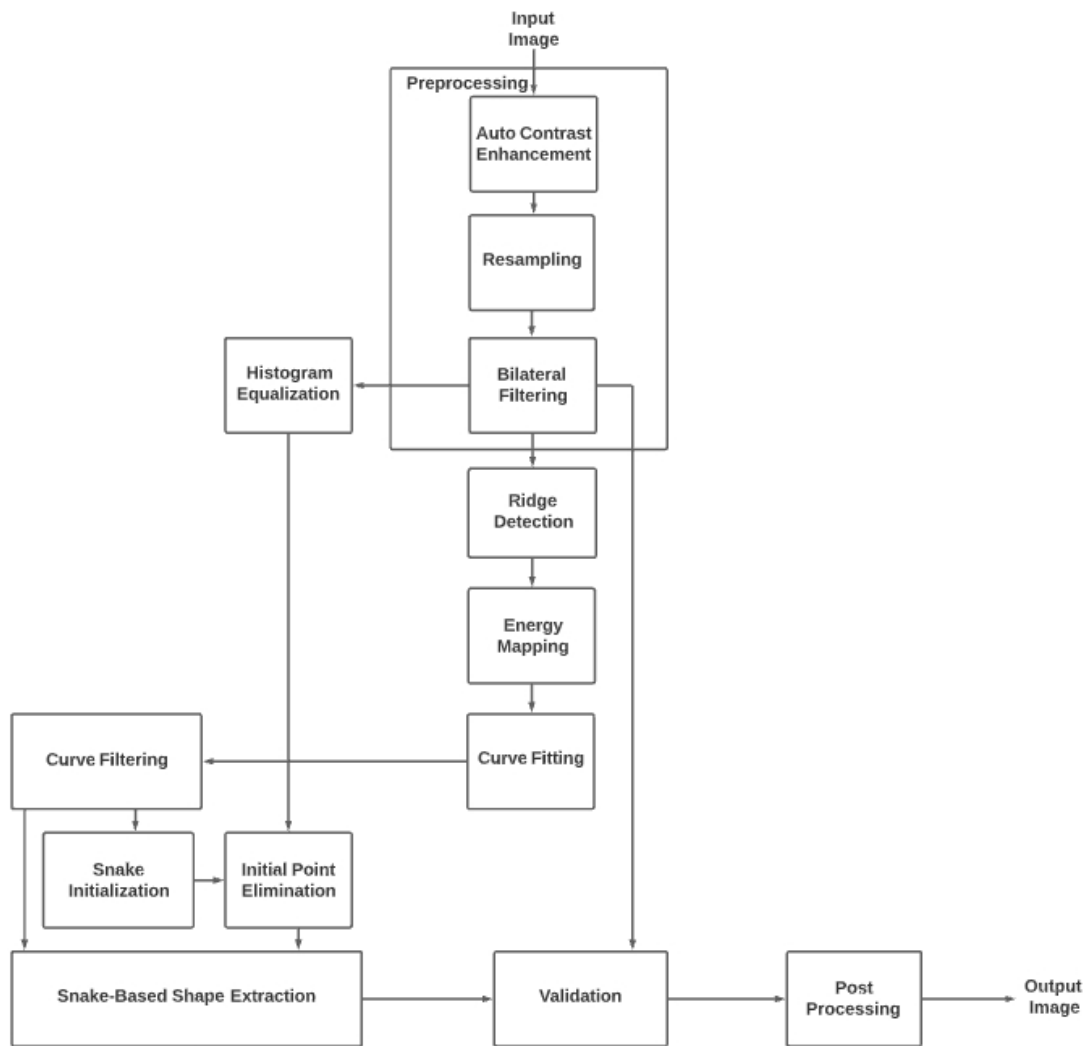
Figure 15: Flowchart of the Method

determined initial points are eliminated by using this histogram equalized image. The initial points determined after this elimination are inputs for the snake-based shape extraction. Then, the validation process follows the snake-based shape extraction to eliminate unreliable segmented snake contours. Finally, the remaining snake contours are combined by using post-processing merge algorithm.

3.2.1 Preprocessing

i. Auto-Contrast Enhancement

Reconstructed SEM images may be produced as noisy. Extremely high and low values are formed due to the nature of the creation process of the image by SEM. Instead

25
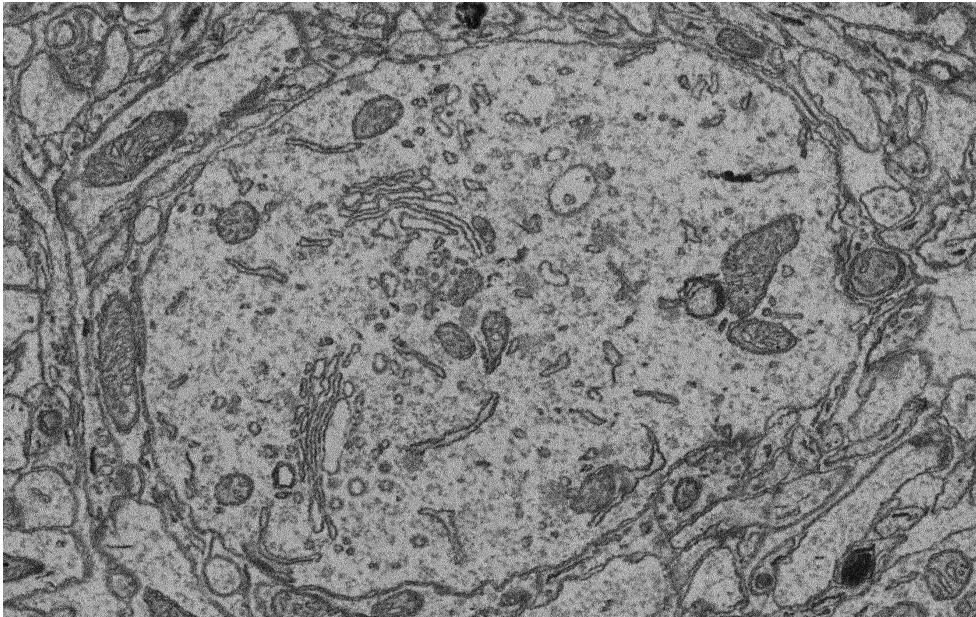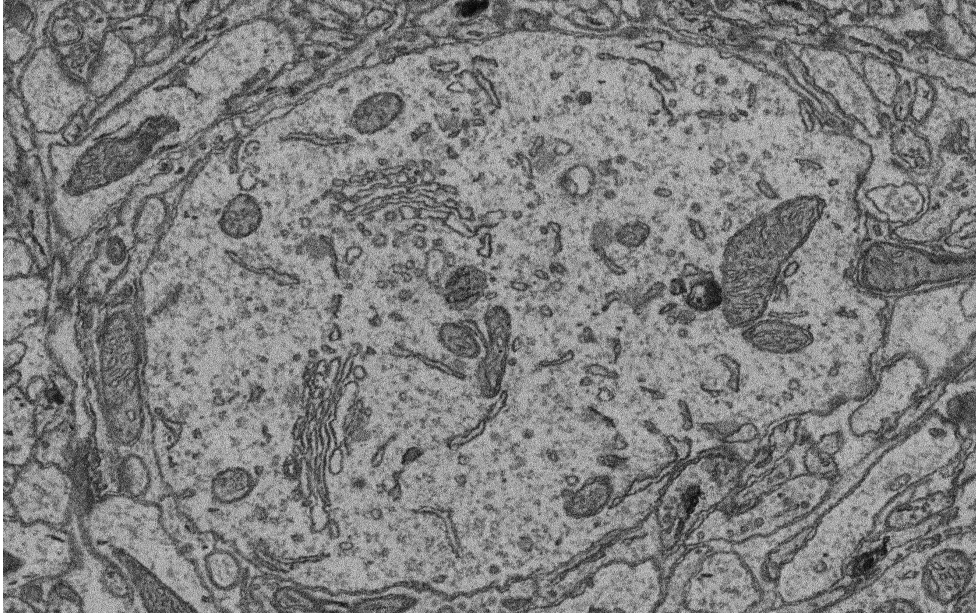
Figure 16: Two Successive Slices of Auto Contrasted SEM Image Dataset 20275
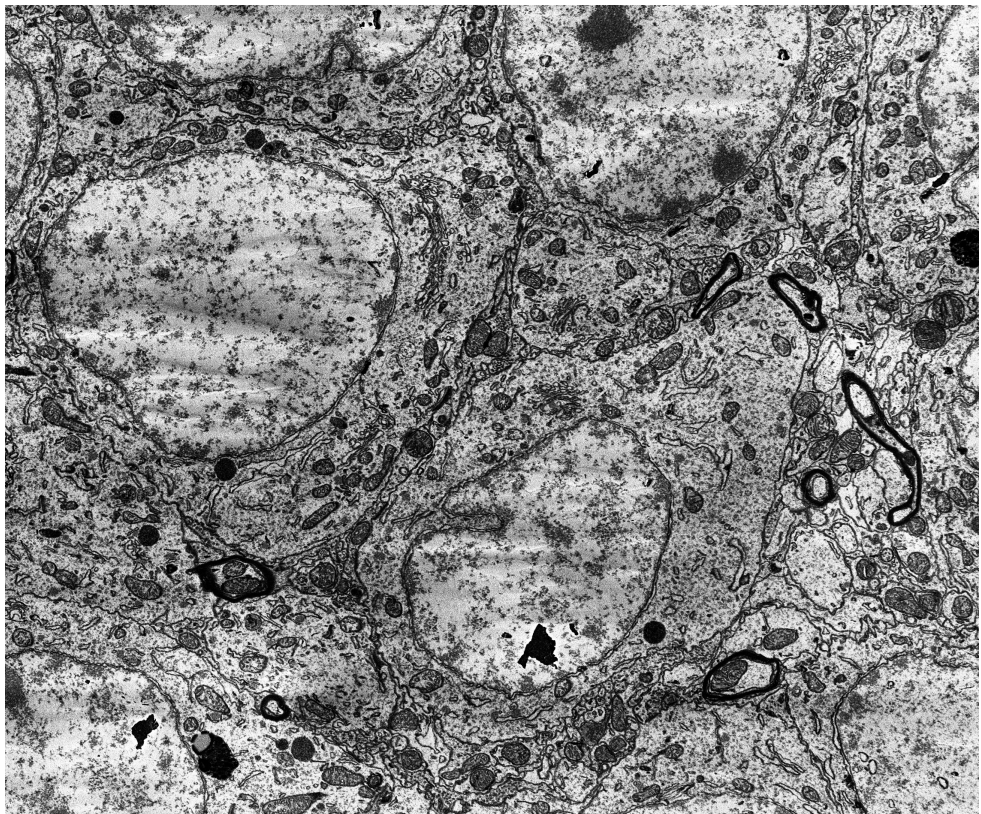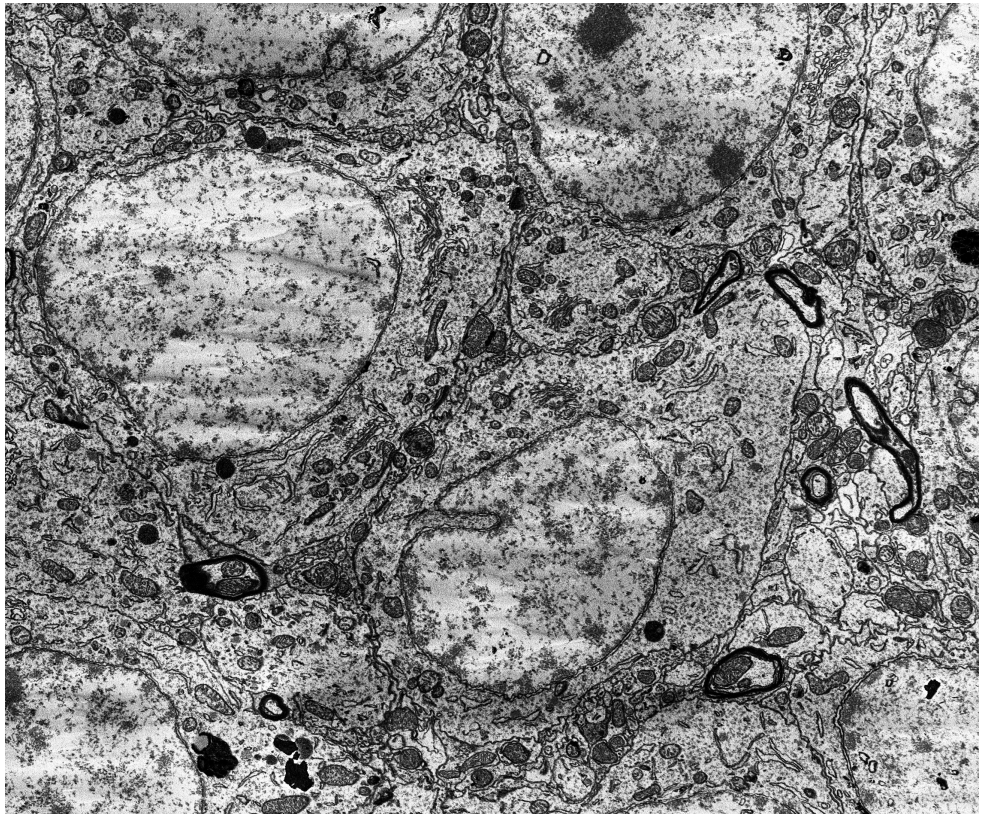
Figure 17: Two Successive Slices of Auto Contrasted SEM Image Dataset 20305

of using a simple normalization technique, auto contrast enhancement algorithm can be used to prevent this image degradation and corruption occurred due to the nature of the SEM image acquisition technique, and to improve contrast [35]. Histogram equalization is implemented as contrast adjustment algorithm by using the histogram of the image. The histogram represents how many pixels there are in the image for each intensity value. This algorithm makes re-normalization by setting gray values between 0-255. Histogram equalization tries to equalize the intensity value of the image by spreading out the maximum number of pixels. Firstly, the histogram of image is calculated for each intensity value. Then, the cumulative sum of histogram is obtained. After that, re-normalization of the cumulative distribution function(CDF) between 0-255 is acquired. Finally, a histogram equalized image is obtained by re-normalizing CDF. Auto contrasted images of slices for dataset 20275, dataset 20305 can be seen in Figure 16 and Figure 17 respectively.

ii.Resampling

After auto contrast enhancement algorithm, the re-sampling is applied to the image by interpolating and down-sampling pixels to make image membranes robust. Membrane thickness is adjusted to desired pixel size by re-sampling the image. The resampled images of slices by a factor of 0.5 (which means: a subsampling of 2-to-1) for dataset 20275 and dataset 20305 can be seen in Figure 18 and Figure 19 respectively.

iii.Bilateral Filtering

As the final step for preprocessing, bilateral filtering which is a type of smoothing algorithm proposed by Tomasi and Manduchi is applied to the image. The bilateral filter is the image filtering algorithm which preserves edges by using the intensity of the neighbor pixel nonlinearly and provides noise reduction. This filter changes the intensity of each pixel with a weighted average of intensity values obtained from neighbor pixels. The bilateral filter is the combination of two filters which are domain and range filter [37]. Equation 1 describes the formula of the bilateral filter which consists of closeness function $c(\xi, x)$, similarity function $s(\xi, x)$, intensity of the $f(\xi)$ and normalization expressed in Equation 2. The Gaussian distribution function is used as a weight function for domain and range filtering. Closeness function and similarity function are expressed in Equations 3 and 4.

$$h(x) = k^{-1}(x) \int_{-\infty}^{\infty} f(\xi) c(\xi, x) s(f(\xi), f(x)) d\xi \qquad (1)$$

$$k(x) = \int_{-\infty}^{\infty} \int_{-\infty}^{\infty} c(\xi, x) s(f(\xi), f(x)) d\xi \qquad (2)$$

28
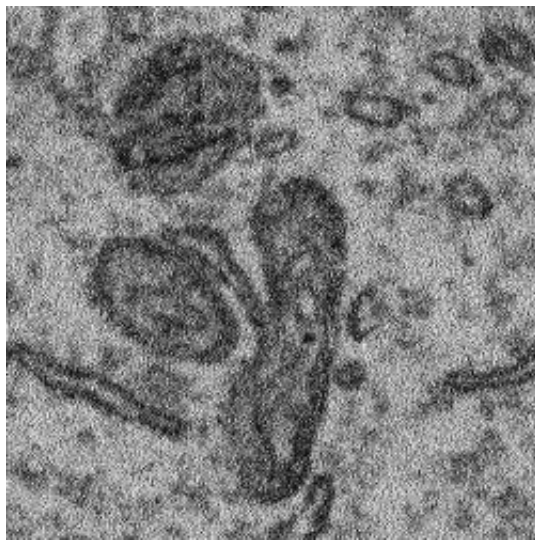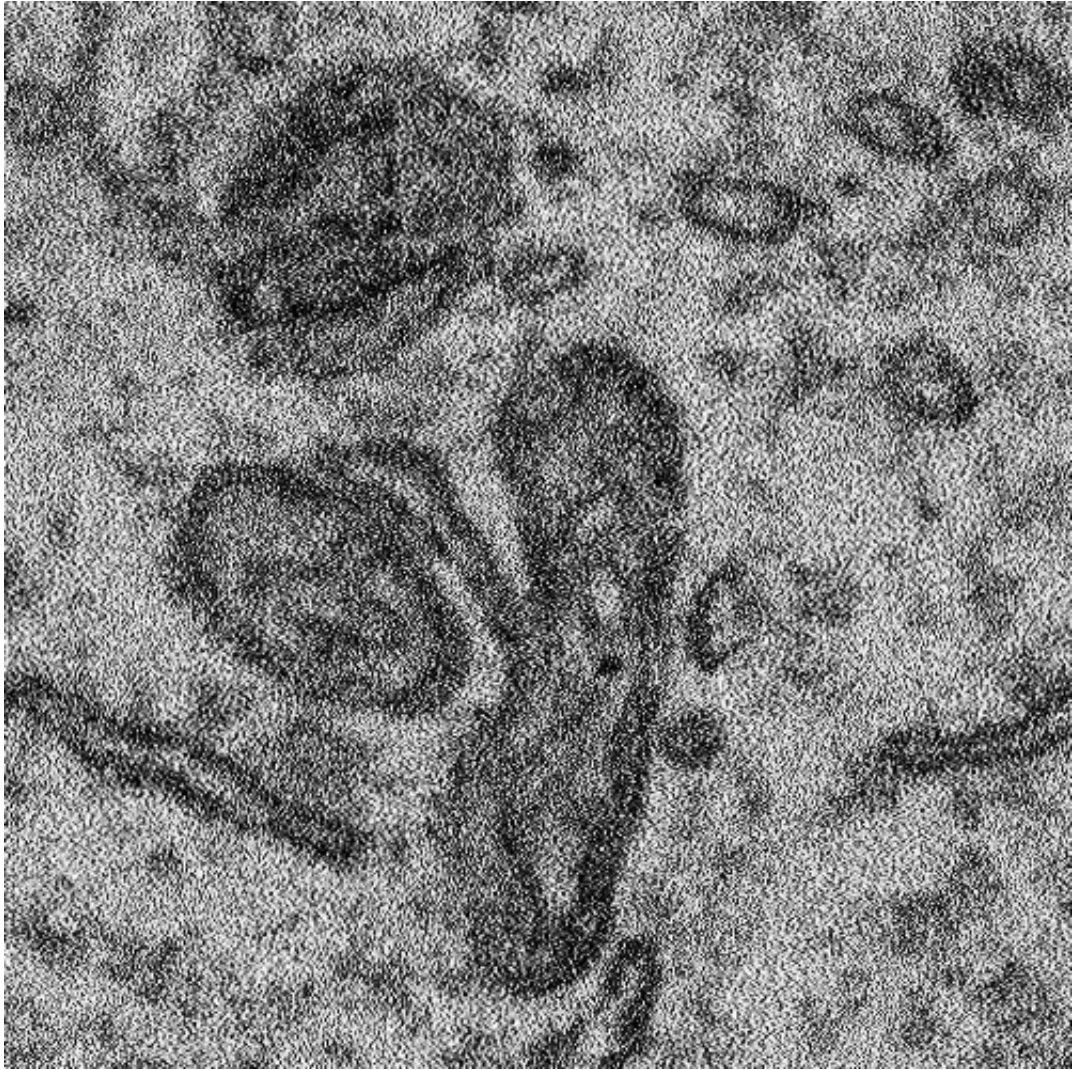
Figure 18: Selected ROI of Input Image and Resampled Image for Dataset 20275
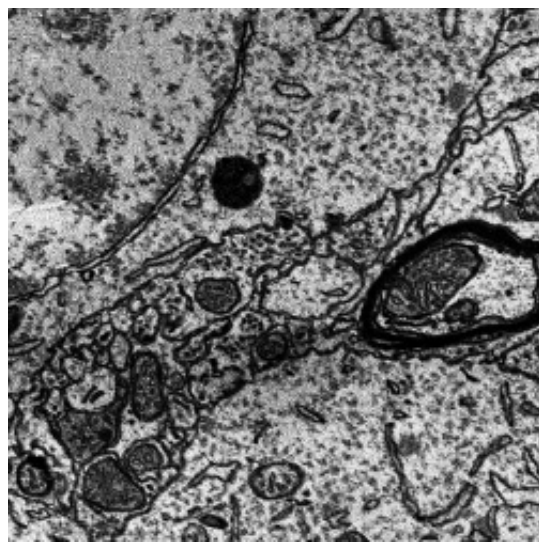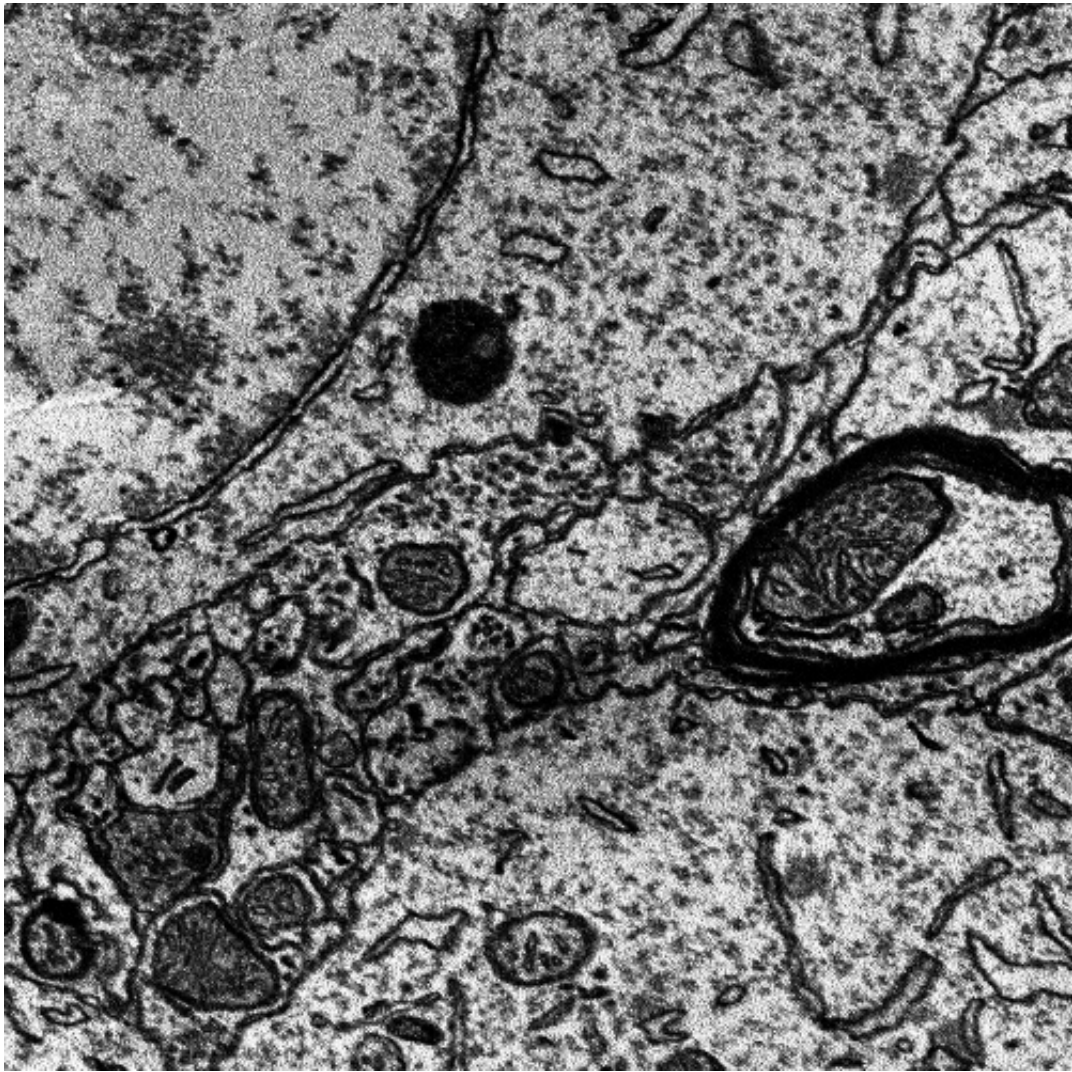
Figure 19: Selected ROI of Input Image and Resampled Image for Dataset 20305
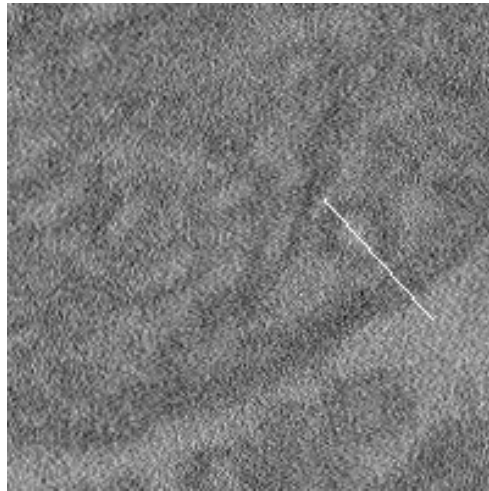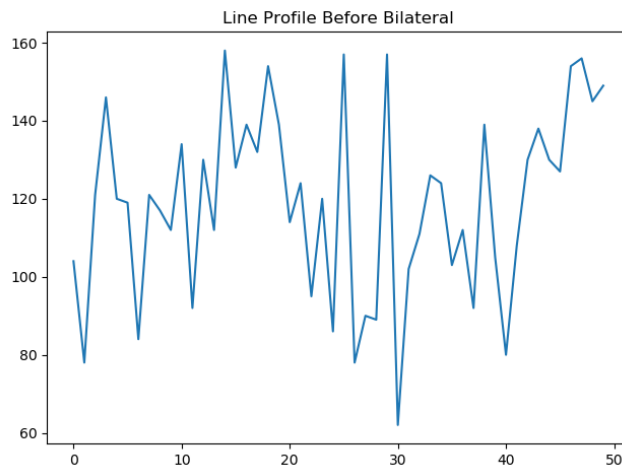
(a) Input Image

(b) Line Profile Of Input Image
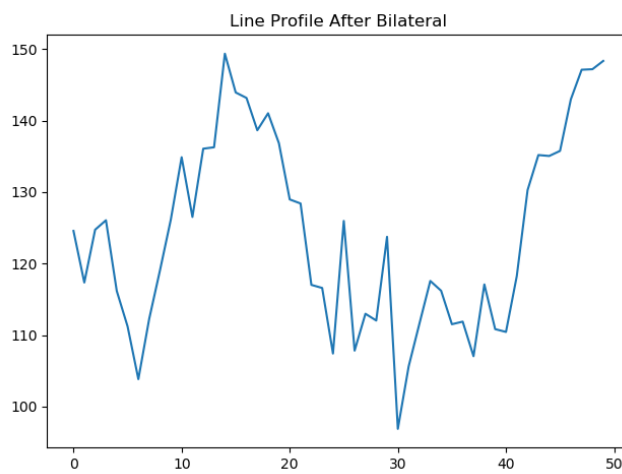
(c) Line Profile Of Bilateral Image

Figure 20: Bilateral Analysis 1

31
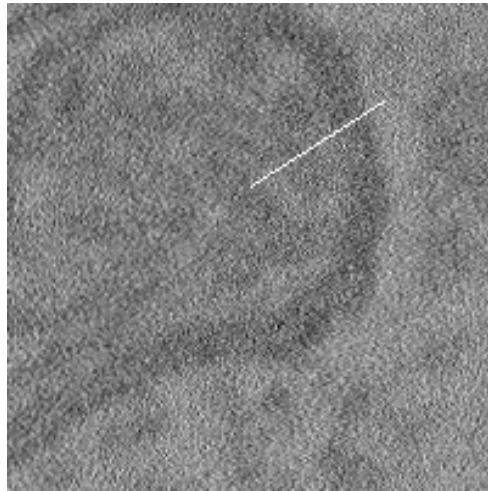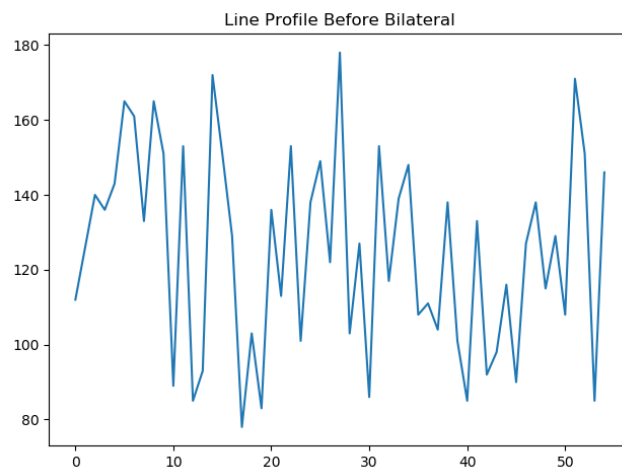
(a) Input Image

(b) Line Profile Of Input Image
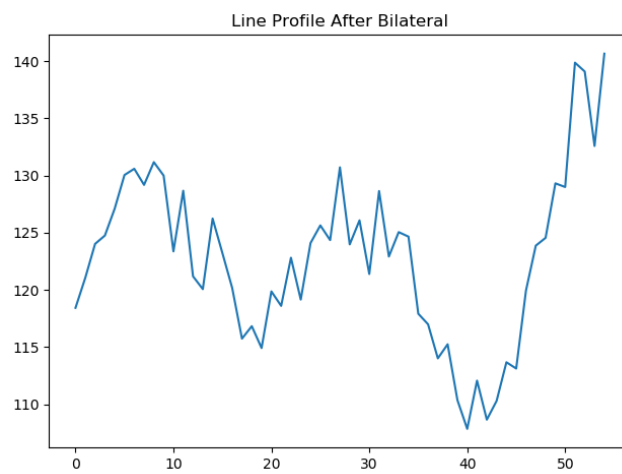
(c) Line Profile Of Bilateral Image

Figure 21: Bilateral Analysis 2

$$c(\xi, x) = e^{-\frac{1}{2}(\frac{\|\xi - x\|}{\sigma_d})^2} \tag{3}$$

$$s(\xi, x) = e^{-\frac{1}{2}(\frac{\|f(\xi) - f(x)\|}{\sigma_r})^2} \tag{4}$$

The line profile for the selected image is obtained before and after bilateral filter as seen in Figure 20 and Figure 21. The line profile includes intensity values of pixels on the line. Bilateral filter reduces noise while preserving edges. This effect can be seen in Figure 20 and Figure 21. Figure 20(a) and Figure 21(a) show the input image and line inside image. Figure 20(b) and Figure 21(b) show the line profile of the input image through the line. Figure 20(c) and Figure 21(c) show the line profile of the bilateral image for the parameters specified in Table 3 and Table 9 of results section respectively. As can be seen from the results of Figure 20 and Figure 21, bilateral filter reduces noise and increase differences between low intensities and high intensities. Moreover, it preserves edges. Figure 22 and Figure 23 shows the input and bilateral filter results of input for the selected ROI of dataset 20275 and dataset 20305 respectively. Bilateral filter causes blurring and reducing noise as seen in Figure 22 and Figure 23 for the parameters specified in Table 3 of results chapter.

3.2.2   Histogram Equalization of Bilateral Image

The histogram equalization algorithm explained in auto contrast enhancement part is applied on the bilateral image obtained in previous subsection. Histogram equalized image is used for initial point elimination for the snake method.

Input ROI Image, auto contrasted image, bilateral image and histogram equalized of bilateral image for dataset 20275 are given in Figure 24.

Histogram of the input image, auto contrasted image, bilateral image and histogram equalized of bilateral image for dataset 20275 are given in Figure 25. As can be seen from Figure 25, auto contrast enhancement spreads out histogram values between 0-255. After applying bilateral filter, graph of image has two hills because of the property of the bilateral filter. This bilateral image is used for the elimination of the snake contour in validation section. Moreover, histogram equalization of bilateral filtered image implemented to eliminate false initial points of the snake based shape extraction. Histogram equalization is applied because black regions become blacker and white regions become whiter as you can see from Figure 24. Therefore, thresholding become more effective to eliminate false initial points. These threshold values are determined by using the valley value of the bilateral image. Optimal value of threshold is determined as 110 as will be mentioned in following chapters. Moreover, results are obtained by changing threshold value in subsection 4.3.1.
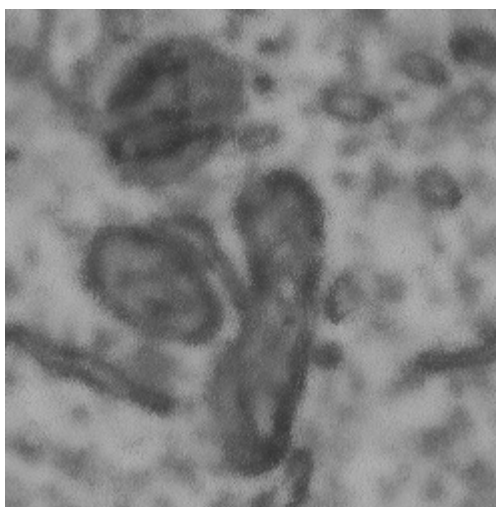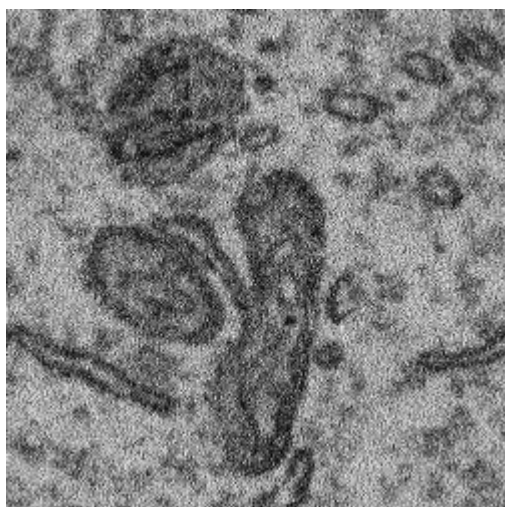
Figure 22: Selected ROI of Image Before Bilateral on the Left and Bilateral Filtered Image on the Right for Dataset 20275
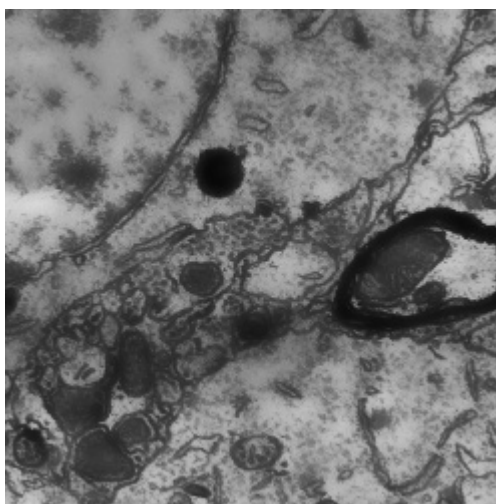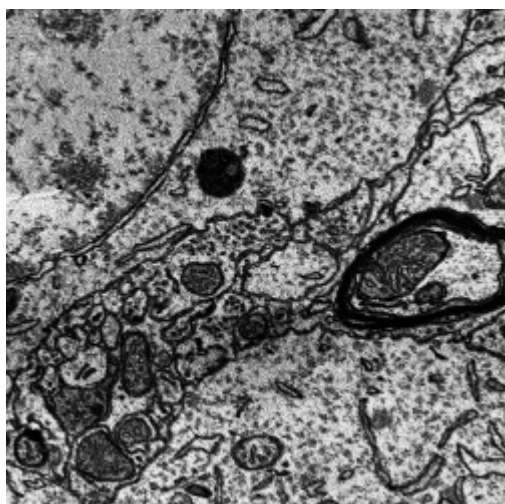
Figure 23: Selected ROI of Image Before Bilateral on the Left and Bilateral Filtered Image on the Right for Dataset 20305
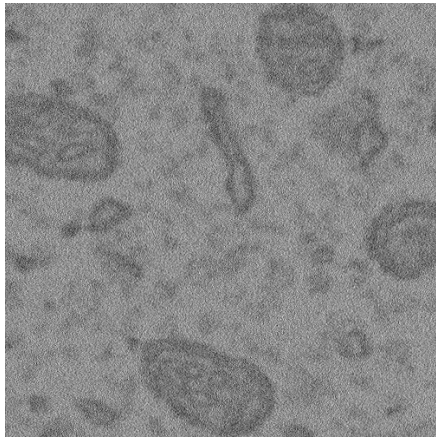
(a) Input Image
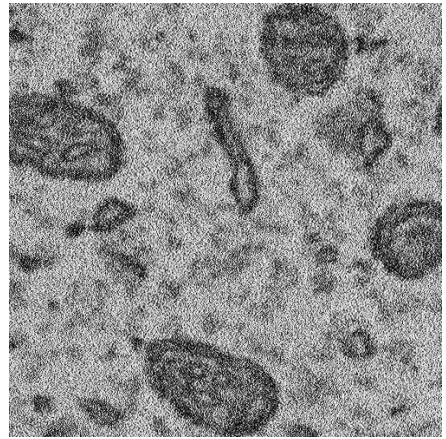
(b) Auto Contrasted Image
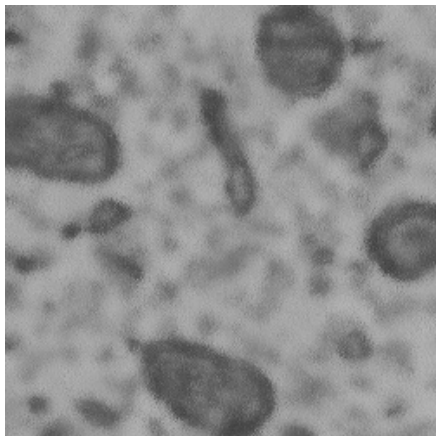
(c) Bilateral Image
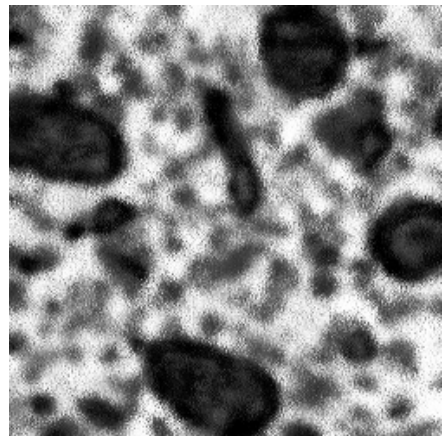
(d) Histogram Equalized Image

Figure 24: Image in (a) shows input ROI image. Image in (b) shows auto contrasted image. Image in (c) shows bilateral filtered image. Image in (d) shows histogram equalized image of bilateral image.
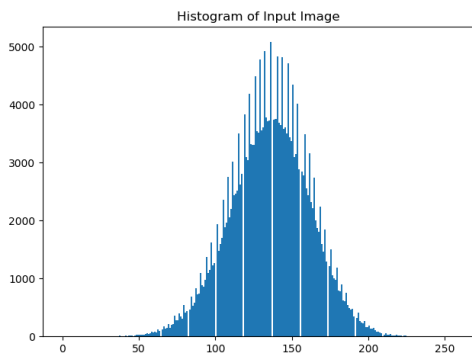
(a) Histogram Of Input Image
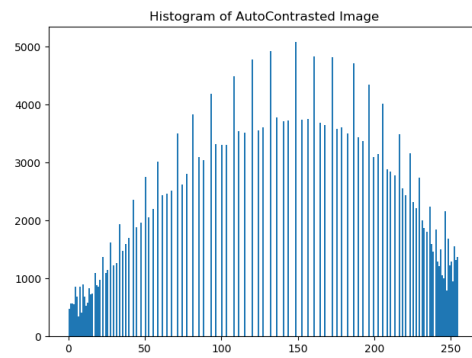
(b) Histogram Of Auto Contrasted Image
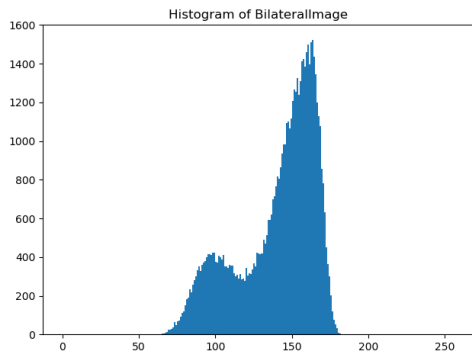
(c) Histogram Of Bilateral Image
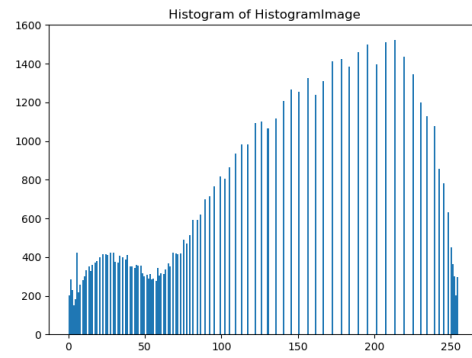
(d) Histogram Of Histogram Equalized Image

Figure 25: Histogram of Images in Figure 24. Graph in (a) shows the histogram of input ROI image. Graph in (b) shows the histogram of auto contrasted image. Graph in (c) shows the histogram of bilateral filtered image. Graph in (d) shows the histogram of histogram equalized image.
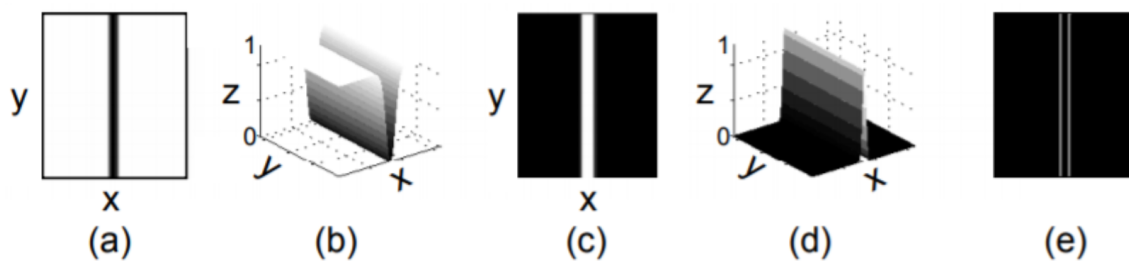
Figure 26: Valley and Ridge [27]

36

3.2.3 Ridge And Valley Detection

In this step, the aim is to detect membranes of the image which are the shape of ridge and valley. In Figure 26, (a) shows the valley and (b) shows the surface representation of the valley. (c) shows the ridge and (d) shows the surface representation of the ridge [27]. Intensity through membranes remains stable and intensity in the perpendicular direction to membrane increases. Since membranes are blacker than around pixels, valley detection is applied to the image to extract membranes in this step. A hessian-based ridge detector is applied to the image obtained from the previous subsection to detect membranes. Eigenvalues of the hessian matrix give required information about possible membranes. The idea of using Hessian Based detector is inspired from [35].

$$H = \begin{bmatrix} G_{xx} & G_{xy} \\ G_{yx} & G_{yy} \end{bmatrix} \tag{5}$$

Hessian Based Matrix is composed of $G_{xx}, G_{xy}, G_{yx}, G_{yy}$ which are second order Gaussian derivatives of the image intensity with respect to the axis specified as sub-character. Hessian Based Matrix is expressed in Equation 5. Gaussian Image is obtained by using the function in Equation 6. Input of the Gaussian function is obtained from previous subsection.

$$G(x, y) = \frac{1}{2\pi\sigma^2} e^{-\frac{x^2+y^2}{2\sigma^2}} \tag{6}$$

Window size and sigma of the Gaussian function are given as input to obtain Gaussian image. Second order derivative of the Gaussian image is obtained by using Sobel filter. Masks for Sobel filter are specified in Equation 7.

$$Gx = \begin{bmatrix} -1 & 0 & 1 \\ -2 & 0 & 2 \\ -1 & 0 & 1 \end{bmatrix}, \quad Gy = \begin{bmatrix} -1 & -2 & -1 \\ 0 & 0 & 0 \\ 1 & 2 & 1 \end{bmatrix} \tag{7}$$

First order Sobel Filters in x and y direction are specified in the Equation 7. Firstly, Gaussian image is convoluted with G_x in x direction. Then, obtained first order result is again convoluted with G_x in x direction. Finally, second order derivative of Gaussian image in x direction is obtained. G_{xy}, G_{yx}, G_{yy} are also obtained as explained above. For sobel filter implementation, opencv library is used. λ_1 and λ_2 are calculated as in Equation 8 and Equation 9 respectively.

$$\lambda_1 = G_{xx} + G_{yy} + \sqrt{(G_{xx} - G_{yy})^2 + 4 * G_{xy} * G_{yx}} \tag{8}$$

$$\lambda_2 = G_{xx} + G_{yy} - \sqrt{(G_{xx} - G_{yy})^2 + 4 * G_{xy} * G_{yx}} \tag{9}$$

As seen from Figure 27, valley occurs when $\lambda_1 - \lambda_2 >> 0$, and gap occurs $\lambda_1 \approx \lambda_2 >> 0$.. Saddle point occurs when $\lambda_1 >> 0$ and $\lambda_2 << 0$. Ridge energy is

calculated as specified in Equation 10. If λ_1 is negative, ridge energy is equal to zero. If λ_1 increases, and λ_2 is close to zero, ridge energy increases. When $\lambda_1 < 0$, and $\lambda_2 > 0$, hill-like saddle point occurs. When $\lambda_1 < 0$, and $\lambda_2 = 0$, hill occurs. When both of them are negative, peak occurs [35]. Figure 28 shows the input image and ridge image after ridge detection. Ridges of mitochondria and other structures are seen in Figure. 28.

$$r(\lambda_1, \lambda_2) = \begin{cases} \lambda_1 - \lambda_2, & \text{if } \lambda_1 > 0 \text{ and } \lambda_2 > 0, \\ \lambda_1, & \text{if } \lambda_1 > 0 \text{ and } \lambda_2 < 0, \\ 0, & \text{otherwise} \end{cases} \tag{10}$$

3.2.4 Energy Mapping

For the following algorithms, ridge direction and ridge energy are used to extract low frequency curves. X-Y plane in the image can be expressed in number of discrete direction according to a quantization number to reduce the complexity of computation and strengthen ridge directions and ridge energies in one discrete direction. 4 and 8 is tried as the quantization number in this thesis. Finally, quantization number is preferred as 4 because it gives desired results, and computational time is lower as compared to time obtained from greater numbers of quantization number. For the quantization number 4, angles between the interval $\left(-\frac{\pi}{8}, \frac{\pi}{8}\right)$ or between the interval $\left(\frac{7\pi}{8}, \frac{9\pi}{8}\right)$ is quantized as 0; angles between the interval $\left(\frac{\pi}{8}, \frac{3\pi}{8}\right)$ or between the interval $\left(-\frac{5\pi}{8}, -\frac{7\pi}{8}\right)$ is quantized as $\frac{\pi}{4}$; angles between the interval $\left(\frac{3\pi}{8}, \frac{5\pi}{8}\right)$ or between the interval $\left(-\frac{3\pi}{8}, -\frac{5\pi}{8}\right)$ is quantized as $\frac{\pi}{2}$; angles between the interval $\left(\frac{5\pi}{8}, \frac{7\pi}{8}\right)$ or between the interval $\left(-\frac{\pi}{8}, -\frac{3\pi}{8}\right)$ is quantized as $\frac{3\pi}{4}$. Total ridge energy is calculated by summing ridge energy through a window in the same interval in terms of quantized ridge direction obtained by quantization angle stated above [35]. The optimum window size parameter is decided as 12 after many trials. The window passes through all pixels images to form an energy map of $e_\theta(s)$. θ represents quantization four angles expressed in this section. s represents the pixel point in the image.

3.2.5 Curve Fitting and Filtering

Mitochondria in images consist of ellipsoidal and circular structures. These structures include parabolic curves. In this subsection, the aim is to find curves by using a parabolic arc model and a curve fitting algorithm. These algorithms are taken from [35]. A combination of parabolic curves forms membranes of mitochondria. The energy map is obtained by using the specified quantization angle in the previous subsection. This energy map shows the magnitude of energies in the specified number of quantization directions. This means that there are possible curves in the specified direction. The parabolic arc model provides extracting possible curves in this manner. The parabolic arc model is used for the curve fitting algorithm. Parabolic curves are represented by two points and height. $(x_1, y_1), (x_2, y_2)$ and h are elements of the

38
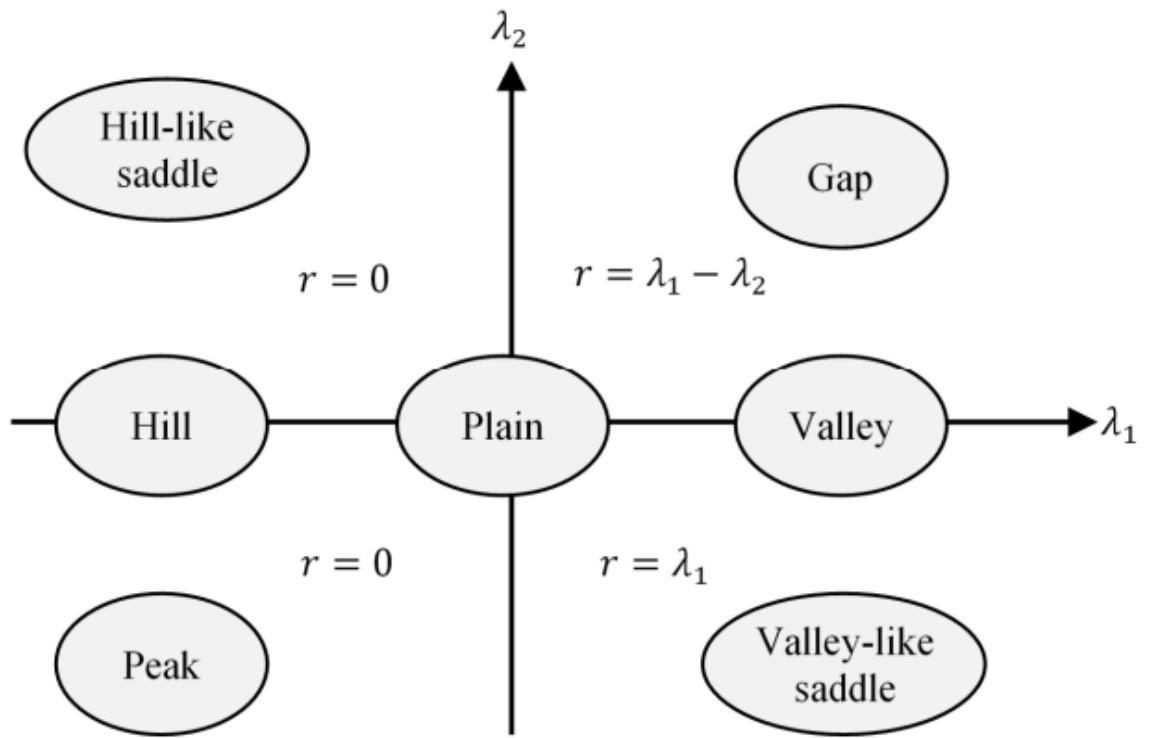
Figure 27: Topographic Shapes Obtained By Using Eigenvalues of Hessian Based Matrix [35]
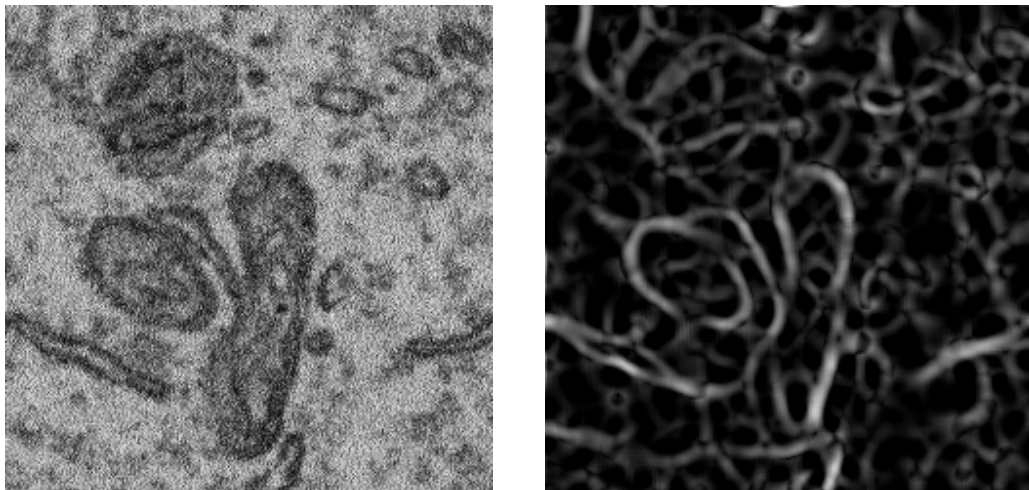
Figure 28: Input Image and Normalized Ridge Energy Image For Dataset 20275
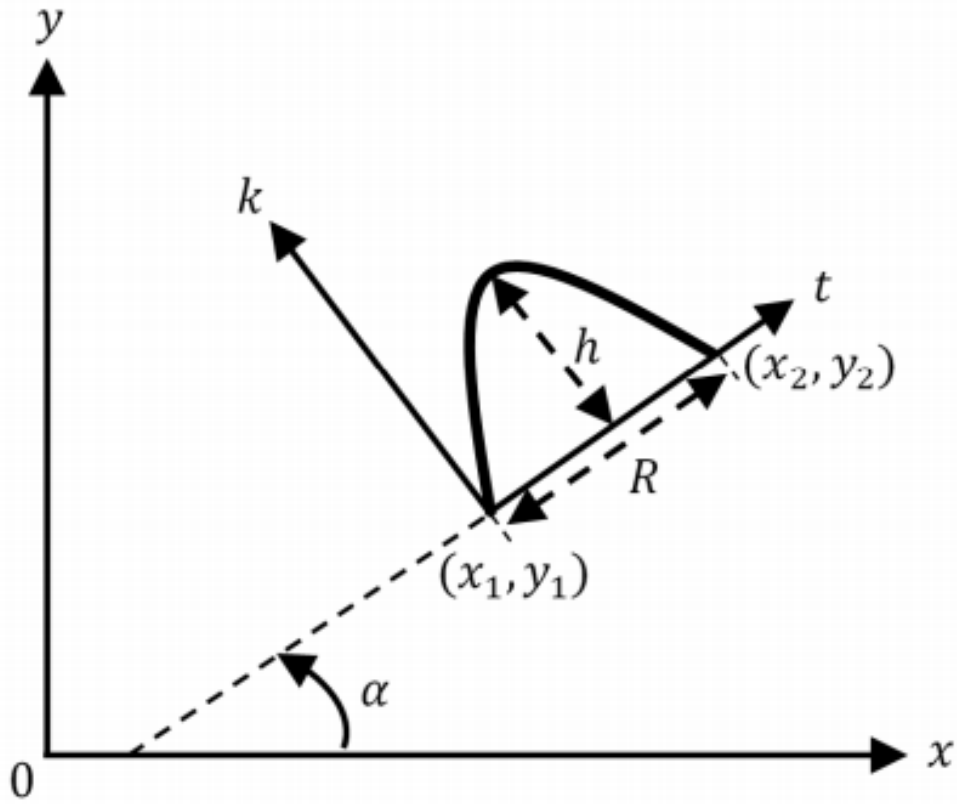
Figure 29: Parabolic Arc Model [35]

curve as seen from Figure 29. Each curve is expressed in the k-t plane by rotating the x-y plane with angle α demonstrated in Figure 29. From the parabola formula, $k = at^2 + bt$ where $b = \frac{4h}{R}$ and $a = -\frac{b}{R}$, 0 <= t <= R. a and b is obtained by applying following instructions. When the derivative of the parabola is equal to 0, the t value which makes maximum to k value is obtained. $f'(t) = 2at + b = 0$, $t = -\frac{b}{2a}$ and $t = \frac{R}{2}$ -> $a = -\frac{b}{R}$ and $h = a * \left(\frac{R}{2}\right)^2 + b * \frac{R}{2}$ -> $b = \frac{4h}{R}$.

$R = \sqrt{((\Delta x)^2 + (\Delta y)^2)}$ where $\Delta x = x_2 - x_1$ and $\Delta y = y_2 - y_1$. By using the information in Figure 29, point s is expressed as [35]:

$$s = \begin{bmatrix} x \\ y \end{bmatrix} = \begin{bmatrix} cos\alpha & -sin\alpha \\ sin\alpha & cos\alpha \end{bmatrix} \begin{bmatrix} t \\ k \end{bmatrix} + \begin{bmatrix} x_1 \\ y_1 \end{bmatrix} \tag{11}$$

40

where $cos\alpha = \frac{\Delta x}{R}$ and $sin\alpha = \frac{\Delta y}{R}$. The tangential angle φ_s of the curve on the point s calculated as follow [35]:

$$\varphi_s = \arctan \frac{y(t - \Delta t) - y(t + \Delta t)}{x(t - \Delta t) - x(t + \Delta t)} \tag{12}$$

The step size Δt is calculated as in Equation 13 to obtain equidistant points on the curve. S represents the pixel distance between two successive points. When S is selected as high, the computation time of the calculation decreases but the smoothness of the curve also decreases. Therefore, S is selected as 1 to obtain more correct results.

$$\Delta t = \frac{S}{\sqrt{1 + (2at + b)^2}} \tag{13}$$

Curve fitting is carried out by using the ridge energy map and parabolic arc model. The energy function is calculated as follow [35]:

$$E(\Omega) = \sum_{s \in \Omega} \sum_{\theta} w(\varphi_s, \theta) e_\theta(s) \tag{14}$$

Omega in Equation 14 is the set of points on the curve. It is obtained by using tangential angle φ_s calculated as in Equation 12. The weight function in equation 14 is calculated as:

$$w(\phi_1, \phi_2) = cos(2(\phi_1 - \phi_2)) \tag{15}$$

The contribution of the energy is controlled by the weight function. The weight function takes two inputs which are φ_s and ridge direction with 4 quantization angle for calculation. If the difference of these two angles is close to zero, the weight will close to 1, and it provides maximum contribution. If the difference of these two angles is close to $\pm\pi/2$, the weight will close to -1, and it provides a minimum contribution [35].

Curves are extracted by using the proposed iterative curve fitting algorithm. The proposed iterative curve fitting algorithm uses the energy function calculated in Equation 14.

The iterative curve fitting algorithm taken from the study [35] is summarized as below:
"A.Initialization: Initialize a curve as a single point for each local maximum of $max_\theta(e_\theta(s))$ satisfying $max_\theta(e_\theta(s)) > T_{RidgeEnergy}$ such that $(x_1, y_1) = (x_2, y_2) = s$ and $h = 0$.
B.Growing Phase 1:
    1. Let $(x_1^{(0)}, y_1^{(0)}) = (x_1, y_1)$, $h^{(0)} = h$ and $i = 0$.
    2. Compute $E(\Omega)$ by using Equation 14 for each parameter set candidate: $(x_1^{(i+1)}, y_1^{(i+1)}) \in \{x|x_1^{(i)} - \tau_x \leqslant x \leqslant x_1^{(i)} + \tau_x\} \times \{y|y_1^{(i)} - \tau_y \leqslant y \leqslant y_1^{(i)} + \tau_y\}$ and height $h^{i+1} \in \{a|h^{(i)} - \tau_h <= a <= h^{(i)} + \tau_h\}$ where the set of curve points Ω is formed by using Equation 11 for the current values of parameters. $(x_1^{(i+1)}, y_1^{(i+1)}, x_2, y_2, h^{(i+1)})$ and t = 0, Δt, $2\Delta t$, $3\Delta t$,.......,R.

Select the parameter set which maximizes $E(\Omega)$.

     3. If $(x_1^{(i)}, y_1^{(i)}, h^{(i)}) \neq (x_1^{(i+1)}, y_1^{(i+1)}, h^{(i+1)})$, increment i and go to step 2

     4. Set $(x_1, y_1) = (x_1^{(i)}, y_1^{(i)})$ and $h = h^{(i)}$

C.Growing Phase 2: This phase is the repetition of the first growing phase. However, the search operation is done by altering the parameters (x_2, y_2, h) this time and keeping (x_1, y_1) fixed."

τ_x, τ_y, and τ_h are the parameters used to update iterative curve fitting algorithm. These parameters enable the setting pixel size and height of the curve to obtain maximum energy, and they determine the speed of the algorithm. Parabolic Arc Model parameters (x_1, y_1), (x_2, y_2) and h are set by implementing the algorithm above according to the specified update parameters. The curve fitting process is performed by using the value of window size determined in the energy mapping step.

Detected curves may be irrelevant to membrane-like structures. They may not belong to mitochondria. Therefore, it is necessary to filter these curves which are not related to mitochondria. If κ calculated in equation 16 is greater than 1, which means that curvature is greater than 1, curves which do not belong to mitochondria are not included to the results. Moreover, curves with low energy average, low length, and low energy are also eliminated because it is expected that curves on membrane boundaries will have high energy and long length. The value which has low energy average, low length, and low energy are eliminated. Energy average is calculated as dividing total energy of the snake contour by length of the snake contour. Moreover, one other criterion is also an indicator for curves. The location of possible curves on the membrane is blacker than the outside of the membrane and the inside of the cell. Therefore, the average value of the pixel intensity on detected snake contour is also used to eliminate unreliable curves. The average value is obtained as dividing total of pixel intensity values on the detected curve by the number of points on the curve. Curves with average of pixel intensity higher than a specified threshold value are also eliminated. Curve detection before elimination can be seen in Figure 30(a). The curves after elimination for the 4 criteria above can be seen in Figure 30(b). The threshold parameters of curve elimination is given in Table 3 and Table 9. The threshold values for elimination are not set to values which provide more elimination because recall value would decrease. Therefore, only most irrelevant curves are eliminated.

$$\kappa = \frac{|h|}{R} \qquad (16)$$

3.2.6 Initial Point Determination

Snake-based shape extraction consists of two steps which are snake initialization and energy minimization. Density-Based Spatial Clustering of Applications with Noise(DBSCAN) [10] algorithm is implemented as snake initialization. Initial points are determined by the DBSCAN algorithm [10]. Previous steps in the method allow

(a) Curve Fitting Before Elimination   (b) Curve Fitting After Elimination
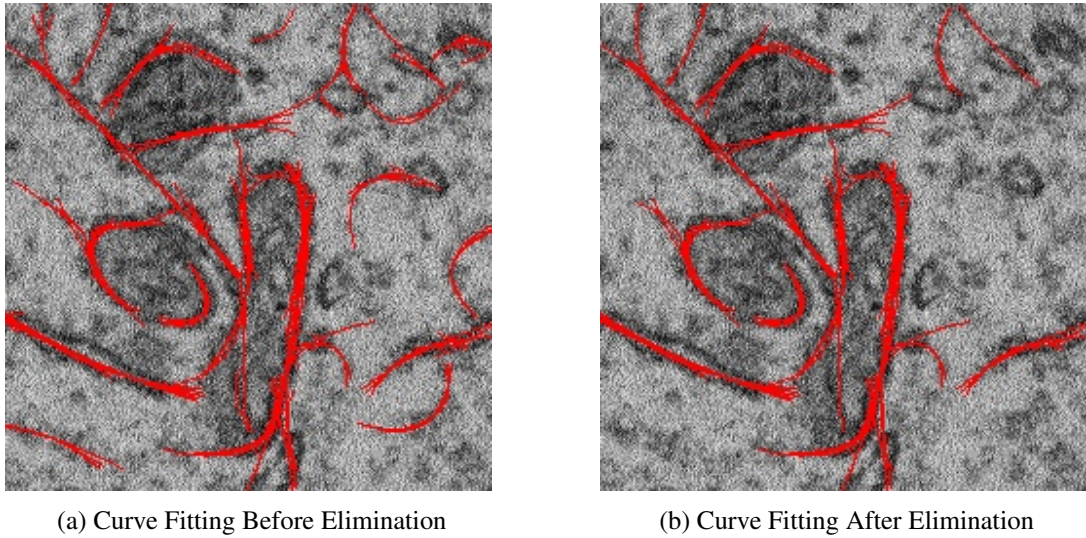
Figure 30: Image obtained after Curve Fitting before curve elimination (a) and Image obtained after Curve Fitting after curve elimination (b) for the values in Table 3

to extract curves and the energy map of the image. Detected low-frequency curves are used to determine initial points for snake-based shape extraction. DBSCAN algorithm [10] can be applied in 2D and 3D Euclidean space. In this case, it is used for 3D space.

Clustering Analysis or clustering is the grouping set of data points with similar properties. In other words, the task of clustering is to form one or more groups from data points in terms of determining criteria. The Clustering Analysis is an unsupervised machine learning algorithm. There are many clustering algorithms such as k-means clustering, mean-shift clustering, Gaussian mixture model algorithm, Agglomerative Hierarchy Clustering Algorithm, DBSCAN algorithm [10], and so on. The main idea of the DBSCAN algorithm [10] is to group data points in the high-density region of data points. DBSCAN algorithm [10] separates the points in high-density regions from the points in low density regions.

Each point in the cluster has to include a minimum number of points as neighbor points. There are two important parameters for determining a group of clusters. The minimum number of points and distance parameter between cluster points are parameters for the DBSCAN algorithm [10]. The DBSCAN algorithm [10] aims to classify core and boundary points according to the minimum number of points and distance(ϵ). If a point has at least the minimum number of points specified (including the point itself) in a distance epsilon to this point, this point becomes the core point[10].

A point is directly density-reachable from another point if the distance between these points is lower than or equal to epsilon. If a point has lower points than the minimum number of points in its neighborhood, and it can be directly density-reachable from a point by concerning epsilon and the minimum number of points; this point is the border point. Border points also belong to clusters. A point is directly density-
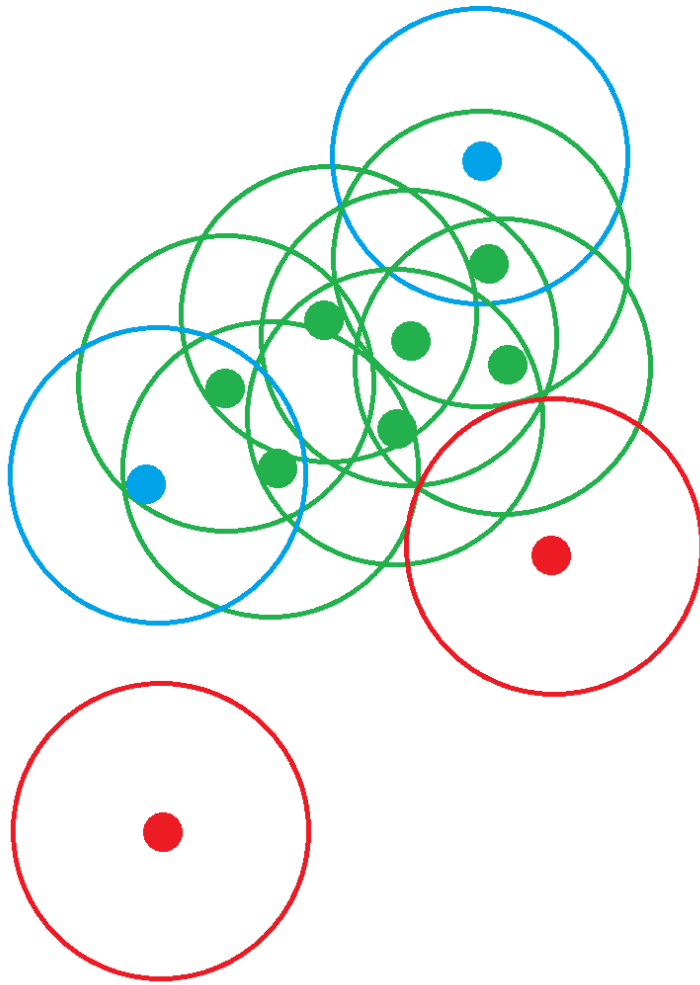
Figure 31: Example of Points for the DBSCAN Algorithm

reachable from another point if the distance between these points is lower than or equal to epsilon [10].

Figure 31 shows the example of points for the DBSCAN algorithm [10]. In this figure, the minimum number of points is equal to 4. Green points are core points because there are at least 4 points in ϵ radius. Blue points are not core points but they are also members of the cluster. Red points are noise points which are not members of the cluster.

Snake initialization is carried out by using the algorithm in [35] as follows:

" i. Determine all of the cue points for each curve detected in a given z-interval.
ii. Find all supportive points for each cue point within ϵ neighborhood.
iii. Constitute a cluster for each neighborhood having a sufficient number of points.
iv. Initialize a snake as a cylinder at each cluster center (i.e. the center of mass formed
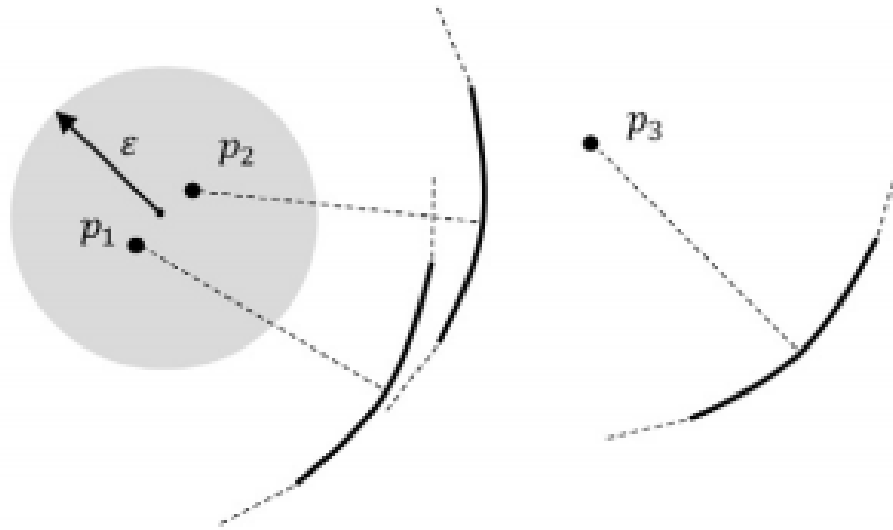
Figure 32: Cue Points [35]

by the cue point population in the cluster).
"

The start point of a parabola takes place concave part of the curve with distance of radius. It is in perpendicular direction to the tangential point of the curve. Cue point selection for a curve is performed as seen in Figure 32. Determined cue points are considered as core points if they take place in the concave sides of the parabolic curves in the distance of epsilon specified. p1 and p2 are examples of the core points as seen in Figure 32. By setting the minimum number of points and epsilon, core points are determined and the center of the gravity of the core points is finally decided as initial point. Initial points are determined by considering the specified z thickness of the algorithm. Since there is z-axis for the initial points, it is considered that snakes are initialized as a cylinder. The optimal value of minimum number of points is selected as 15 and the distance parameter epsilon is selected as 25 after many trials.

After the initial point determination, unreliable initial points are eliminated by applying a threshold to initial points by using the histogram equalized image of the bilateral image. This facilitates time-saving and correctness for segmentation of mitochondria.

As can be seen in Figure 33, the initial points for the ROI of dataset 20275 are marked and eliminated initial points can be seen in (a). Initial points in orange circles are eliminated due to thresholding process on histogram equalized Image. This elimination especially increases the precision value.

(a) Determined Initial Points   (b) Initial Points After Elimination
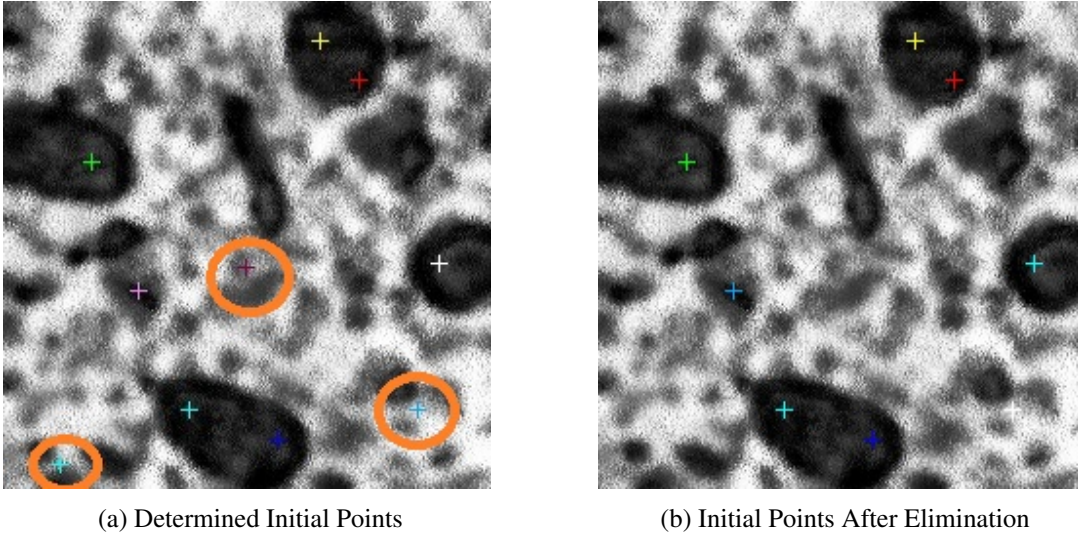
Figure 33: Determined Initial Points(a) and Initial Points After Elimination on Histogram Equalized Image(b)

3.2.7 2.5D Snake-Based Shape Extraction

Curve fitting step and previous algorithms are not enough for the segmentation of mitochondria. However, they are necessary to create inputs for the snake method. The balloon snake method [7], which is the type of active contour method, is used to segment mitochondria. The snake method's principle is based on the energy minimization of the snake model which consists of the formula as given in Equation 17.

The initialization is performed as mentioned in the previous subsection. After initial point determination, snakes are initialized by using these determined initial points. A circle with a specified radius is formed as a unit circle. This unit circle is updated to reach the final snake contour by using snake-based shape extraction algorithm.

The principle of the snake is based on energy minimizing by considering internal force related to image features which are lines and edges, external forces related to energy term obtained in the energy mapping subsection, and also inflation energy which prevents snakes from shrinking by creating outward energy. The formula of the snake model is as follow:

$$E_{snake}(\nu) = \int \Big(E_{int}(\nu) + E_{ext}(\nu) + E_{inf}(\nu) \Big) dt \tag{17}$$

46

where ν is the boundary of the membrane of mitochondria that consists of x and y coordinates along the path t. $E_{int}(\nu)$ includes the first and second derivatives of the ν in terms of t. It is computed as follow:

$$E_{int}(\nu) = \frac{1}{2}\left(w_a \left\| \frac{d\nu}{dt} \right\| + w_b \left\| \frac{d^2\nu}{dt^2} \right\|^2 \right) \tag{18}$$

where w_a is the coefficient term to set tension energy and w_b is the coefficient term to set curvature energy. The another term of Equation 17 is $E_{ext}(\nu)$. It includes the energy of the low-frequency curves computed in the curve fitting part. Formula of the $E_{ext}(\nu)$ is as follow:

$$E_{ext}(\nu) = -w_c \sum_{p \in C_L} E_{curve}(x, p) \tag{19}$$

where w_c is the coefficient term to set energy of the curves on snake contour.C_L is the set of low frequency curves. $E_{curve}(x, p)$ is calculated as follow:

$$E_{curve}(t, p) = \begin{cases} \frac{E(\Omega)}{|\Omega_p|}, & \text{if } t \in \Omega_p \\ 0, & \text{otherwise} \end{cases} \tag{20}$$

where t is the image pixel point. Ω_p is the set of points on the parabola p and $|\Omega_p|$ gives number of points on the parabola. The last term of Equation 17 is $E_{inf}(\nu)$. It is the inflation energy which creates outward energy. The external energy has the negative sign because the snake aims to minimize energy on membrane boundaries by providing with converging on the points which the curve energy is calculated as maximum. The following formula is used to update snake energy in the 2D snake method:

$$\nabla E_{snake} = \nabla E_{int} + \nabla E_{ext} + \nabla E_{inf} \tag{21}$$

The ∇E_{snake} term is tried to be minimized by using iterative calculations until reaching convergence. Convergence is checked for each iteration. Convergence criterion is checked by using the snake area. The snake area is calculated for each iteration. Moreover, the absolute difference of area for the two successive iteration is calculated. If the average of these values for the last specified number of iteration is lower than the specified number then it is accepted as convergence occurs.

$$\nabla E_{int} = -w_a \frac{\partial^2 \nu}{\partial t^2} + w_b \frac{\partial^4 \nu}{\partial t^4} \tag{22}$$

∇E_{int} is calculated in 2D as in Equation 22. It is computed by using 5 successive points on the snake. ∇E_{ext} is calculated by taking derivatives of E_{ext} in terms of x and y as seen in Equation 19. ∇E_{inf} is the outward inflation energy calculated as:

$$\nabla E_{inf} = -w_d \vec{N_\nu} \tag{23}$$

where $\vec{N_\nu} = \frac{\nabla P}{\|P\|}$. P is the unit normal vector at the boundary ν [7]. w_d is the coefficient term to set inflation energy. This energy prevents snake from shrinking. The inflation energy pulls the snake from initial unit circle to mitochondria membranes. When snakes come to membrane boundaries, it is expected that convergence occurs near to the membrane structure. If w_d is set as small value, small mitochondria in terms of area are detected. If w_d is set as high value, large mitochondria in terms of area are detected. For this reason, iterative snake calculation taken from [35] is implemented by using different w_d. It is set to different values to detect different size of mitochondria. If w_d is selected as excessively high value, snake contour may exceed the boundary of mitochondria. Snake contour may not be held on mitochondria because high value of w_d creates strong force through the outside of the membrane [35]. This situation have been considered, and w_d parameter is selected accordingly. If the excessive force occurs, formed snake contours will eliminated in validation step. The iterative model taken from [35] to extract mitochondria is proposed as follows:

"I. Repeat the following sub-steps for each parabolic arc:
      i. Initialize w_d with a small value.
      ii. Initialize the snake nearby the vertex of the parabolic arc as a unit circle.
      iii. Execute the snake algorithm.
      iv. If a different boundary is obtained, save the snake boundary.
      v. Increase w_d.
      vi. If w_d is smaller than a threshold (T_{inf}), go to step ii.
II. Use the saved snake boundaries as candidate shapes for the next stage. "

The algorithm stated above is implemented by using the snake algorithm for different values of w_d. w_d is started from low values to high values to extract mitochondria.

The algorithm is implemented by using low-frequency curves detected in selected ROI. Detected curve segments may be weak. Moreover, false initialization causes the false detection of mitochondria boundaries. If the initialization of snakes occurs outside of the membrane of mitochondria, snake contour may not be held on membranes. As a result, the validation process is proposed to reduce the false detection number of mitochondria. The validation aims to increase the performance of the segmentation. The vector of snake contour is updated by using the following equation:

$$\nu_{i+1} = \nu_i - \gamma * \nabla E_{snake}(\nu_i) \tag{24}$$

where γ is the step size. γ is calculated as in Equation 25 to prevent the snake from exceeding the boundary. $|\nabla E_{snake}|$ is taken as the maximum value of ∇E_{snake} on the curve point of the snake.

$$\gamma = \frac{1}{|\nabla E_{snake}|} \tag{25}$$
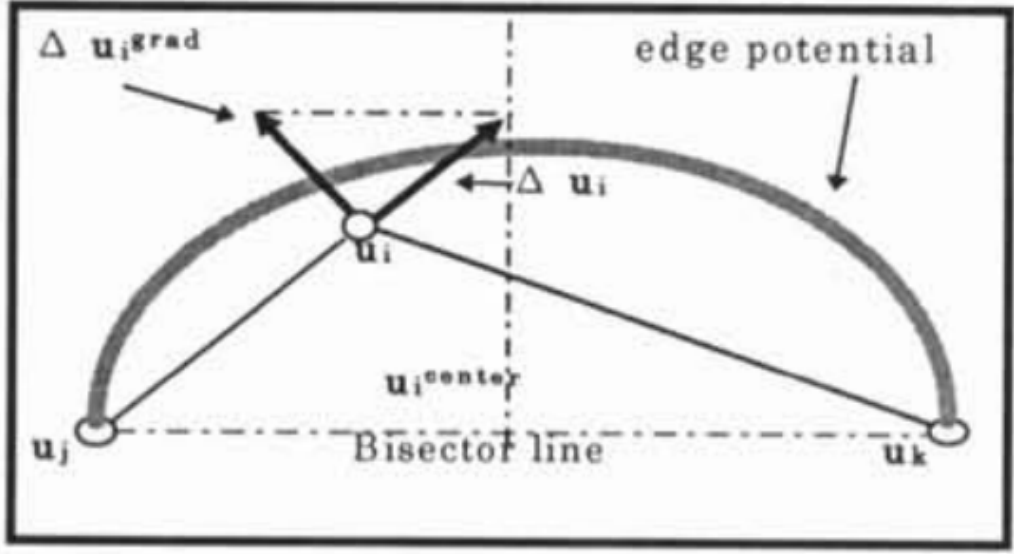
Figure 34: Motion Correction Vector[39]

While the update equation is being calculated, the distance between successive points is different for the each calculation according to previous concept. Therefore, an equidistant correction is implemented to solve this problem. From the study of [39], equidistant correction is implemented by considering the following principle. It is stated that "Our method of achieving equidistance is based on a very simple but important property: All the control points are equidistant only when they are on the bisector line of its neighboring two control points." The motion vector is modified for each control point to guarantee that they are on the bisector line. The final motion vector Δu_i is calculated as follow:

$$\Delta u_i = \Delta u_i{}^{grad} + \frac{(u_k - u_j)^t(u_i^{center} - (u_i + \Delta_{u_i}^{grad}))}{\|u_k - u_j\|^2}(u_k - u_j) \qquad (26)$$

$$\text{where} \quad u_i^{center} = \frac{u_j - u_k}{2} \qquad (27)$$

All components in Equation 26 are seen in Figure 34.

The snake model in 2D is extended to 3D as in study of [35]. The 3D model also consists of the three energy terms which are internal energy, external energy, and inflation energy terms. The 3D model includes the vertex point in the (x,y,z) direction and active forces are implemented by considering the x-y plane and z plane [2]. This means that snake contour extends in the z-direction and x-y direction until convergence occurs on the boundary. The quasi-3D (2.5D) approach in which the snake model is implemented in this thesis proposed by [35]. This model is implemented in 3D space as a stack of 2D snakes. The internal force is calculated by considering vertices in the trajectory of x-y plane and z plane. The external and inflation forces

49
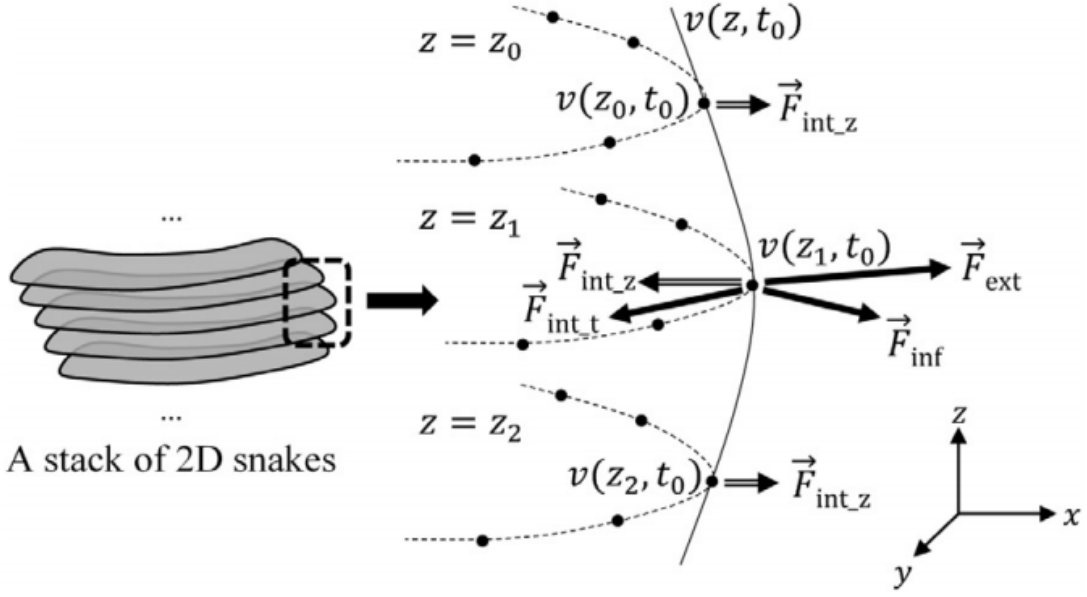
Figure 35: A stack of snakes and acting forces on a vertex of the snake[35]

are calculated as in the 2D snake model. The internal energy term becomes as in 2.5D approach:

$$E_{int} = \frac{1}{2}\left(- w_{at}\left\|\frac{\partial \nu}{\partial t}\right\|^2 + w_{bt}\left\|\frac{\partial^2 \nu}{\partial t^2}\right\|^2 - w_{az}\left\|\frac{\partial \nu}{\partial z}\right\|^2 + w_{bz}\left\|\frac{\partial^2 \nu}{\partial z^2}\right\|^2 \right) \qquad (28)$$

The parameters $w_{at}, w_{bt}, w_{az}, w_{bz}$ control tension in x-y plane, curvature in x-y plane, tension in z plane and curvature in z plane respectively. $v(z,t) = (x_{z,t}, y_{z,t})$ which can be also seen in Figure 35 represents a 2D point on the snake boundary for the slice z. Since v(z, t) represents a 2D point on the snake boundary for the slice, E_{int} in Equation 28 produces 2D vectors arisen from the forces $\vec{F_{int\_t}}$ and $\vec{F_{int\_z}}$ as seen in Figure 35. Formula of the force is expressed as $\vec{F} = -\nabla E$. $\vec{F_{int\_t}}$ is corresponding to first two terms of the Equation 28, $\vec{F_{int\_z}}$ is corresponding to last two terms of the Equation 28. The update energy term of the internal energy is calculated as in Equation 29. By considering internal energy, external energy and inflation energy, the update term can be expressed as in Equation 30 for 2.5D snake calculation.

$$\nabla E_{int} = w_{at}\frac{\partial^2 \nu}{\partial t^2} + w_{bt}\frac{\partial^4 \nu}{\partial t^4} + w_{az}\frac{\partial^2 \nu}{\partial z^2} + w_{bz}\frac{\partial^4 \nu}{\partial z^4} \qquad (29)$$

$$\nabla E_{snake} = \nabla E_{int} + \nabla E_{ext}^{(z)} + \nabla E_{inf} \qquad (30)$$

$\nabla E_{ext}^{(z)}$ is the external gradient energy calculated by considering derivatives of energy through slices in z axis. The calculation of $\nabla E_{ext}^{(z)}$ is performed as mentioned in 2D

snake model. ∇E_{inf} is the outward inflation energy term also calculated as in 2D Snake Model like $\nabla E_{ext}^{(z)}$.

3.2.8 Validation

The validation step is necessary to increase the accuracy of mitochondria segmentation by eliminating unreliable segmentation of mitochondria. Mitochondria have distinctive features as compared to other structures in the cell. These features are important for the validation process because they enable mitochondria to have discriminating properties. In this thesis, two features are used to validate segmented mitochondria obtained from previous steps. The average intensity of the snake contour and the inner average intensity of the snake contour are used for validation steps. The average intensity of the snake contour is calculated as dividing total intensity of all pixels on the snake contour by length of the snake contour. The inner average intensity of the snake contour are calculated as dividing total intensity of all pixels which take place inside closed snake contour by total count of pixels which take place inside closed snake contour.

3.2.9 Post Processing

Mitochondria could not be segmented as one piece after applying previous algorithms. Especially, utilized iterative snake algorithm for different value of w_d may cause small pieces of mitochondria to be detected. Cristae energy condensed in one region of the inside of mitochondria may cause snake boundary to be converged the inside of mitochondria instead of real boundaries. Different snake initial points are converged on different portions of mitochondria. Therefore, a combining process is necessary to segment all piece of mitochondria. Merging as a post-processing step is implemented on validated snake contours. This process is conducted when the ratio of the intersection area of two contours is larger than a threshold. This threshold is determined by taking 10% area of the smaller detected snake contour. All detected snake contours are compared with each other by controlling the criterion above. Although there is a disadvantage of combining contours which exceed the boundaries of mitochondria, it increases the accuracy of the segmentation. The validation step before joining two contours becomes very important to prevent combining wrong segmented pieces.

Figure 36 shows the input image(a) and the detected snake contours on image(b), snake contours after validation step(c) and merged contours after post processing step(d) for the selected ROI of dataset 20275.
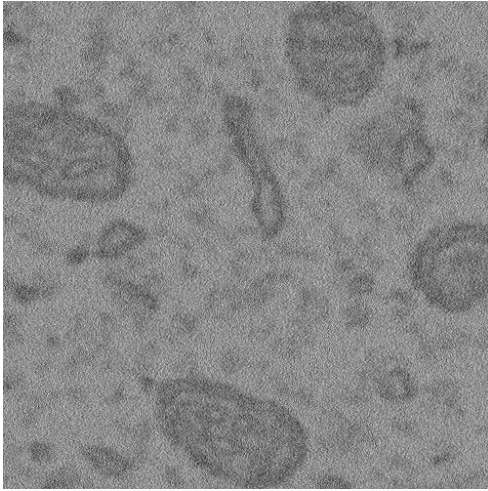
(a) Input Image
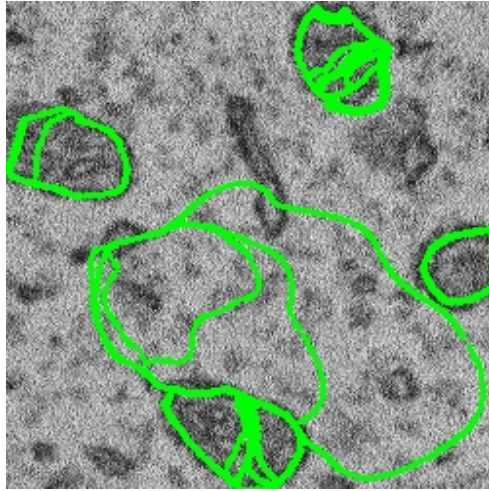
(b) Snake Contours Before Validation
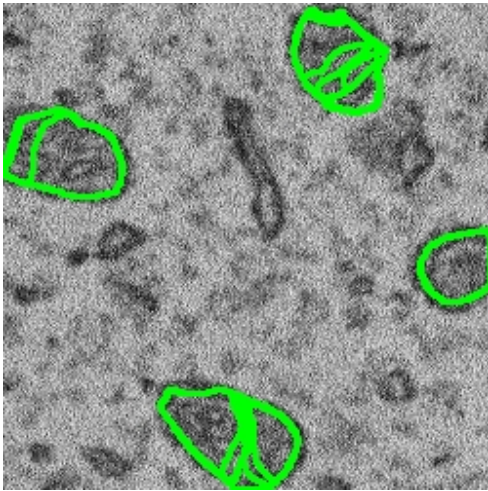
(c) Snake Contours After Validation
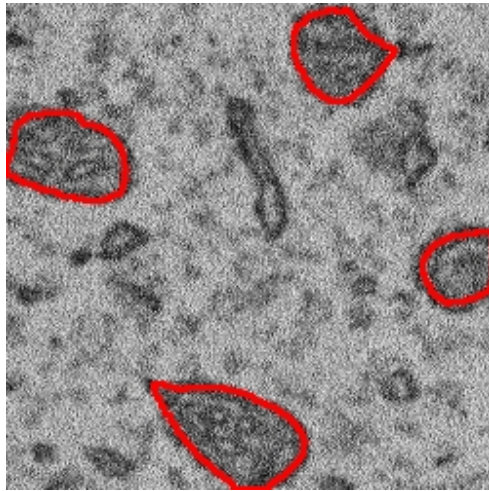
(d) Merged Snake Contours

Figure 36: Image in (a) shows input ROI image. Image in (b) detected snake contours on image before validation . Image in(c) shows snake contours on image after validation. Image in (d) shows merged contours after post processing step for the selected ROI of Dataset 20275.

CHAPTER 4

RESULTS

Results of the method implemented were obtained by using two datasets and 6 different ROIs of these two dataset. In each trial, 20 slices are used as input. Two dataset properties and x-y value of the selected ROIs of the image are expressed in Table 2. Results are obtained by using these ROI regions.

In this chapter, quantitative and qualitative results are given and discussed. Results measurement is conducted by using metrics such as DSC, precision, recall and F-score to obtain quantitative results. All parameters and reason for usage of them are explained in detail in section 4.2. Moreover, optimal values of the parameters are explained in section 4.2. Quantitative results are acquired by using different parameters. These results are discussed in section 4.3. Moreover, results are achieved by using the method in [35]. These results are obtained by changing parameters in [35] according to SEM images. These results are compared with the results of this study qualitatively.

4.1 Performance Evaluation

After implementation, performance evaluation is necessary to make inferences. Results are evaluated to measure the success of the implemented method. Evaluation is performed by using DSC, precision, recall and F-score metrics. Precision and recall are two important performance evaluation techniques. They indicate at what rate the proposed algorithm is successful. Precision value is calculated by dividing true pos-

Table 2: Properties of Dataset

ROI Name (Dataset Name)	Image Size (WidthxHeight)	Start Point Of ROI Region (XxY)	ROI Size (WidthxHeight)	Voxel Size(nm) (X x Y x Z)
ROI1(20275)	2021x3201	1350x 850	500x500	11x11x70
ROI2(20275)	2021x3201	2250x 750	500x500	11x11x70
ROI3(20275)	2021x3201	150x 700	500x500	11x11x70
ROI4(20305)	2271x1891	1300x1300	500x500	2.3x2.3x70
ROI5(20305)	2271x1891	0x650	500x500	2.3x2.3x70
ROI6(20305)	2271x1891	1000x650	500x500	2.3x2.3x70

itives by all positives. Recall value is calculated by dividing true positives to all true components. Precision and recall are calculated by using the area of the segmented shape and shape of the ground truth. In this thesis, precision and recall values are calculated by using the approach in [35]. The DSC is calculated by using the equation:

$$DSC(G, S) = \frac{2|G \cap S|}{|G| \cap |S|} \tag{31}$$

where S represents the detected shape and G represents the ground truth of the mitochondrion. The detected mitochondrion shape is compared with all ground truth shapes. Mitochondrion is matched with the ground truth which has biggest DSC. DSC is calculated by matching detected mitochondrion which has maximum DSC with the ground truth of mitochondrion. The cardinality term $\|$ represents the area of 2D shapes and the volume of 3D shapes. The precision and recall values are calculated as follows [35] :

$$\text{Precision} = \frac{|\bigcup_i G'_i \cap S_i|}{|\bigcup_i S_i|} \tag{32}$$

$$\text{Recall} = \frac{|\bigcup_i G'_i \cap S_i|}{|\bigcup_i G_i|} \tag{33}$$

"where S_i denotes the i'th detected shape and G_i denotes the ground truth of the i'th mitochondrion and G'_i denotes best matching ground truth region for S_i" [35]. Numerators of the formulas are calculated by taking union of intersections of detected shapes with best matching ground truth shape. Therefore, evaluation is performed by considering that detected shape is only matched one ground truth of mitochondrion [35]. The reliability of the performance evaluation is strengthened by calculating average of DSC. Average DSC is obtained by calculating DSC from Equation 31 for all snake contours separately and averaging them.

Moreover, F-score is calculated for all results. F-score is obtained by calculating the harmonic mean of the precision and recall value. It is explained in the Fourth Message Understanding Conference (MUC-4) [6] in 1992. This conference expresses methods for scoring to extract metrics and improves methods used in MUC-3. The F-score gives a single result by considering recall and precision. It combines them to a certain extent. Precision and recall have their weight to calculate F-score. This weight can be set according to conducted study. The formula of the F-score is given as:

$$F = \frac{(\beta^2 + 1.0) * P * R}{\beta^2 * P + R}, 0 \leqslant \beta \leqslant +\infty \tag{34}$$

where P is equal to the value of Precision, R is equal to the value of the Recall and β is the relative weight of recall over precision. If β is selected as 1, it means that precision and recall are equally important on the F-score. if β is selected as 0.5, it means that recall has half importance on the precision for the F-score. If β is selected as 2, it means that recall has twice importance on the precision for the F-score. β shows how the recall value has importance on the precision value. If $\beta > 1$, F becomes recall weighted. If $\beta < 1$, F becomes precision weighted. If $\beta = 1$, F becomes equally
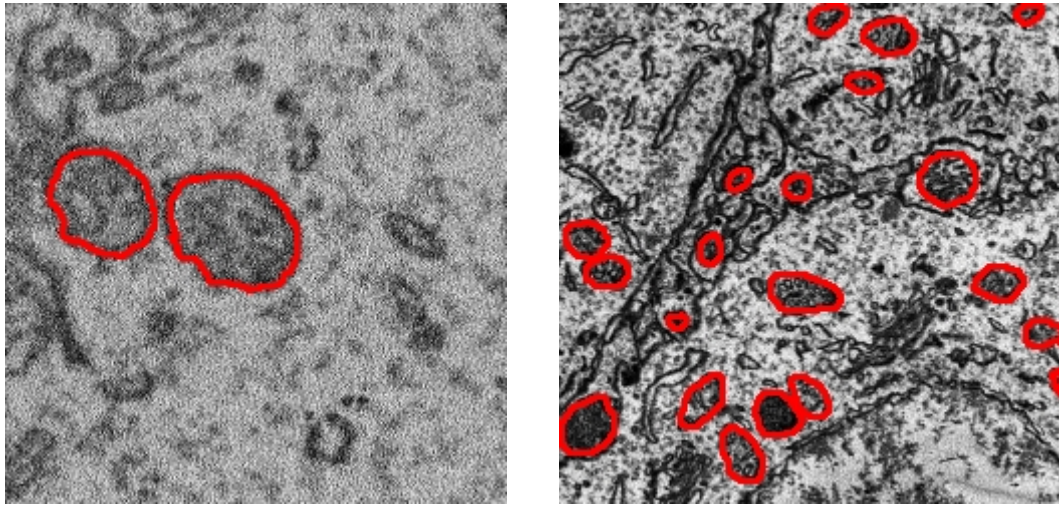
Figure 37: Ground Truths of First Dataset(on the left) and Second Dataset(on the right)

weighted [6]. In this study, F-score is calculated by considering that precision and recall are equally important. It is selected as β is equal to 1.

Consequently; DSC, Precision, Recall and F-score are used for performance evaluation quantitatively as specified in this section.

4.2 Parameter Analysis

As can be seen from the flowchart in Figure 15 in Chapter 3, there are many algorithms. Algorithms used in the method of this study include many parameters. These parameters determine segmentation results. All of them has specific effect for the precision, recall, F-score and DSC. For different parameters, results are obtained, and these results are discussed in section 4.3. The parameters sets used in algorithms to obtain best results for dataset 20275 are specified in Table 3 and Table 9.

Datasets 20275 and 20305 are tested with parameters set in Table 3, and results are obtained. Results for the second dataset are not satisfying because characteristic of second dataset is different. Voxel sizes of the datasets are different for x-y dimension, sizes of mitochondria for same pixel region are very different. Figure 37 shows the ground truth samples for two datasets. This figure shows that the sizes of mitochondria for two datasets are very different. Moreover, while there exists 2 mitochondria in first dataset, there are twenty mitochondria in second dataset as can be seen from Figure 37. Parameters in the algorithms of this study were determined by considering the first dataset. Parameters for the second dataset should be determined differently. Therefore, a new approach is necessary for segmentation of mitochondria to achieve good results for different datasets. If there was more time, automatic parameter selection is made by considering voxel size and histogram of the image. Voxel size can

be used to determine especially in resampling ratio, bilateral filter and snake based shape extraction parameters. Voxel size of the dataset changes membrane thicknesses. Thicknesses of membranes are important to decide parameters such as Gaussian and bilateral parameters. Changes in voxel size also cause changes in size of mitochondria. Therefore, voxel size is important for the snake initialization parameters. It affects radius of the curves, minimum number of points and epsilon value of the snake initialization. Size of mitochondria and membrane thicknesses also affect energy inside and the outside of mitochondria. Therefore, parameters of the curve fitting and snake based shape extraction are also affected by voxel size. Moreover, thresholding parameters for the initial point elimination and validation are very important to obtain optimal values of precision and recall. Effect of thresholding parameters on precision, recall, F-score and DSC are discussed in Quantitative Results subsection 4.3.1. These thresholding parameters are determined by considering intensity values of pixels inside mitochondria. In Histogram Equalization subsection 3.2.2 of Chapter 3, it is mentioned how these thresholding parameters are set. For different datasets, frequencies of the intensity values may be different. Therefore, these thresholding parameters can be determined by using the histogram analysis of the image. In this study, all parameters of the method are determined by considering the dataset 20275.

Parameters of all algorithm steps are discussed as below:

Auto Contrast Enhancement: Histogram Equalization is implemented in this step. Histogram Equalization does not include any parameter.

Resampling: Resampling number is the parameter of this step. When it is used for downsampling, it reduces computation time of the algorithm and provides more robust results. Resampling number is selected as 0.5 for this study.

Bilateral Filtering: This algorithm enables to reduce noise and preserve edges. It reduces the effect of ridges which do not belong to membranes. There are two parameters for this step. Sigma intensity and sigma spatial determine the effect of the bilateral filtering. When the sigma intensity is between 30 and 100, and sigma spatial is between 1 and 5, effective results are achieved. Sigma intensity and sigma spatial parameters of bilateral filter, and Gaussian sigma of ridge detection are very important to reach better results. These three parameters should be considered together. In this study, results are obtained for two options of these parameters. Especially, when sigma intensity is equal to 50, sigma spatial is equal to 1.5 and Gaussian sigma of ridge detection step is equal to 3, good results are obtained quantitatively. Moreover, when sigma intensity is equal to 80, sigma spatial is equal to 5 and Gaussian sigma of ridge detection step is equal to 3, results are also well quantitatively. Quantitative results are given in section 4.3.1 for these two options.

Implementation of bilateral filter is conducted with opencv and without using opencv. Implementation times of bilateral filter with opencv and without opencv for ROI1 region are given in Table 5. Results are compared to each other, and it is checked that all values in bilateral images are same for these two methods.

Table 3: First Parameters Set Used In This Study

List of Parameters and Settings		
Step Name	Parameter Name	Parameter Value
Preprocessing	Resampling Ratio	0.5
	Bilateral Filtering Sigma Spatial	1.5
	Bilateral Filtering Sigma Intensity	50
	Bilateral Filtering Window Size	15
Ridge Detection	Gaussian Sigma Spatial	3
	Gaussian Window Size	15
Energy Mapping	Window Size	15
	Quantization Number of Angle	4
Curve Fitting	Threshold Energy	40% of max $e_\theta(s)$
	Curve Update Paramaters(τ_x, τ_y, τ_z)	1
Curve Filtering	Average Score Threshold	8
	Average Length Threshold	40
	Score Threshold	800
	Average Intensity Threshold	90
	Max Allowed Value For Curvature	1
Snake Initialization	Minimum Number of Points	15
	Epsilon of DBSCAN	25
	Radius of The Curve	10
	Initial Point Elimination Threshold	120
Snake-Based Shape Extraction	Initial Radius Size of Snake	10
	Tension in XY Plane	10
	Curvature in XY Plane	50
	Tension in Z Plane	5
	Curvature in Z Plane	5
	External Energy Weight	1
	Wd_{Min}	1
	Wd_{Max}	3
	Wd_{Step}	1
	Z Thickness	5
	Convergence Value for Area	5
	Convergence Count For Area	100
Validation	Average Intensity of The Snake Contour	110
	Inner Average Intensity of The Snake Contour	110
Post Processing	Merging Threshold Ratio	0.1

Ridge Detection: There is a sigma parameter for the Gaussian derivatives to detect ridge structures. This value also is effective when it is considered together with bilateral filter parameters. When bilateral parameters are selected in the specified interval as stated above, the sigma parameter for the ridge detection is effective especially on the interval 3 and 5. As expressed, this interval is effective, when it is considered with parameters of bilateral filter.

Energy Mapping: There are two parameters to be determined in this step. The first parameter is the quantization number. Since an image consists of pixels, a continuous calculation is impossible and so there should be discrete calculation.In this study, 4 and 8 are tried as quantization number. Increasing the quantization number can also increase the performance up to a certain level. However, this situation can cause to spend too much time. Moreover, results obtained by quantization numbers 4 and 8 are not very different. When the quantization number is equal to 4, desired results are obtained. The second parameter of this step is window size to obtain energy. After many trials with 10,11,12,13,14,15,16,17,18, best results are obtained when window size is equal to 12.

Curve Fitting: In this step, the percentage of the ridge energy is used to determine the local maxima point as a start point to start the iterative curve fitting algorithm. This percentage gives desired results when it is selected as 40%. This value is taken from [35]. When this value is tried, desired results are achieved. This value provides good curve fitting and preventing bad initialization for the iterative curve fitting algorithm. Moreover, there are update parameters which determine the possible initialization points. If these parameters are selected as high like 2 and 4, results are not very different, and not better than 1. Furthermore, calculation time increases for values 2 and 4. However, there is not much difference between high and low values in terms of accuracy. Therefore, these parameters are selected as 1 in this step.

Curve Filtering: This step includes length threshold, energy score of the curve threshold, average energy score of the curve threshold, average intensity value of the curve threshold, and curvature ratio threshold. For these parameters, many trials are conducted to determine the optimum value. For the length threshold value, 40 is selected. For the energy score of the curve threshold value, 800 is selected. For the average energy score of the curve threshold value, 8 is selected. For the average intensity value of the curve threshold, 90 value is selected. For the curvature value, 1 value is selected. For these values the desired result is obtained. This curve elimination is necessary to determine initial points for the snake-based shape extraction and enable segmentation of the mitochondria membranes more accurately by eliminating unreliable curves and keeping reliable, and necessary curves.

Snake Initialization: In this step, the DBSCAN algorithm[10] is implemented to determine initial points. There are four parameters which affect the initial point determination. These parameters are epsilon, the minimum number of points, z thickness, and initial radius which is the distance between the curve and the location of initial point. Snake initialization is unreliable when initial points are determined at the outside of mitochondria. After some trials, epsilon is set to 25, the minimum number of points is set to 15, and the radius is set to 10 to obtain the desired result. If z thick-

ness is greater than 5, initial points are determined wrongly because the place of the mitochondrion in successive slices changes much. 5 is the optimum value for initial point determination. For the different values of z thickness, DSC average, precision, recall and F-score are calculated in Quantitative Results subsection of section 4.3.

Snake-Based Shape Extraction: There are 6 parameters used in snake-based shape extraction. These parameters are X-Y tension, X-Y curvature, Z tension, Z curvature, inflation, and external force parameters. The proportion of these parameters is important to obtain desired results. The algorithm is implemented by using different values of inflation parameters. The inflation parameter is determined as a certain interval. Many trials are conducted and results are obtained at the end of these trials. Finally, optimum results are obtained when X-Y Tension is equal to 10, X-Y Curvature is equal to 50, Z Tension is equal to 5, Z Curvature is equal to 5, inflation is between 1 and 3, and external force is equal to 1.

Validation Process:
In this step, two features are used to validate segmented contours. These features are the average intensity of the snake contour and the inner average intensity of the snake contour. Validation is implemented by using a threshold for these features. For the average intensity of the snake contour, 110 is optimal value determined as thresholding. Snake contours with average intensity higher than this value are eliminated. For the inner average intensity of the snake contour, 110 is also optimal value determined as thresholding. Snake contours with inner average intensity higher than this value are eliminated. For the different values of these thresholds; DSC average, precision and recall are calculated for dataset 20275 in Quantitative Results subsection of section 4.3. However, these values can be changed for a different dataset. A new approach should be proposed to determine these values for different datasets. .

Post Processing: In this step, merging ratio parameter should be determined. In previous steps, there are many eliminations for snake contours such as initial point elimination, and snake contour elimination in the validation step. Therefore, a low ratio for merging is preferred to increase the calculated precision and recall value. Each initial point is converged on a certain place of mitochondria. Therefore, merging them enables better segmentation. A high merging ratio prevents merging these detected contours. As a result, a low merging ratio is preferred. This value is determined as 10% of intersection area.

4.3 Quantitative and Qualitative Results

4.3.1 Quantitative Results

The precision, recall, F-score and DSC metrics have been calculated for many different parameters stated in this section. Moreover, F-score is calculated to state the strength of algorithm results.

Table 4: Properties of Computer and Software Tool

Memory	15.3 GiB
Processor	Intel® Core™ i7-10750H CPU @ 2.60GHz × 12
Graphics	Mesa Intel® UHD Graphics (CML GT2) / Mesa Intel® UHD Graphics (CML GT2)
OS Name	Ubuntu 20.04.2 LTS
OS Type	64-bit
GNOME Version	3.36.8
Windowing System	X11
Python Version	3.8

Properties of used computer and software tool are given in Table 4. Python 3.8 is used with PyCharm IDE to develop software. The multithreading library is preferred to make multiprocess calculations up to the snake method in each slice. Multithreading reduces calculation time. Table 5 shows the duration of algorithms of ROI1 for the parameters set stated in Table 3.

After many trials, best results are achieved by setting parameters as in Table 3 and Table 9. The results of parameters set in Table 3 are given in Table 6 for two datasets and 6 ROIs. The results of second dataset are not very satisfying because of the reason stated in section 4.2.

Adjustment of the z-thickness of the snake algorithm is important to obtain desired results. Since mitochondria in each slice of SEM images are changed in a huge distance as compared to TEM images. When z thickness is selected as high, initial points can not be formed as desired. Therefore, z thickness is selected as a lower value as compared to trials in [35]. When z thickness increased, values of precision and DSC results are decreased since more initial points are initiated and non-mitochondrial regions are detected as mitochondria. Moreover, results are not satisfying with increasing z thickness, because distance in z axis is high in SEM images. Voxel size of used dataset 20275 is equal to 11 nm x 11 nm x 70 nm. Mitochondria and internal structures of the cell change a lot in x-y axis between two successive slices. Therefore, big z thickness gives worse results since wrong initial points are determined. Although these initial points are eliminated due to thresholds, results do not become well as compared to low z thickness value. Figure 38 shows the initial points when z thickness is equal to 5, 10, 20. Since more initial points are determined for thickness 20, recall value is greater than for thickness 10. Table 7 shows the results for the different z thickness values.

The another important parameter to obtain desired result is threshold value of validation step. Optimal threshold value of validation is 110. When the threshold value is set to value different than 110, results of DSC are decreased because best value for average intensity of mitochondria region intensity is around 110. When threshold value is above 110, segmented candidate non-mitochondrial region could not be eliminated. Therefore, precision value is decreased. Precision value is calculated as

Table 5: Run Time Of Algorithms For Parameter Set in Table 3

DATABASE BASENAME: 20275			
STEP NAME	SCALE	DURATION(sec)	ROI Number
Auto Contrast	For First Slice	0.144	ROI1
Resampling	For First Slice	0.001	ROI1
Bilateral Filter (OpenCv)	For First Slice	0.011	ROI1
Bilateral Filter (New Formed)	For First Slice	67.549	ROI1
Histogram Equalization	For First Slice	0.001	ROI1
Ridge Detection	For First Slice	0.672	ROI1
Energy Mapping	For First Slice	6.071	ROI1
Curve Fitting	For First Slice	281.877	ROI1
All Steps Before Snake Algorithm	For 20 Slices	4154.738	ROI1
Snake Algorithm	For 20 Slices	26311.196	ROI1
Total Time	For 20 Slices	30474.813	ROI1

Table 6: Results For The Parameters Set in Table 3

EVALUATION RESULTS FOR ALL DATASETS				
	DSC AVERAGE	PRECISION	RECALL	F-SCORE
ROI1	0.84	0.92	0.78	0.85
ROI2	0.51	0.67	0.75	0.71
ROI3	0.47	0.67	0.55	0.60
Mean ± Std	0.61 ± 0.20	0.76 ± 0.14	0.69 ± 0.13	0.72 ± 0.02
ROI4	0.09	0.04	0.31	0.07
ROI5	0.19	0.06	0.33	0.10
ROI6	0.18	0.07	0.29	0.11
Mean ± Std	0.15 ± 0.05	0.06 ± 0.02	0.31 ± 0.02	0.09 ±0.02
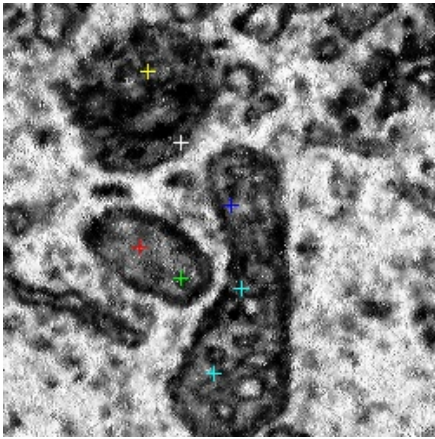
(a) Determined Initial Points For Z Thickness = 5
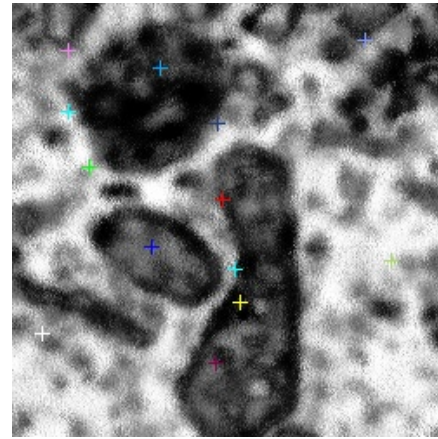
(b) Determined Initial Points For Z Thickness = 10
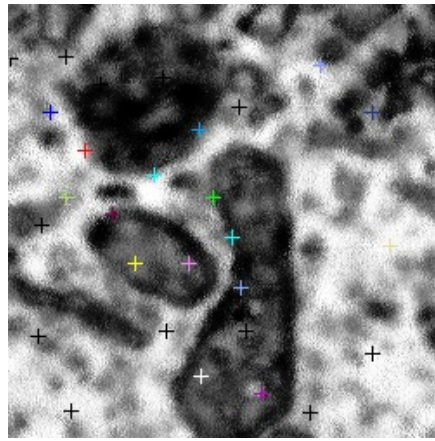
(c) Determined Initial Points For Z Thickness = 20

Figure 38: Determined Initial Points After Elimination For Z Thickness 5(a),10(b),20(c)

in Equation 32. When the non-mitochondrial regions are segmented as mitochondria, areas of all positives are increase, and precision is decreased. When threshold value is higher than 110, recall value is increased up to certain value. After this value, recall becomes constant because mitochondrial region could not be eliminated after certain value. Results of different threshold values for dataset 20275 are given in Table 8. Graph in Figure 39 is formed by using data in Table 8. As can be seen from Figure 39, recall value is increased to certain value with increasing threshold value and finally becomes constant. Precision is decreased to certain value with threshold value. Best results are achieved with around value 110 because this elimination is conducted by using bilateral filter and histogram of bilateral filter is given in Figure 25. Best results are obtained with threshold value of 110, and 120.

Table 7: Evaluation Metrics Results Of Different Z Thickness Values For Parameter Set in Table 9

DATABASE NAME:20275				
EVALUATION METRICS				
	DSC AVERAGE	PRECISION	RECALL	F-SCORE
ROI Number	Z Thickness = 5			
ROI1	0.83	0.91	0.71	0.79
ROI2	0.47	0.73	0.76	0.74
ROI3	0.41	0.70	0.55	0.62
Mean ± Std	0.57 ± 0.23	0.78 ± 0.11	0.67 ± 0.11	0.72 ± 0.09
	Z Thickness = 10			
ROI1	0.67	0.88	0.65	0.75
ROI2	0.22	0.62	0.67	0.64
ROI3	0.19	0.65	0.40	0.50
Mean ± Std	0.36 ± 0.27	0.72 ± 0.14	0.57 ± 0.15	0.63 ± 0.13
	Z Thickness = 20			
ROI1	0.56	0.78	0.70	0.74
ROI2	0.19	0.59	0.79	0.68
ROI3	0.19	0.69	0.50	0.58
Mean ± Std	0.31 ± 0.22	0.69 ± 0.09	0.66 ± 0.15	0.67 ± 0.08
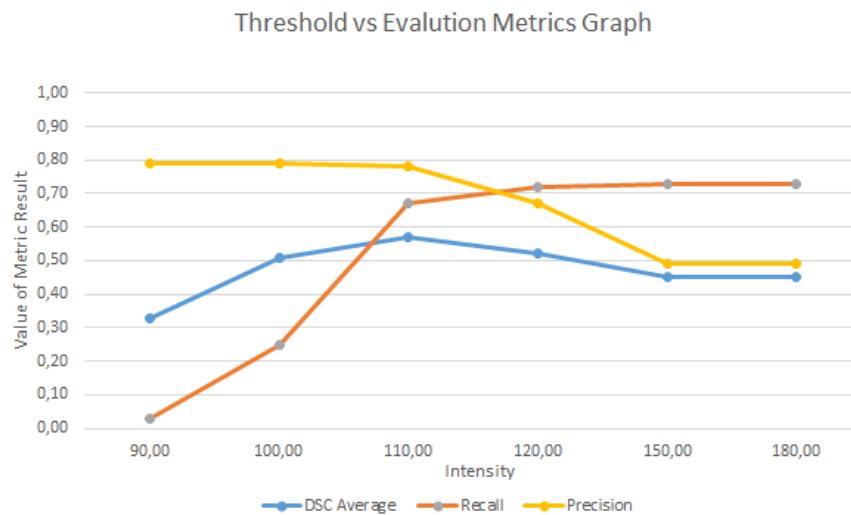
Figure 39: Threshold vs Evaluation Metrics Graph

Table 8: Evaluation Metrics Of Different Threshold Values In Validation For The Parameters Set in Table 9

	DSC AVERAGE	PRECISION	RECALL	F-SCORE
DATABASE NAME:20275				
EVALUATION METRICS				
ROI Number	Threshold = 90			
ROI1	0.45	0.98	0.05	0.10
ROI2	0.23	0.66	0.01	0.01
ROI3	0.33	0.73	0.04	0.07
Mean $\pm$ Std	0.33 ± 0.11	0.79 ± 0.17	0.03 ± 0.02	0.06 ± 0.04
	Threshold = 100			
ROI1	0.82	0.94	0.47	0.63
ROI2	0.35	0.64	0.10	0.18
ROI3	0.36	0.78	0.16	0.26
Mean $\pm$ Std	0.51 ± 0.27	0.79 ± 0.15	0.25 ± 0.20	0.36 ± 0.20
	Threshold = 110			
ROI1	0.83	0.91	0.71	0.79
ROI2	0.47	0.73	0.76	0.74
ROI3	0.41	0.70	0.55	0.62
Mean $\pm$ Std	0.57 ± 0.23	0.78 ± 0.11	0.67 ± 0.11	0.72 ± 0.09
	Threshold = 120			
ROI1	0.74	0.78	0.72	0.75
ROI2	0.43	0.62	0.76	0.68
ROI3	0.40	0.62	0.66	0.64
Mean $\pm$ Std	0.52 ± 0.19	0.67 ± 0.09	0.72 ± 0.05	0.69 ± 0.06
	Threshold = 150			
ROI1	0.61	0.43	0.75	0.55
ROI2	0.39	0.55	0.77	0.64
ROI3	0.34	0.50	0.68	0.57
Mean $\pm$ Std	0.45 ± 0.14	0.49 ± 0.06	0.73 ± 0.05	0.59 ± 0.05
	Threshold = 180			
ROI1	0.61	0.43	0.75	0.55
ROI2	0.39	0.55	0.77	0.64
ROI3	0.34	0.50	0.68	0.57
Mean $\pm$ Std	0.45 ± 0.14	0.49 ± 0.06	0.73 ± 0.05	0.59 ± 0.05

Table 9: The Second Parameters Set Used in This Study

List of Parameters and Settings		
Step Name	Parameter Name	Parameter Value
Preprocessing	Resampling Ratio	0.5
	Bilateral Filtering Sigma Spatial	5
	Bilateral Filtering Sigma Intensity	80
	Bilateral Filtering Window Size	15
Ridge Detection	Gaussian Sigma Spatial	3
	Gaussian Window Size	15
Energy Mapping	Window Size	15
	Quantization Number of Angle	4
Curve Fitting	Threshold Energy	40% of max $e_\theta(s)$
	Curve Update Paramaters(τ_x, τ_y, τ_z)	1
Curve Filtering	Average Score Threshold	8
	Average Length Threshold	40
	Score Threshold	800
	Average Intensity Threshold	90
	Max Allowed Value For Curvature	1
Snake Initialization	Minimum Number of Points	15
	Epsilon of DBSCAN	25
	Radius of The Curve	10
	Initial Point Elimination Threshold	120
Snake Based Shape Extraction	Initial Radius Size of Snake	10
	Tension in XY Plane	10
	Curvature in XY Plane	50
	Tension in Z Plane	5
	Curvature in Z Plane	5
	External Energy Weight	1
	Wd_{Min}	1
	Wd_{Max}	3
	Wd_{Step}	1
	Z Thickness	5
	Convergence Value for Area	5
	Convergence Count For Area	100
Validation	Average Intensity of The Snake Contour	110
	Inner Average Intensity of The Snake Contour	110
Post Processing	Merging Threshold Ratio	0.1

4.3.2 Qualitative Results

Main algorithms of this study are taken from [35]. In the study of [35], results are obtained for TEM images. Parameters are set, and the method of [35] is proposed according to characteristics of TEM image. In this study, parameters are set by considering characteristics of SEM images, and extra features are included to obtain better results. Figure 40 shows the initial points obtained for the proposed method of [35] for ROI1 specified in Table 2 of dataset 20275. The best obtained results for the proposed method of [35] after post processing are also given in Figure 40. Parameter sets for these results are given in the Table 10. As can be seen from the results in Figure 40 and Figure 41, changes in this study make huge contribution to obtain better results when results are compared to ground truth results which are given in Figure 42. Main changes are initial point elimination, elimination with reference to internal intensity of image and intensity of contour, merging ratio, and selection of optimal parameters. These changes provide better results.
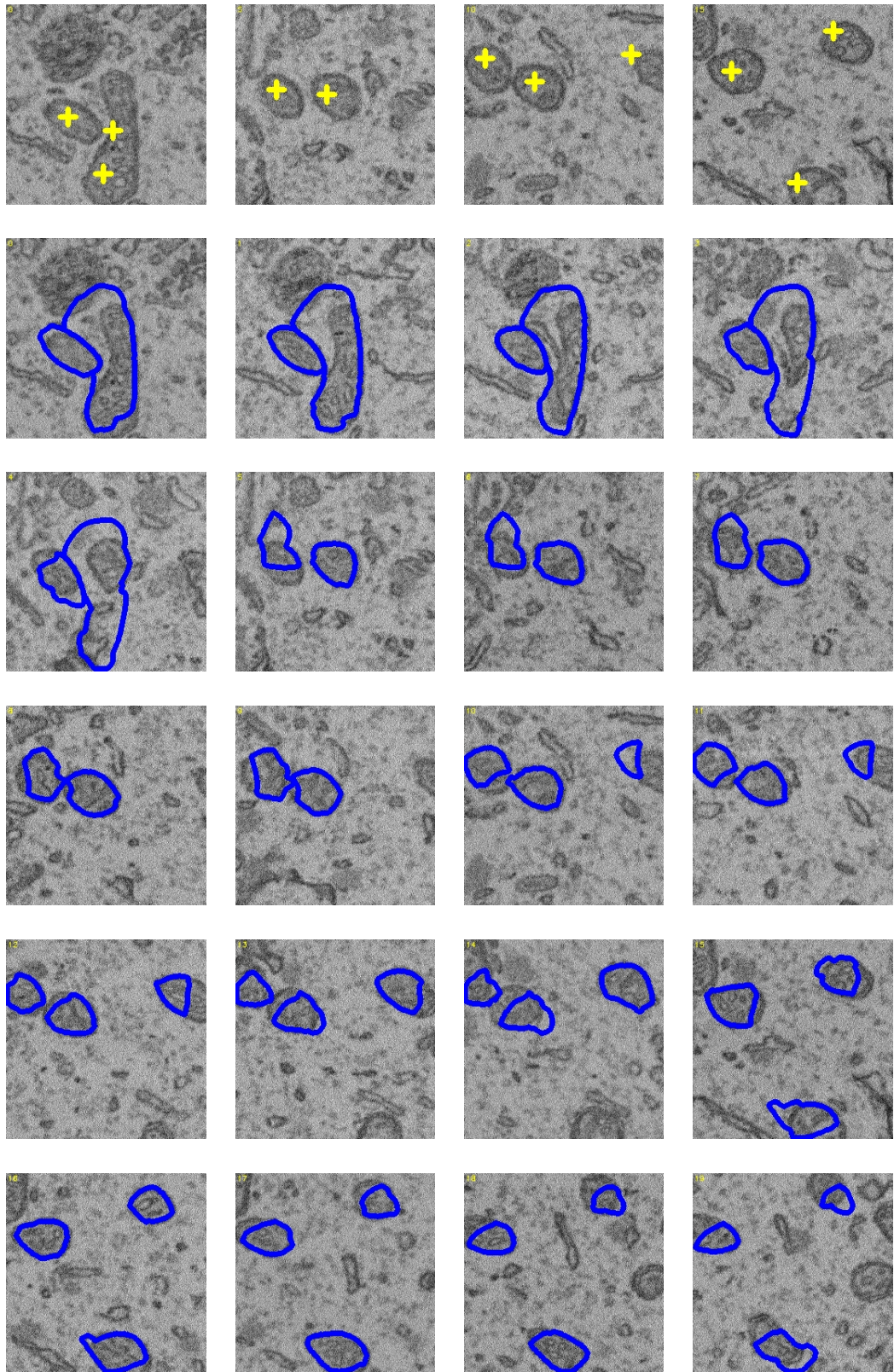
Figure 40: ROI1 Results Of Proposed Method by [35] with parameter sets given in Table 10 for 20 successive slices. First 4 images above show the initial points for every 5 slices.(Z Thickness is equal to 5.)
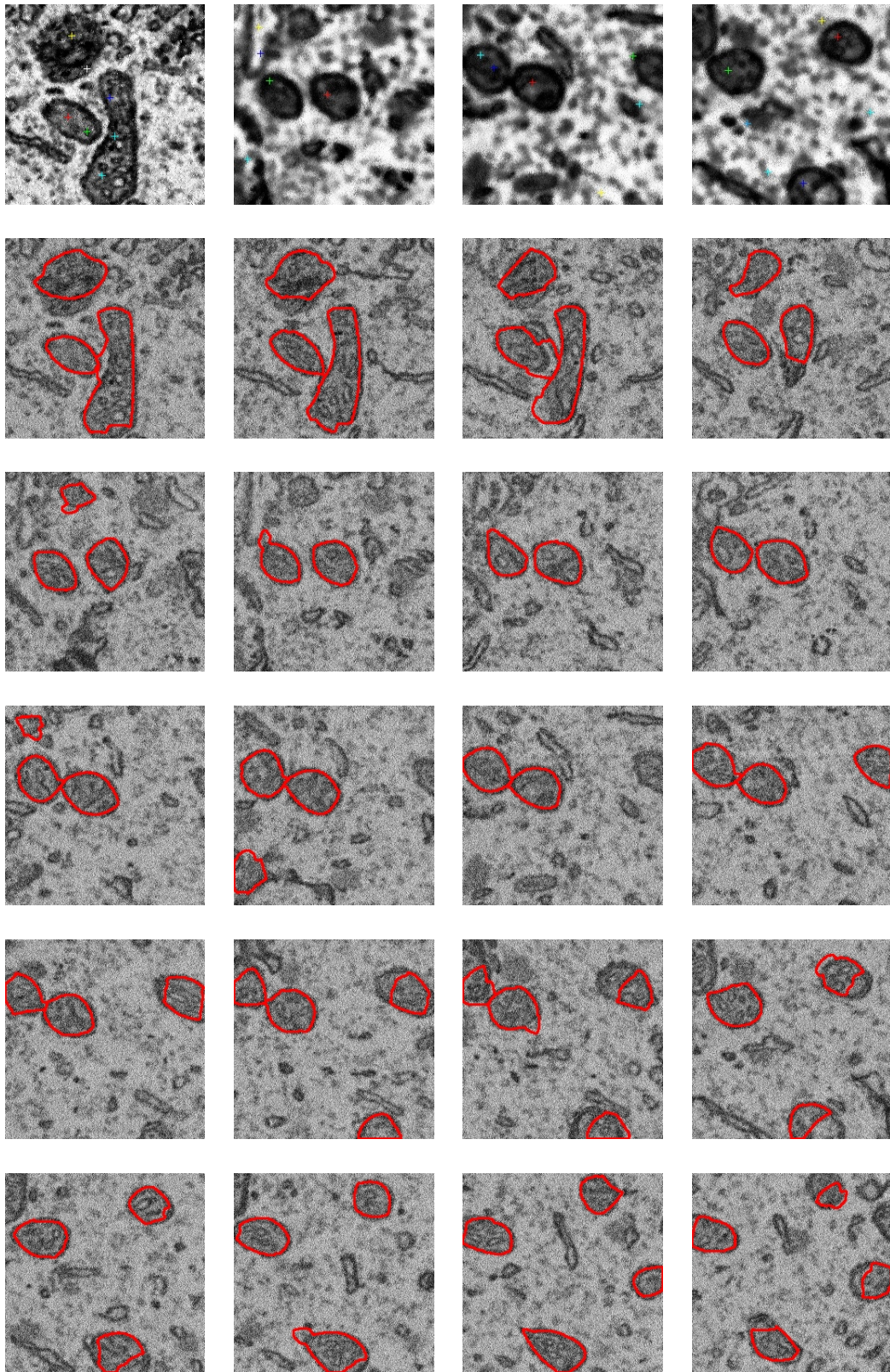
Figure 41: ROI1 Results Of this study with parameter sets given in Table 3 for 20 successive slices. First 4 images above show the initial points for every 5 slices.(Z Thickness is equal to 5.)

Table 10: Parameter Sets Of The Study [35] For Best Result

List of Parameters and Settings		
Step Name	Parameter Name	Parameter Value
Preprocessing	Auto-Contrast Histogram Cut	0.005
	Resampling Ratio	0.5
	Bilateral Filtering Sigma Intensity	50
	Bilateral Filtering Sigma Spatial	0.15
Ridge Detection	Gaussian Sigma Spatial	3
Energy Mapping	Low Frequency Window Size	12
	High Frequency Window Size	6
Curve Fitting	Threshold Energy	40% of $e_\theta(s)$
	Curve Update Paramaters(τ_x, τ_y, τ_z)	2
Curve Filtering	Curvature	4
	Min Arc Length Threshold	40
	Min Average Energy Threshold	8
	Min Average Energy Threshold	800
	Max Allowed Value For Curvature	1
Snake Initialization	Minimum Number of Points	15
	Epsilon of DBSCAN	25
	Radius of The Curve	10
Snake Based Shape Extraction	Initial Radius of Snake Size	10
	Tension in XY Plane	10
	Curvature in XY Plane	50
	Tension in Z Plane	5
	Curvature in Z Plane	5
	External Energy Weight	1
	Wd_{Min}	1
	Wd_{Max}	3
	Wd_{Step}	1
	Z Thickness	5
Validation	Validity Threshold	All validation parameters are discarded by setting validity threshold to 0
Post Processing	Merging Threshold	0.3

Figure 42: Ground Truths For 20 Slices Of ROI1 Region

CHAPTER 5

CONCLUSIONS AND FUTURE WORK

5.1 Conclusions and Discussions

In summary, automatic segmentation of mitochondria in SEM images is implemented in this thesis. The method consists of many steps. First step of the method is the pre-processing that consists of auto contrast enhancement, re-sampling and bilateral filtering; Moreover, ridge detection, energy mapping, curve fitting and filtering are a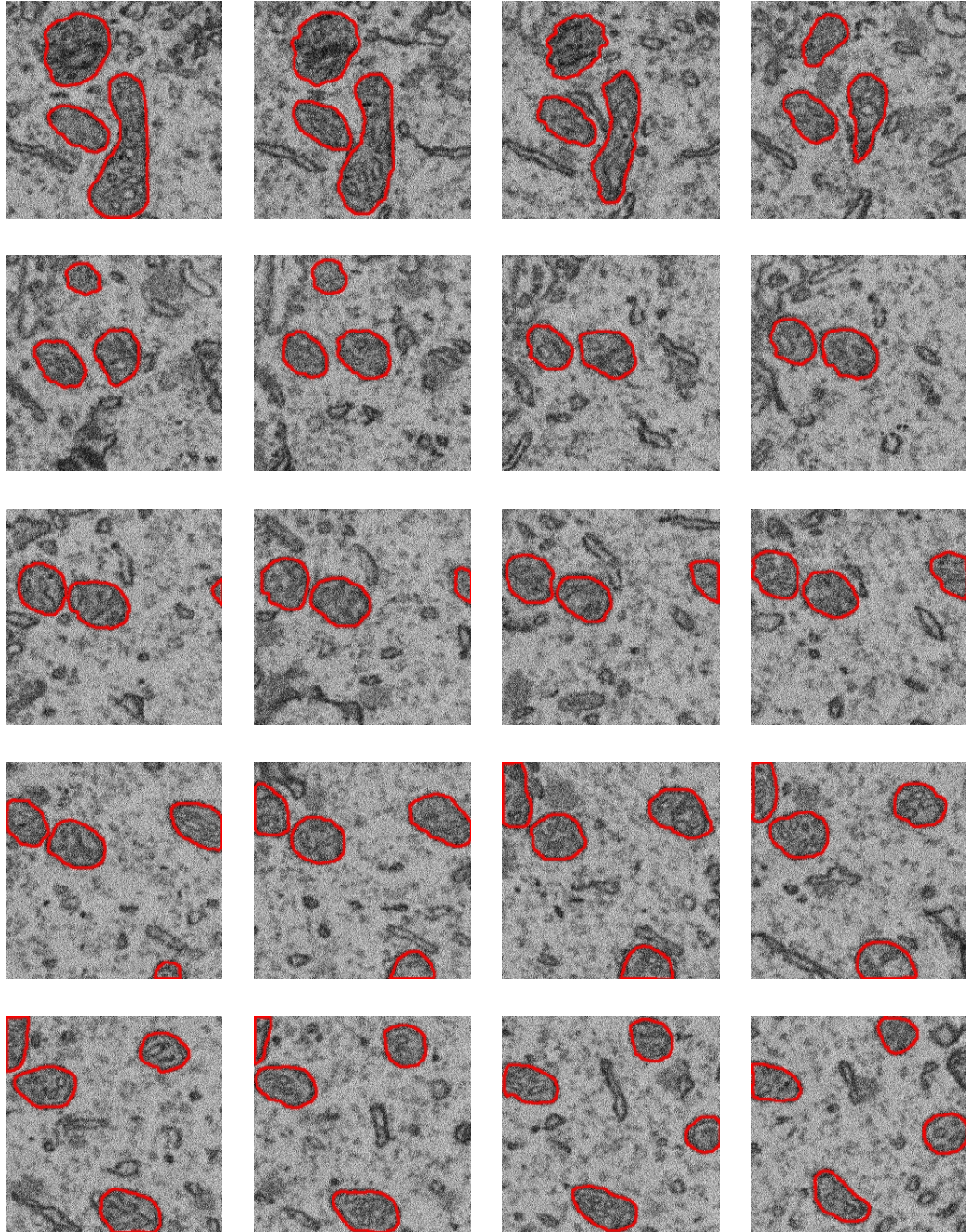pplied to extract curves. After that snake initialization, histogram equalization, initial point elimination are conducted to determine initial points. After initial point determination, snake-based shape extraction are implemented to obtain snake contours. Finally, false snake contours are eliminated by using validation, and post processing is used to merge contours which are not eliminated. Obtained results are evaluated by using the DSC, precision, recall and F-score metrics.

Algorithms are accelerated by using multithreading. The multithreading library is preferred to make multiprocessing calculations up to the snake based shape extraction step for each slice. Multithreading library reduced calculation time.

In this study, SBFSEM images are used for segmentation. It has lower resolution than TEM, FIB-SEM images. However, acquisition time of the SBFSEM is lower than other imaging techniques. Moreover, acquisition area of the SBFSEM is greater than other techniques. Devices used in SBFSEM is simpler and smaller than the TEM imaging techniques. Because of the reasons stated, SBFSEM is commercially preferred. Moreover, there is limited number of study in SBFSEM images. Because of these reasons, this study is valuable in the field of automatic segmentation of mitochondria.

Most of studies mentioned in the literature review chapter which uses SEM images evaluate results with simple evaluation metrics. Segmentation is accepted as true if intersection area of mitochondrion and ground truth is greater than %70. In this study, DSC, precision, recall and F-score are calculated as in the study of [35]. Results directly show the intersection area of detected shapes. If other simple evaluation metric was used and algorithms were determined according to this simple metric; higher precision, recall, DSC and F-score would be obtained.

For this study, some parameters such as snake, bilateral parameters and Gaussian filter parameter of ridge detection have a very crucial effect to obtain desired results. Moreover, adjustment of z thickness of the snake algorithm has significant effect for desired results because SEM images change in z direction too much as compared to TEM images. Big z thickness values cause worse initial points as compared to small z thickness.

Automatic segmentation of mitochondria is very difficult task due to nature of image acquisition. Quality of images is not very good for segmentation. Images include noise, and all structures are in images similar. Therefore, feature extraction becomes difficult. It is very difficult task to segment mitochondria even with eye. Manual segmentation is conducted by very experienced specialists. Many biologists can make mistake while making hand segmentation. As a result, automatic segmentation of mitochondria is a very difficult task, and this study is important to make segmentation of mitochondria in SEM images.

In this study, two datasets were used to obtain results. Parameters of the algorithms are determined by considering only one of them. Membrane thicknesses, size and number of mitochondria for the same size changes in different datasets. Therefore, while good results are obtained one dataset, worse results are obtained for other dataset. Mean of precision, recall, F-score and DSC values are equal to 0.76, 0.69, 0.61, 0.72 respectively for the first dataset. Mean of precision, recall, F-score and DSC values are equal to 0.06, 0.31, 0.09, 0.15 respectively for the second dataset. Therefore, a new approach should be proposed to determine optimal parameters values for different datasets as future work. Threshold parameters can be set by using histogram of the local image in the future. Threshold parameters are used to eliminate false initial points and false snake contours. Intensities inside of mitochondria and Intensities outside of mitochondria are very different. Inner intensity of mitochondria lower than intensity of the outside of mitochondria. Threshold parameters can be determined by using this feature. Histogram of the images gives idea about this thresholding value. As future work this information can be used. Moreover, parameters can be set according to voxel size for different datasets in the future. In the study of [35], some parameters such as bilateral, resampling and ridge detection sigma parameters were set by using pixel size of the image. However, size of z direction was not considered to determine parameters since TEM image has isotropic resolution for all dimension. If there was more time, algorithm parameters such as bilateral, resampling and ridge detection sigma can be set by using x-y size of datasets. In addition, voxel size of z dimension can be considered to determine snake parameters. Since the proportions of snake parameters are important for convergence of snake contours on the mitochondria membranes, voxel size in z direction can be used to set Z tension and Z curvature values according to XY tension and XY curvature values. This enables the method to be effective in different datasets. Since Z direction size/X-Y direction size ratio of SEM images is much greater than ratio in TEM images, voxel size in z direction should be taken into account to determine snake parameters for Sem images.

5.2   Future Work

Run times of the implemented algorithms are high but they can be reduced by applying parallel processing and optimization techniques. Moreover, algorithms can be accelerated by using optimization techniques. There are many loops in used algorithms. Computation times can be decreased by optimizing calculations in loops. Moreover, algorithms can be made parallel using GPU and Cuda. In this study, numba library of Python is used for parallelization but effective parallelization could not be succeeded. "Numba is an open source JIT compiler that translates a subset of Python and NumPy code into fast machine code." [1]. After initial point determination, initial points are used for snake method. Snake method can be implemented sequentially with these initial points. In the future, these initial points of candidate snake contours can be implemented as parallel because initial points do not affect each other.

The parameters in this study can be determined for different datasets by using the approach proposed in the discussion section. This study shows that if the parameters of this study is determined by using features of the image such as histogram and voxel size, better results can be obtained for different datasets. These algorithms can be applied for FIB-SEM, ATUM-SEM and results of tests can be compared to each other.

Finally, deep learning methods can be considered as segmentation method of mitochondria and cristae. There are a lot of parameters and features to be determined. Deep Learning methods such as CNN can be applied to make feature extraction. If data is increased and more powerful computers are supplied to make training, and testing, good results can be obtained. Recently, there are some studies about deep learning. In the study of [25], improved Mask R-CNN is applied on the SEM images and satisfying results are obtained for different datasets. Moreover, in the study of [8] and [41], CNN method is used for SEM image segmentation. In study of [19], ANN is used for segmentation on TEM images. The algorithms of [19] can be used for SEM images for future work. In these studies, modified U-net, modified resnet50, ANN and VGG-16 architectures of deep learning are used. Different architectures such as Alex-Net and Google-Net can be tried for different types of SEM images. All results can be compared with each other. In the future, algorithms of these studies can be implemented and improved. Precision, recall, F-score and DSC values can be increased by using these algorithms.

Bibliography

[1] *A 5 minute guide to Numba*. `http://numba.pydata.org/`. last visited on September 2021.

[2] Jörgen Ahlberg. "Active Contours in Three Dimensions". LiTH-ISY-Ex No. 1708. Sweden: Linköping University, 1996.

[3] St Baloyannis. "Mitochondria and Alzheimer's Disease". In: *Journal of Neurology and Stroke* 1 (Sept. 2014), p. 00028. DOI: `10.15406/jnsk.2014.01.00028`.

[4] Anne Cataldo et al. "Abnormalities in Mitochondrial Structure in Cells from Patients with Bipolar Disorder". In: *The American journal of pathology* 177 (Aug. 2010), pp. 575–85. DOI: `10.2353/ajpath.2010.081068`.

[5] *Cell*. `https://www.genome.gov/genetics-glossary/Cell`. last visited on September 2021.

[6] Nancy A. Chinchor. "MUC-4 evaluation metrics". In: *MUC*. 1992.

[7] Laurent D. Cohen. "On active contour models and balloons". In: *CVGIP: Image Understanding* 53.2 (1991), pp. 211–218. ISSN: 1049-9660. DOI: `https://doi.org/10.1016/1049-9660(91)90028-N`. URL: `https://www.sciencedirect.com/science/article/pii/104996609190028N`.

[8] Julia Dietlmeier et al. "Few-shot hypercolumn-based mitochondria segmentation in cardiac and outer hair cells in focused ion beam-scanning electron microscopy (FIB-SEM) data". In: *Pattern Recognition Letters* 128 (2019), pp. 521–528. ISSN: 0167-8655. DOI: `https://doi.org/10.1016/j.patrec.2019.10.031`. URL: `https://www.sciencedirect.com/science/article/pii/S0167865519303095`.

[9] Ray F. Egerton. *Physical Principles of Electron Microscopy*. Springer US, 2005. DOI: `10.1007/b136495`. URL: `https://doi.org/10.1007%5C%2Fb136495`.

[10] Martin Ester et al. "A Density-Based Algorithm for Discovering Clusters in Large Spatial Databases with Noise". In: *Proc. of 2nd International Conference on Knowledge Discovery and*. 1996, pp. 226–231.

[11] Lucille A. Giannuzzi. "Scanning Electron Microscopy and X-Ray Microanalysis 4th Edition, Joseph I. Goldstein, Dale E. Newbury, Joseph R. Michael, Nicholas W.M. Ritchie, John Henry J. Scott, David C. Joy, Springer, 2018, 550 pp. ISBN:978-1-4939-6674-5." In: *Microscopy and Microanalysis* 24.6 (2018), pp. 768–768. DOI: `10.1017/S1431927618015271`.

[12] R. Giuly, M. Martone, and M. Ellisman. "Method: automatic segmentation of mitochondria utilizing patch classification, contour pair classification, and automatically seeded level sets". In: *BMC Bioinformatics* 13 (2011), pp. 29–29.

[13] Tomohiro Haruta. "Comparison of 3D Imaging Methods in Electron Microscopy for Biomaterials". In: *Analytics* 8 (Jan. 2018), pp. 536–543. DOI: `10.22184/2227-572X.2018.08.6.536.543`.

[14] Q. He et al. "Biological serial block face scanning electron microscopy at improved z-resolution based on Monte Carlo model". In: *Scientific Reports* 8.1 (Aug. 2018). DOI: `10.1038/s41598-018-31231-w`.

[15] Qianping He et al. "Sub-Surface Serial Block Face Scanning Electron Microscopy". In: *Biophysical Journal* 108 (Jan. 2015), 619a–620a. DOI: `10.1016/j.bpj.2014.11.3371`.

[16] Jon Holy and Ed Perkins. "Structure and Function of the Nucleus and Cell Organelles". In: Jan. 2009, pp. 3–31. ISBN: 978-1-934115-02-2. DOI: `10.1007/978-1-59745-440-7_1`.

[17] Sabzali Javadov, Andrey Kozlov, and Amadou Camara. "Mitochondria in Health and Diseases". In: *Cells* 9 (May 2020), p. 1177. DOI: `10.3390/cells9051177`.

[18] M. Kannan. "Scanning Electron Microscopy: Principle, Components and Applications". In: Mar. 2018, pp. 81–92. ISBN: isbn 978-93-5124-932-0 (PB).

[19] MERİH ALPHAN KARADENİZ. "AUTOMATIC SEGMENTATION OF CRISTAE MEMBRANES IN 3D ELECTRON MICROSCOPY TOMOGRAPHY IMAGES USING ARTIFICIAL NEURAL NETWORKS". MA thesis. MIDDLE EAST TECHNICAL UNIVERSITY, Sept. 2016.

[20] David Kelley et al. "Dysfunction of Mitochondria in Human Skeletal Muscle in Type 2 Diabetes". In: *Diabetes* 51 (Nov. 2002), pp. 2944–50. DOI: `10.2337/diabetes.51.10.2944`.

[21] Yoshiyuki Kubota, Jaerin Sohn, and Yasuo Kawaguchi. "Large Volume Electron Microscopy and Neural Microcircuit Analysis". In: *Frontiers in Neural Circuits* 12 (2018), p. 98. ISSN: 1662-5110. DOI: `10.3389/fncir.2018.00098`. URL: `https://www.frontiersin.org/article/10.3389/fncir.2018.00098`.

[22] David Leadley. *Transmission Electron Microscopy(TEM)*. `https://warwick.ac.uk/fac/sci/physics/current/postgraduate/regs/mpagswarwick/ex5/techniques/structural/tem/`. last visited on September 2021. Jan. 2010.

[23] Weifu Li et al. "An Automated Pipeline for Mitochondrial Segmentation on ATUM-SEM Stacks". In: *Journal of Bioinformatics and Computational Biology* 15 (May 2017). DOI: `10.1142/S0219720017500159`.

[24] *Library digital collections: UC San DIEGO LIBRARY*. `https://library.ucsd.edu/dc/`. last visited on September 2021.

[25] Jing Liu et al. "Automatic Detection and Segmentation of Mitochondria from SEM Images using Deep Neural Network". In: *2018 40th Annual International Conference of the IEEE Engineering in Medicine and Biology Society (EMBC)*. 2018, pp. 628–631. DOI: 10.1109/EMBC.2018.8512393.

[26] Aurélien Lucchi et al. "Supervoxel-Based Segmentation of Mitochondria in EM Image Stacks With Learned Shape Features". In: *IEEE Transactions on Medical Imaging* 31 (2012), pp. 474–486.

[27] Baptiste Magnier, Philippe Montesinos, and Daniel Diep. "Ridges and Valleys Detection in Images Using Difference of Rotating Half Smoothing Filters". In: *Advanced Concepts for Intelligent Vision Systems*. Ed. by Jacques Blanc-Talon et al. Berlin, Heidelberg: Springer Berlin Heidelberg, 2011, pp. 261–272. ISBN: 978-3-642-23687-7.

[28] Antonio Martinez-Sanchez et al. "Robust membrane detection based on tensor voting for electron tomography". In: *Journal of Structural Biology* 186.1 (2014), pp. 49–61. ISSN: 1047-8477. DOI: https://doi.org/10.1016/j.jsb.2014.02.015. URL: https://www.sciencedirect.com/science/article/pii/S1047847714000495.

[29] Harrie Massey and D. H. Davis. "Eric Henry Stoneley Burhop. 31 January 1911-22 January 1980". In: *Biographical Memoirs of Fellows of the Royal Society* 27 (1981), pp. 131–152. ISSN: 00804606. URL: http://www.jstor.org/stable/769868.

[30] E.U. MUMCUOGLU et al. "Computerized detection and segmentation of mitochondria on electron microscope images". In: *Journal of Microscopy* 246.3 (2012), pp. 248–265. DOI: https://doi.org/10.1111/j.1365-2818.2012.03614.x. eprint: https://onlinelibrary.wiley.com/doi/pdf/10.1111/j.1365-2818.2012.03614.x. URL: https://onlinelibrary.wiley.com/doi/abs/10.1111/j.1365-2818.2012.03614.x.

[31] R. Narasimha et al. "Automatic joint classification and segmentation of whole cell 3D images". In: *Pattern Recognit.* 42 (2009), pp. 1067–1079.

[32] Nhan Nguyen-Thanh, Tuan Pham, and Kazuhisa Ichikawa. "Automated Detection and Segmentation of Mitochondrial Images based on Gradient Enhancement and Adaptive Gabor Filter". working paper or preprint. Sept. 2019. URL: https://hal.archives-ouvertes.fr/hal-02284786.

[33] Jodi Nunnari and Anu Suomalainen. "Mitochondria: In sickness and in health". English (US). In: *Cell* 148.6 (Mar. 2012), pp. 1145–1159. ISSN: 0092-8674. DOI: 10.1016/j.cell.2012.02.035.

[34] Christopher J. Peddie and Lucy M. Collinson. "Exploring the third dimension: Volume electron microscopy comes of age". In: *Micron* 61 (2014), pp. 9–19. ISSN: 0968-4328. DOI: https://doi.org/10.1016/j.micron.2014.01.009. URL: https://www.sciencedirect.com/science/article/pii/S0968432814000250.

[35] Serdar F. Tasel et al. "A validated active contour method driven by parabolic arc model for detection and segmentation of mitochondria". In: *Journal of Structural Biology* 194.3 (2016), pp. 253–271. ISSN: 1047-8477. DOI: https://doi.org/10.1016/j.jsb.2016.03.002. URL: https://www.sciencedirect.com/science/article/pii/S1047847716300387.

[36] *The Imod Home Page*. https://bio3d.colorado.edu/imod/. last visited on September 2021.

[37] C. Tomasi and R. Manduchi. "Bilateral filtering for gray and color images". In: *Sixth International Conference on Computer Vision (IEEE Cat. No.98CH36271)*. 1998, pp. 839–846. DOI: 10.1109/ICCV.1998.710815.

[38] *Transmission Electron Microscopy vs Scanning Electron Microscopy*. https://www.thermofisher.com/tr/en/home/materials-science/learning-center/applications/sem-tem-difference.html?gclid=EAIaIQobChMI6IGcsdSG8wIVh6SyCh1M_QQSEAAYASAAEgK-jPD_BwE. last visited on September 2021.

[39] Ivá Valdés, Yoshihiko Nomura, and Yasunaga Mitsuya. "Equidistant Snakes: Accurate Irregular Shaped Contour Detection". In: *Proceedings of IAPR Workshop on Machine Vision Applications, MVA 1996, November 12-14, 1996, Tokyo, Japan*. 1996, pp. 285–288. URL: http://b2.cvl.iis.u-tokyo.ac.jp/mva/proceedings/CommemorativeDVD/1996/papers/1996285.pdf.

[40] Willy W. Wong. *About The Cell*. http://www.cellimagelibrary.org/pages/about. last visited on September 2021.

[41] Chi Xiao et al. "Automatic Mitochondria Segmentation for EM Data Using a 3D Supervised Convolutional Network". In: *Frontiers in Neuroanatomy* 12 (2018), p. 92. ISSN: 1662-5129. DOI: 10.3389/fnana.2018.00092. URL: https://www.frontiersin.org/article/10.3389/fnana.2018.00092.